Study on Crystal Design and Growth of Metal-organic Frameworks toward Gas Separation and Membrane Fabrication

WANG Xiaoguang

Study on Crystal Design and Growth of Metal-organic Frameworks toward Gas Separation and Membrane Fabrication

ガス分離と膜作製に向けた金属有機構造体の結晶設計と成長に関する研究

July 2022

Nagoya University
Graduate School of Engineering
Department of Materials Chemistry

WANG Xiaoguang

Reviewers of This Thesis

Prof. Dr. Ryotaro Matsuda (Thesis supervisor)
Nagoya University

Prof. Dr. Kazuki Nakanishi
Nagoya University

Prof. Dr. Yoshiaki Kawajiri
Nagoya University

Prof. Dr. Ayae Sugawara-Narutaki
Nagoya University

Preface

Gas is used extensively as an energy source in industry and our daily lives. The combustion of fossil fuels and industrial production release massive gas mixture and the separation of gas is not only occupying a very important position in industrial production but also has a significant impact on the ecological environment. For example, the capture of carbon dioxide (CO_2) in flue gases can contribute to achieving carbon neutrality, the removal of traces of acetylene in ethylene to purify ethylene, and the separation of atmospheric air into its primary components, typically nitrogen and oxygen. Microporous and mesoporous materials are widely used in gas adsorption separation and membrane separations due to their large internal space, uniform pore channels, and permanent porosity, such as activated carbons, zeolites, mesoporous silicas, and so on. In the past few years, Metal-organic frameworks (MOFs), a class of newly developed crystalline hybrid porous materials, have been a very rapid development not only in the synthesis of novel structures but also potential applications in a variety of fields. There are two main approaches to the application of MOFs for gas separation. One approach is to introduce functionalized reactive groups and active metal sites to improve the selectivity of gas adsorptive separation. Besides, the sieving of molecules through the channels of MOF membranes is another effective separation method. However, so far the design of MOFs for gas selective adsorption main focus on inserting open metal site to improve the bonding between frameworks and molecules, while the way of introducing functionalized ligands is more diverse. Thus, the design of MOFs with porous structures and functional groups which can coordinate with gas molecules in the pore channels of MOFs to achieve separation is worth exploring. What's more, the researches on MOFs membranes for gas separation are still limited compared to the number of reported MOFs. Crystal growth rate control, pore size adjustment, crystal growth into dense membranes, and structure orientation control are still not well clarified. Therefore, it needs further research on the

fabrication of MOF membranes for gas separation and the synthesis of MOFs for selective adsorption.

In this thesis, the structural diversity of MOFs and MOFs containing functional groups for gas selective adsorption are summarized. Methods for the preparation of MOF membranes on porous substrates for gas separation and orientation control of MOF membranes are described. This thesis also has focused on the construction of SIFSIX (SIFSIX, hexafluorosilicate (SiF_6^{2-}) pillared MOFs containing reactive functional groups for trapping O_2 from the air and interaction sites for C_2H_2/C_2H_4 separation. Through the rational design of metal ions and organic ligands, as well as adjustment of solvent and post-treatment method, the stable three-dimensional (3D) porous MOF crystals with internal nanospace to accommodate the guest molecules were obtained. This thesis also studies the fabrication of MOF membranes for H_2 purification, CO_2/CH_4, and CO_2/N_2 separation. The method for preparing dense membranes was developed through chemical modifications for porous substrates. What's more, a new concept of preparing bilayer membranes by adjusting the pore size and growth rate of the crystals to separate CO_2 was also established. This thesis will contribute to a deeper understanding of the design of the crystal structure of MOFs for selective adsorption and the growth of MOFs crystals into membranes on substrates for gas separation. This thesis is composed of six chapters as follows.

Chapter 1 describes the background, significance, and purpose of this thesis. Firstly, the structure, development, and applications of MOFs are overviewed. Next, the secondary building units (SBUs) of MOFs, the influence of the conditions of synthesis on the structure, and the effects of post-treatment on the structure toward gases capture and separation are introduced. MOF crystals growth to form membrane and crystal orientation control are also described for the gas separations.

Chapter 2 describes that a series of MOFs based on 9,10-Di(4-pyridyl)anthracene (dpa) and two MOFs based on 9,10-epidioxidoanthracene (epo) were synthesized by self-assembly with metallic hexafluorosilicate. Interestingly, Co^{2+}, Ni^{2+}, Cd^{2+} or Zn^{2+} with

9,10-Di(4-pyridyl)anthracene show different 1D, 2D and 3D topologies using same solvent. Compounds [$Zn(dpa)_2(SiF_6)$] is a 3D structure that can maintain stability after removal of the solvent, it exhibits the property of trapping oxygen under photoirradiation and releasing oxygen after heating. We also directly synthesized compounds [$Zn(epo)_2(SiF_6)$] to determine the structure of [$Zn(dpa)_2(SiF_6)$] after photoirradiation. Our works indicate that [$Zn(dpa)_2(SiF_6)$] can selectively capture oxygen from the air and can release O_2 through the reverse reaction upon application of heat. It has the potential application for the separation of oxygen in air.

Chapter 3 describes the synthesis of a series of 3D SIFSIX pillared MOFs using different metals and 4,4′-bipyridine or 1,2-bis(4-pyridyl)ethane. Due to the tendency of crystallization of SIFSIX pillared MOFs into 2D non-porous structures in an aqueous environment, it has been a challenge to synthesize those MOFs with 3D coordination networks. Based on the study of Chapter 2, the same method is applied to the synthesis of SIFSIX-1-M (Ni, Co, Cd) and SIFSIX-7-M (Ni, Co, Cd) using the organic linkers 4,4′-bipyridine and 1,2-bis(4-pyridyl)ethane, respectively. Among them, SIFSIX-1-Ni, SIFISX-1-Co, and SIFSIX-7-Ni show excellent adsorption selectivities for CO_2 from a CO_2/N_2 gas mixture and C_2H_2 from a C_2H_2/C_2H_4 gas mixture respectively.

Chapter 4 describes the efficient fabrication method for the membrane of a metal-organic framework (MOF) (Kgm-OEt) which is one kind of kagomé-type MOF with a two-dimensional (2D) sheet structure having one-dimensional (1D) channels suitable for separation of H_2 from other larger gases. Kgm-OEt seed layer was created on an Al_2O_3 substrate using layer-by-layer (LBL) growth, then a membrane was fabricated by the secondary growth. The membrane on a 3-aminopropyltriethoxysilane (APTEs)-treated substrate obtained in this method was continuous and defect-free with the crystal orientation suitable for gas transportation, while the membrane grown on a bare substrate was loosely packed with the unfavorable crystal orientation. Kgm-OEt membrane also shows better H_2/CO_2 separation performance than polymer membranes.

Chapter 5 describes the fabrication of the heterobilayer membrane strategy using

two isostructural MOFs. First, a MOF Kgm-OPr with fast nucleation rate was fabricated as a seed layer on an Al_2O_3 substrate, then the layer of Kgm-OMe or Kgm-H, which is isostructural to Kgm-OPr, was prepared on the Kgm-OPr seed layer through secondary growth. In this way, the high-quality membranes which selectively permeate CO_2 over N_2, CH_4, and C_2H_4 were obtained, although all three MOFs did not form dense membranes when they were used alone. Our result would contribute to the expansion of the family of MOFs applicable to membranes for molecular separation.

Chapter 6 describes the conclusions of this thesis, including the synthesis of MOF crystals for the selective adsorption for gas and the fabrication of MOF membranes for gas separation.

Contents

Chapter 1

General Introduction

1-1. Introduction

In 1706, scientists discovered the first compound with a three-dimensional net structure, Prussian blue, whose structure was determined by Lude et al. [1] in 1972, but did not attract much attention at that time. Wells et al. [2] laid the foundation of topological theory for the net structure of inorganic compounds by reducing the crystal structure to a series of nodes with geometric configurations (planar triangles, tetrahedra, etc.). In 1989, Robson et al. [3,4] extended topology theory further to the coordination polymers and firstly proposed the following opinion: using the structure of some simple minerals as the network prototype, replace the nodes in the network structure with geometrically matched molecular modules, and replace the single chemical bonds in the prototype network with organic linkers to construct coordination polymers with mineral topological structures. Robson's vision and pioneering work pointed the way for the development of coordination polymers research. Subsequently, Yaghi's group in The United States and Kitagawa's group in Japan have developed those metal-organic skeletal structure materials and named them metal-organic frameworks (MOFs) or porous coordination polymers (PCPs).

Chapter 1 describes the structure, development of MOFs and their applications in gas separation. A background of MOFs is described in Section 1-2. In Section 1-3, the influence of structural phase control of crystals as well as the effect of surface functional groups of MOF crystals on the adsorption and separation of gases are summarized. In Section 1-4, the crystallization of MOFs into a dense membrane and the control of structural orientation toward gas separation are generalized. The significance and purpose of this study are presented in Section 1-5.

1-2. Background of metal-organic frameworks

Recently, MOFs have emerged as an indispensable part of the field of porous materials. They are widely used in gas adsorption [5], separation [6], fluorescence [7],

magnetism [8], catalysis [9], and molecular recognition [10]. As shown in the **Figure 1-1**, MOFs materials are infinitely extending coordination polymers formed by the bridging of a single metal ion (or metal ion cluster) and organic ligands [11-13]. MOFs can achieve the desired target products through reasonable optimization, ligand control, and specific synthesis conditions. This is the essence of MOFs compared to other porous materials (such as activated carbon and zeolite). The structure of MOFs can be determined by X-ray diffraction, thereby promoting their rational design and functional modification. As a class of inorganic-organic hybrid materials, MOF compounds are functional materials with the characteristics of both inorganic compounds and organic compounds. In recent years, they have attracted the attention of countless scientific researchers.

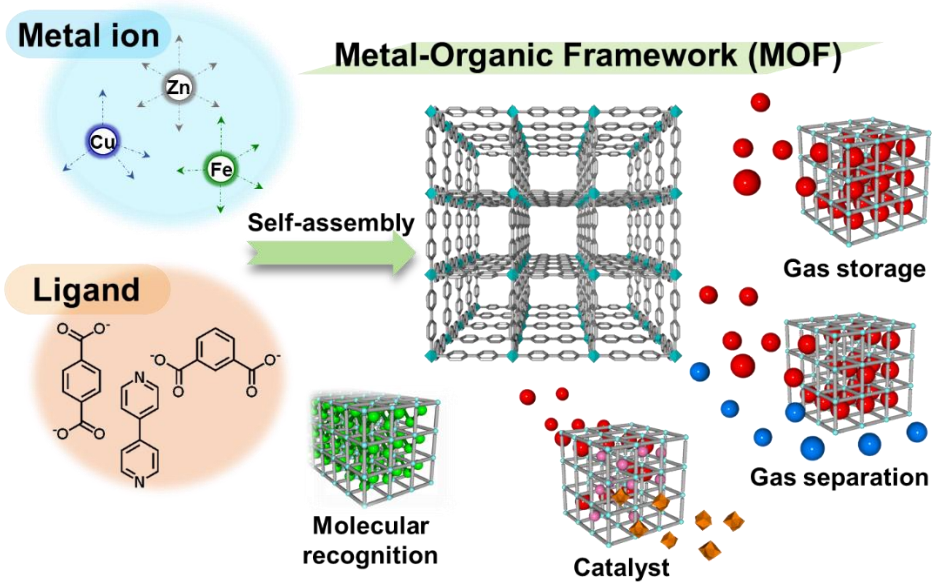

Figure 1-1. Metal-organic frameworks and their applications.

Over the past two decades, MOFs have shown rapid growth in terms of preparation, characterization, and evaluation. Flexible self-assembly through metal ion clusters as secondary building units (SBUs) with organic ligands, thousands of new MOFs materials are prepared every year. [14] MOFs are particularly suitable for gases and liquids adsorption because of they possess large specific surface area and high porosity [15,16], especially the adsorption of gas molecules has become a hot research topic. The adsorption of gas mainly relies on the interaction between gas molecules and framework (Hydrogen

bonding, electrostatic interaction, etc.). [17,18] MOFs have structural diversity and variability of surface properties, which make them have great potential applications in gas selective adsorption and membrane separation.

1-3. Design of MOFs for gas adsorption and separation

For single-component gas molecules, MOFs are mainly focused on large-capacity gas storage. MOFs with high adsorption amounts have significant prospective applications for gas storage. In contrast, for multi-components, MOFs can be used as effective separating porous materials. Separation processes have important applications in industry. However, the commonly used separation processes such as distillation, crystallization, and extraction are suffering from high energy consumption and complex separation processes. [19, 20] Compared with distillation separation, adsorption separation and membrane separation based porous materials in the separation process have a lower energy consumption benefited by their low energy consumption and easy operation. [21, 22] MOFs as a new type of porous material also have important applications in the separation field.

1-3-1. Crystal phase control in MOFs for gas adsorption and separation

MOFs can be divided into zero-dimensional (0D), one-dimensional (1D), two-dimensional (2D), and three-dimensional (3D) structures according to their skeletal structure (**Figure 1-2**). Zero-dimensional are mainly polygonal or polyhedral MOFs, which are usually very rich in hydrogen bonds. One-dimensional are mainly linear chains, trapezoidal chains, or z-shaped chains of various shapes, with chains usually connected by hydrogen bonds or π-π interactions. Two-dimensional are mainly some square or rectangular, bilayer or honeycomb type structures. Three-dimensional MOFs have complex structures with infinite skeletons extending in three directions, which have higher stability and broader application prospects.

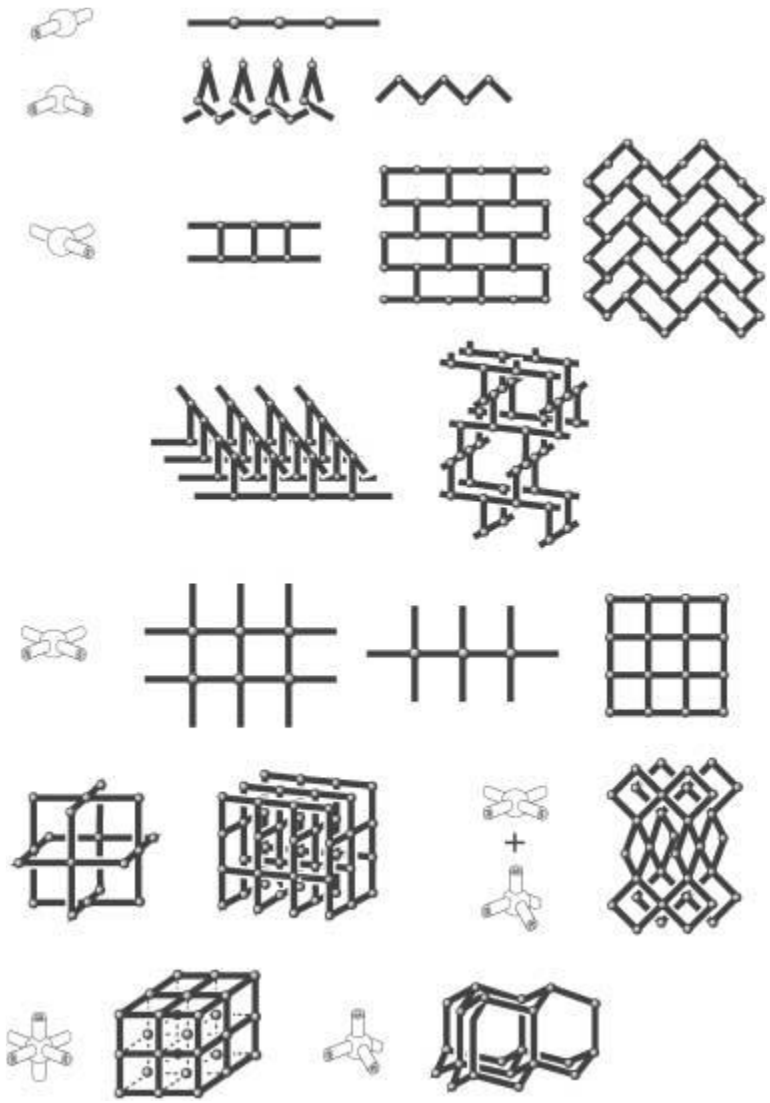

Figure 1-2. The structural frameworks that can be constructed by using different connectors and linear linkers. [23] Copyright (2004) Wiley Online Library.

The process of adsorption and separation is also a thermodynamic equilibrium of the adsorbed gas mixture in the porous material. There is a competition for adsorption in the pores, the molecules that interact strongly with the framework preferably get adsorbed in large amounts compared to the molecules that interact weakly with the framework and lead to their separation based on adsorption. [24] Therefore, the most essential factor for the application of MOFs in the adsorption and separation of gases is porosity and stability. Although thousands of MOFs have been reported so far, a significant proportion of the

crystal structures are either unstable or non-porous.

About the synthesis of MOFs, different synthesis methods often obtain different structures when using the same starting materials. In order to obtain the target structure of MOFs, it is important to choose a suitable synthesis method. Many factors are affecting the synthesis process of MOFs. Firstly, the basic network structure depends on the coordination environment of metal clusters and organic linkers. Secondly, the anti-balance anion of metal ions, template molecules, solvents, reactant ligands, and pH values all have effects during the nucleation of MOFs crystals. Finally, the post-synthesis treatment is also crucial. The exchange of solvents during the solvent exchange process can also have an impact on the structure of MOFs, especially for MOFs with larger specific surface areas, which require mild conditions to maintain the stability when removing the solvent molecules.

Öhrström et al. [25] reported three types of MOFs which are composed of Y^{3+}, Ce^{3+}, or Gd^{3+} coordinated by benzene-1,2,4,5-tetracarboxylate to form crystal structure of a dot-MOF (CTH-14), a sheet-MOF (CTH-15), and a rod-MOF (CTH-16) (**Figure 1-3**). In addition, only CTH-15 Ce(IV) is stable, suggesting that the sheet-MOFs can represent an intellectual advance in the development of MOFs. The order of stability of these three MOFs (dot-, rod- and sheet- MOFs) is as follows dot-MOFs < rod-MOFs < sheet-MOFs. Different metals and the same ligand form different topological structures and the stability of the different structures varies with the overall stability of the structures following the stability order as 2D > 1D > 0D.

Bloch et al. [26] synthesized a series MOFs with different structures using the same metals and ligands through precisely tuning the synthesis conditions such as solvents and temperature. The reaction of copper salts with isophthalic acid affords tetragonal sheet, hexagonal sheet, and porous cage (**Figure 1-4**). The discrete porous cages display a higher surface area than the 2D sheet and show good ethane and ethylene adsorption properties.

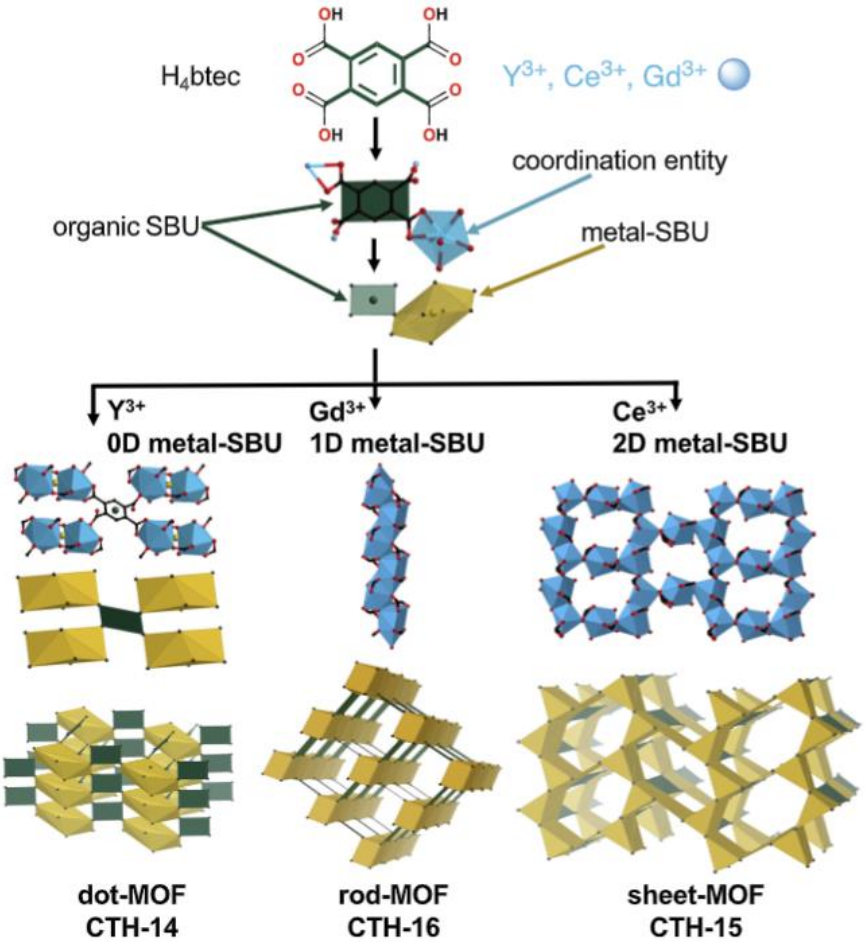

Figure 1-3. Overview of the three different MOFs, CTH-14, CTH-15, and CTH-16 [25]. Copyright (2021) Cell Press.

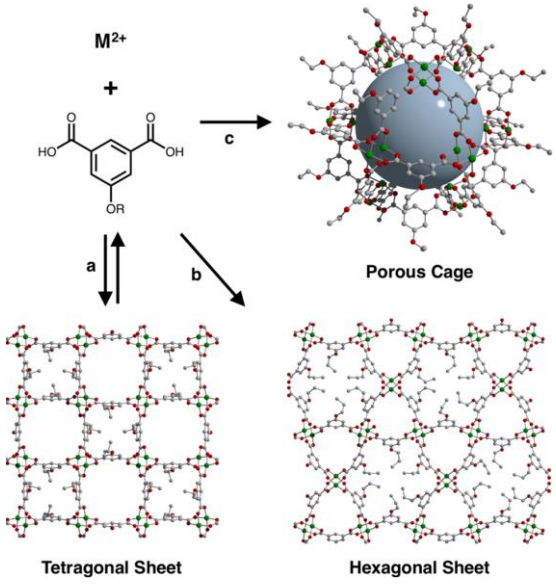

Figure 1-4. Reaction scheme illustrating the synthesis of two dimensional layered materials and discrete, intrinsically porous molecular assemblies. Copyright (2018) American Chemical Society.

In addition, Zaworotko et al. [27] reported a SIFSIX pillared MOFs called SIFSIX-14-Cu-i which is composed of Cu (II) cations and 1,2-bis(4-pyridy)diazene to form a square grid structure with sql network. These networks are pillared by SiF_6^{2-} anions to construct a 3D framework. However, SIFSIX-14-Cu-i can transform to nonporous interpenetrated square grid topology networks from porous pcu topology networks by crystalline-to-crystalline phase transitions (**Figure 1-5**) in the humid environment. They also found that 3D structures could be obtained when the synthesized solvents did not contain water, instead, a mixture of the 3D phase and 2D phase was obtained in aqueous solvents. The porous phase SIFSIX-14-Cu-i also exhibits high CO_2 uptake capacity and CO_2/N_2 selectivity. Eddaoudi et al. [28] also found the structural phase transformation of the 2D structure of the SIFSIX-3-Ni analogue and 3D SIFSIX-3-Ni can occur after using the wetting and heating process.

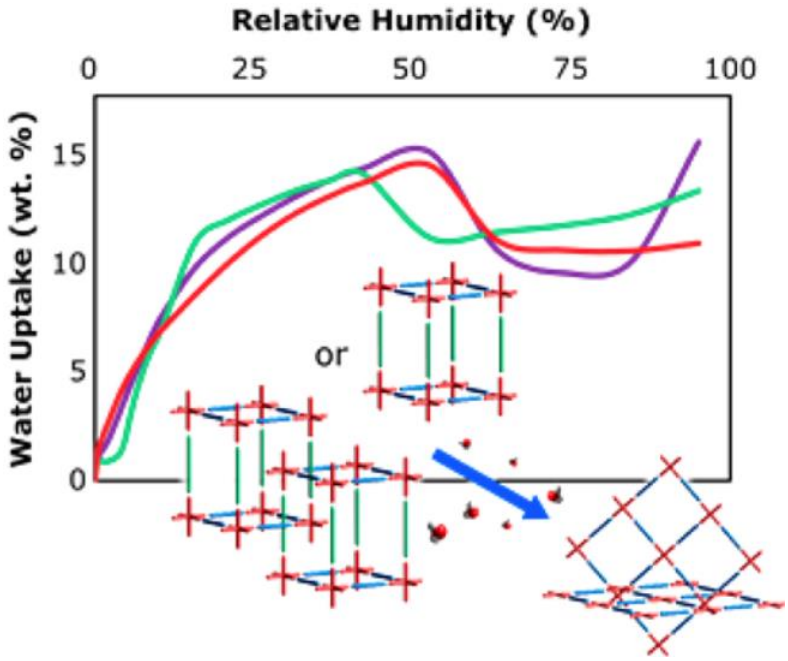

Figure 1-5. Transformations of SIFSIX-14-Cu-i from 3D porous structure to nonporous interpenetrated structure. Copyright (2017) American Chemical Society.

The design of porous and stable MOFs with large adsorption capacity and selectivity for gases is worthy to explore in the future. Porous MOFs not only can be applied for molecular storage and separation but also catalysis, molecular recognition, drug delivery, etc.

1-3-2. Surface functionalization of MOFs for gas adsorption and separation

Although there have been many reports on the MOFs that can adsorb a large capacity of gases molecules based on physical adsorption. To improve the gas adsorption selectivity, for example, the incorporation of organic linkers containing functional groups into MOFs has been shown to greatly enhance the binding affinity for gases. Although open metal sites(OMS) also provide binding sites for gas, the ligands containing coordinative sites are more variable. These functional groups include $–NH_2$, $–NO_2$, –CN, –SH, etc. For example, acid-base type interactions between the lone-pair of $–NH_2$ and CO_2 can greatly improve the separation performance of CO_2/N_2 when using MOFs containing $–NH_2$ groups. Caro's group [29] made a comparison of the difference of CO_2 adsorption capacity by UIO-66 and UIO-66-NH_2, the ligand of UIO-66-NH_2 contain -NH_2 groups compared with UIO-66, but the CO_2 adsorption capacity of the UIO-66-NH_2 is nearly 2 times higher than that of UIO-66 due to the Lewis basic amines have a stronger affinity to CO_2. The SIFSIX series including $SiF_6^{2–}$ has strong C–H···F hydrogen (H) bonding with acetylene, which exhibit excellent C_2H_2 storage performance. [30, 31] In particular, SIFSIX-1-Cu [32] shows a high separation efficiency for C_2H_2/C_2H_4 mixtures which is demonstrated by experimental breakthrough curves (0.73 millimoles per gram from a 1/99 mixture). In addition, Matsuda et al. [33] reported a flexible structure (CPL-1: $Cu_2(pzdc)_2(pyz)$) with hydrogen bonding between non-coordinated oxygen atoms and acidic hydrogens of the acetylene molecule (**Figure 1-6)**. Later, Li's group [34] also found that the flexible CPL-1 can achieve adsorptive separation of C_3H_6 over C_3H_8 via the gate

opening adsorption for C_3H_6 but not for C_3H_8 at 273 K. This is a result of the slight rotation of the pyrazine ligand, where the C_3H_6 molecule can be more preferentially adsorbed by forming hydrogen bonds with the pyrazine, and then the transformation of its structure triggers the opening of the pores.

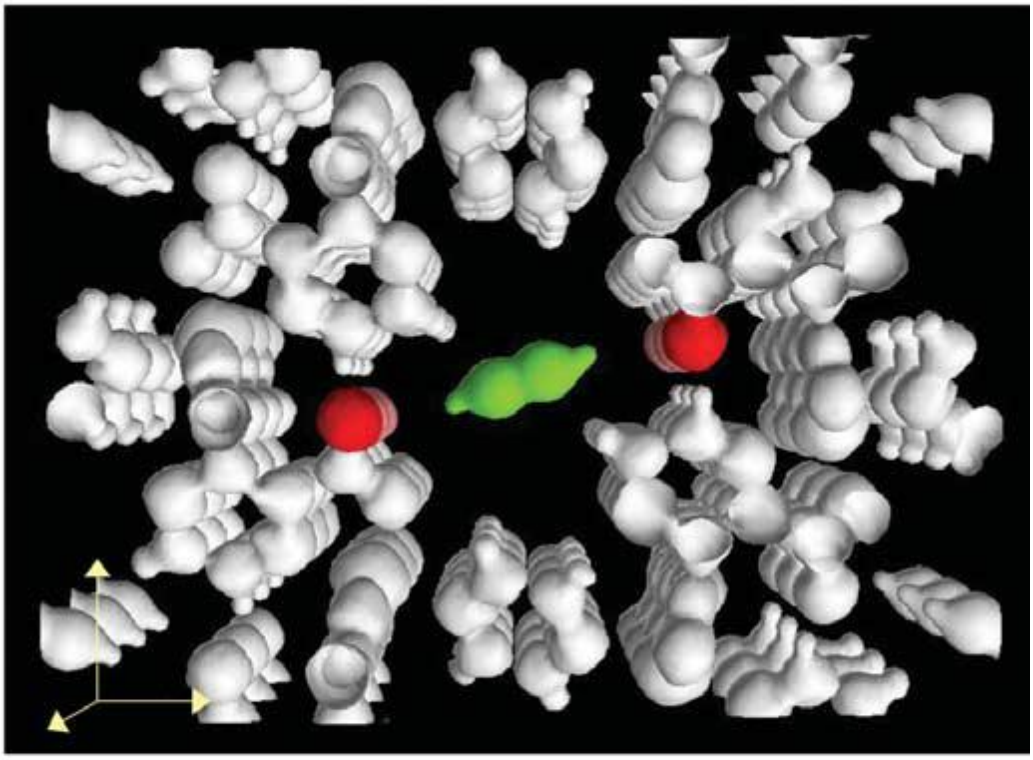

Figure 1-6. MEM electron densities of C_2H_2 adsorbed 1 at 170K as an equal-density contour surface along the a-axis. Copyright (2005) Nature.

MOFs based on reversible chemical reactions with gas molecules are also very worthy to investigate, since capturing the gas molecules through chemical reactions is stronger than physical adsorption. Yaghi et al. [35] reported functionalized IRMOF-74-III-CH_2NH_2 compounds which can capture CO_2 in the presence of water (**Figure 1-7**). The alkylamines in IRMOF-74-III-CH_2NH_2 chemically bind CO_2, leading to a high CO_2 uptake capacity (3.2 mmol g^{-1} at 800 Torr). Matsuda's group [36] synthesized a MOMF-1 ($[Zn_2(dpa)(2,6\text{-}NDC)_2]\cdot(DMF)_2$) with the ability to trap and release oxygen molecules dissolved in various liquid solvents. MOMF-1 can selectively trap oxygen in the solvent without reacting with other gas molecules (**Figure 1-8**). In this case, adsorption and

release through a reversible chemical reaction have become an efficient separation method.

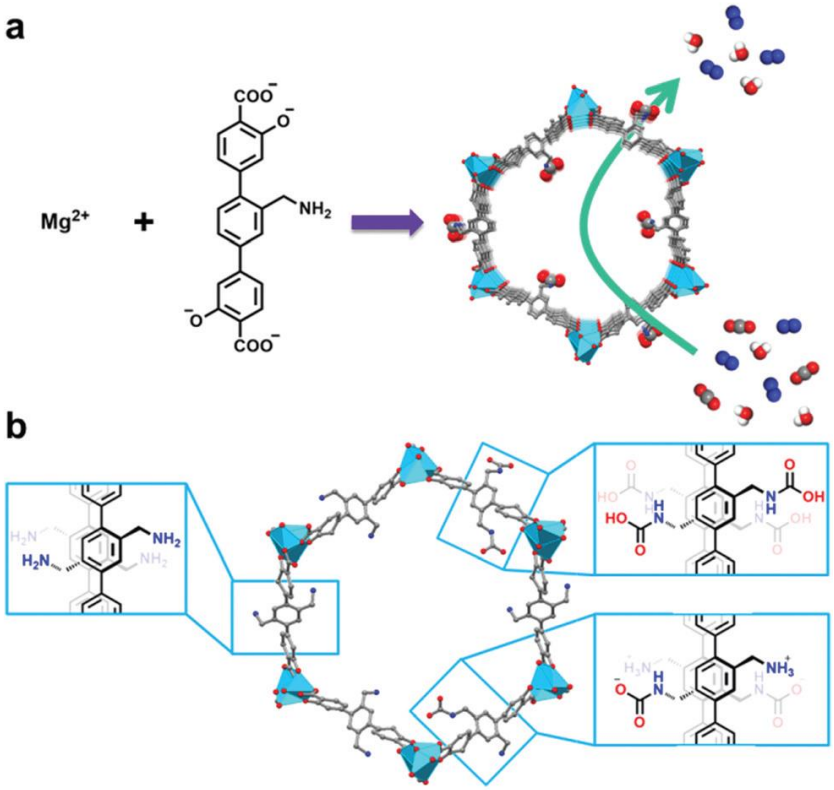

Figure 1-7. (a) Synthesis of IRMOF-74-III-CH_2NH_2 from Mg^{2+} and the amine functionalized linker (20-(aminomethyl)-3,300-dioxido-[1,10:40,100-terphenyl]-4,400-dicarboxylate) for selective, chemisorptive CO_2 capture from a $CO_2/N_2/H_2O$ gas mixture. (b) View of modeled IRMOF-74-III-$(CH_2NH_2)_2$ structure down the crystallographic c-axis, depicting the three pore environments before (left pore wall) and after exposure to CO_2 under dry conditions toproduce carbamic acids (upper right pore wall) and 95% relative humidity(RH) to give ammonium carbamates (bottom right pore wall). Color code:C, gray; O, red; N, blue; H, white; and Mg, cyan. Copyright (2017) American Chemical Society.

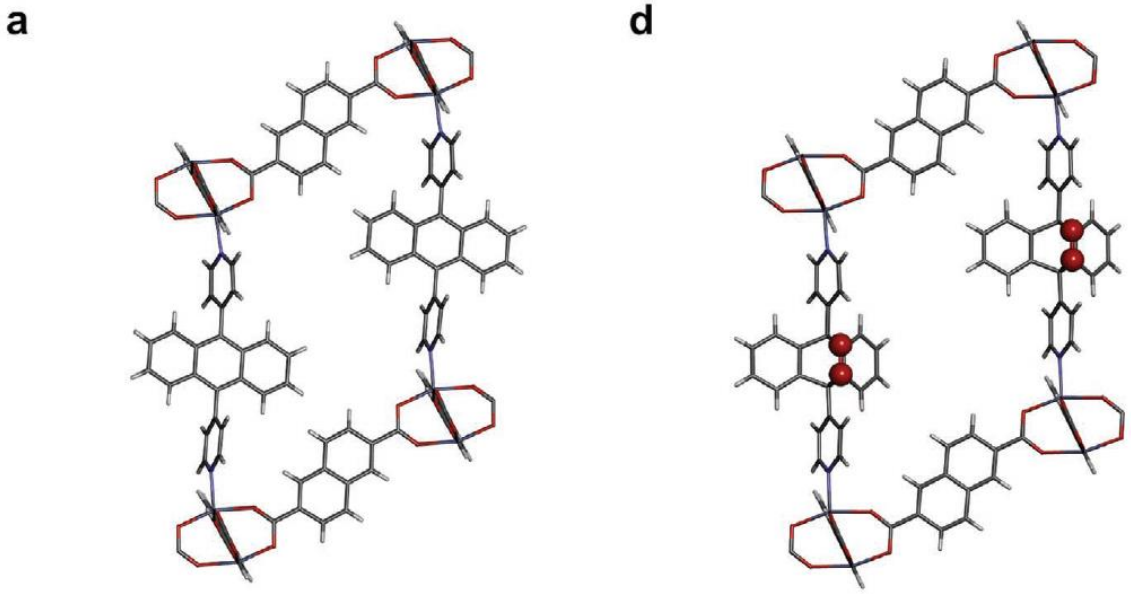

Figure 1-8. Crystal structures of MOMF-1 and MOMF-2. DMF molecules are omitted from all of the structures for the clarity. Oxygen atoms on endoperoxides are highlighted to the ball model. a,d) Unit structures of MOMF-1 and MOMF-2. Copyright (2020) Wiley Online Library.

In summary, the benefit of their extraordinary specific surface areas, finely tunable pore surface properties, and structural flexibility have made MOFs become the most promising porous materials for many applications such as gas storage, selective adsorption, and separation.

1-4. Fabrication of MOF membranes for gas separations

With the increase in energy consumption, membrane separation technology is gaining attention due to its environmental friendliness and low operating costs. [37, 38] In engineering operations, the space occupation of gas membrane separation units is smaller than other operating units, such as gas adsorption separation units. [39] Traditional separation units such as distillation and absorption in the separation process usually require phase transition and high energy consumption, whereas membrane separation units do not require a phase transition. [40] Combining the superiority of smaller space

occupation and low energy consumption, membrane separation has a better application prospect than other traditional separation methods. The membrane separation process is schematically presented in the **Figure 1-19**. The indicators for evaluating the membrane separation performance are mainly the separation selectivity and permeability of the membrane. Polymer membranes are widely used on a large scale in practical industrial membrane separation processes because they are easy to produce and have good mechanical properties. [41,42] However, some inherent limitations, such as the permeability/selectivity trade-off have been exist in polymeric membranes. Polymer membrane is difficult to achieve high selectivity and permeability simultaneously, and there is a constrained relationship between selectivity and permeability [43-45]. In many cases, polymer membranes need to increase permeability by reducing selectivity or increase selectivity by decreasing permeability, so they are difficult to achieve trade-off. Besides, plasticization and susceptibility to harsh operating conditions are also serious impediments to its wide range of application in the industry of polymer membranes. [46] Inorganic membranes based on porous materials may offer an alternative solution to the above problems as they exhibit, permanent porosity, framework robustness, and the ability to separate molecules based on their shape, size, and affinity to the framework. So far, Zeolite membranes have been applied in industrial separation because they have homogeneous, molecular-size pores (typically 0.3-1.3 nm) and excellent thermal, mechanical, and chemical stability. [47-49] Compared to zeolite materials, MOFs are highly attractive for assembly into MOF membranes for gas and liquid separations because their pores can be reasonably controlled by the interaction of metal ions and organic linkers, and their pore surfaces can be rationally modified via a variety of approaches.

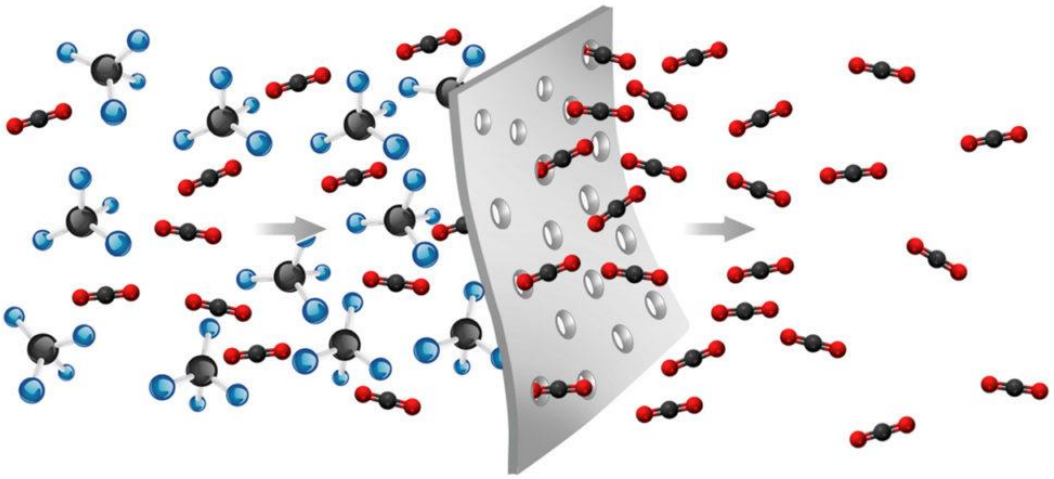

Figure 1-9 . Scheme of membrane separation. Copyright: (2012-2019) Nordic membrane.

1-4-1. Preparation of defect-free MOF membranes for gas separation

Although the number of published MOF structures has increased explosively during the last decade, the number of reported MOF membranes has slowly increased. Because preparing high quality MOF membranes is still challenging, which limits the development of MOF membranes. Nevertheless, many scientists have developed some creative methods in the fabrication of MOF membranes such as direct growth, layer-by-layer growth, secondary growth (seeded growth), chemical solution deposition, and electrospinning technology. [50-53] MOF materials generally need to be supported by porous substrates due to their inherent limited mechanical strength for membrane formation. Among them, the porous carriers are mainly metal oxides such as alumina, titanium dioxide, and zinc oxide, and porous polymers. The most commonly used methods for preparing MOF membranes are direct growth and secondary growth. Direct growth is to directly immerse the substrate into the growth solution. The nucleation, growth, and intergrowth of crystals on the substrate all proceed during the preparation procedure. However, because of the poor bonding between the crystals and substrate [54], only a few MOF membranes were reported without modifying the porous support. Chemical

modification of the substrate is an effective strategy to improve the heterogeneous nucleation of MOF crystals on the surface of the substrate. For example, Caro et al. [55] reported a covalent functionalization strategy for the construction of ZIF-90 membrane using 3-aminopropyltriethoxysilane (APTEs) as covalent linkers between the ZIF-90 membrane and the Al_2O_3 substrate. The ethoxy groups of the APTEs can react with the hydroxyl groups at the surface of the Al_2O_3 substrate to obtain amino groups, the aldehyde groups from ligand of ZIF-90 can react with amino groups via imine condensation (**Figure 1-10)**. In this way, ZIF-90 crystals can form a dense membrane on the surface of the substrate. As shown in **Figure 1-11,** ZIF-90 membrane exhibits high H_2 permeability than CO_2, N_2, and CH_4. Later studies [56, 57] demonstrated that the amino groups on the surface of Al_2O_3 substrate also can promote the preparation of MOFs based on the carboxylic acid ligand.

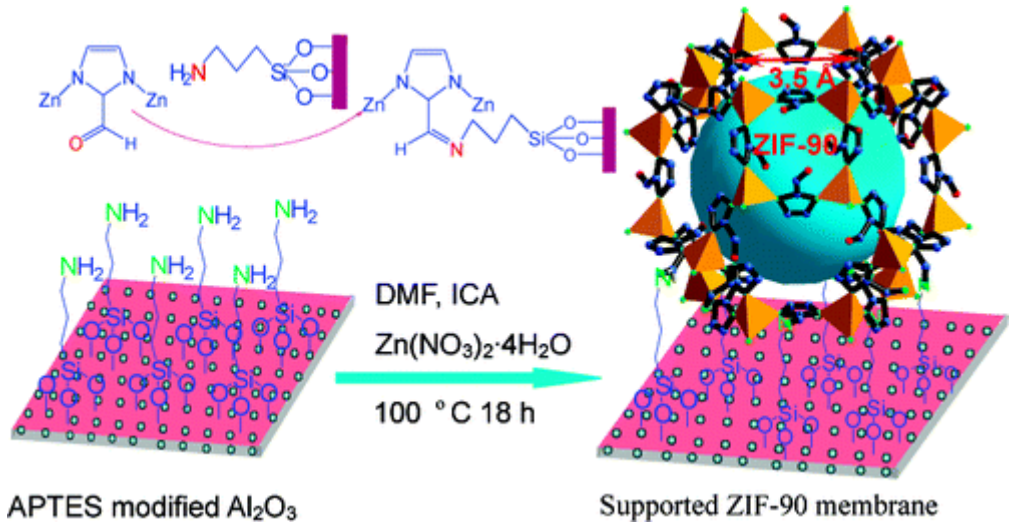

Figure 1-10. Scheme for preparing ZIF-90 membranes using 3-aminopropyltriethoxysilane (APTEs) as a covalent linker between a ZIF-90 membrane and an Al_2O_3 support via an imine condensation reaction. Copyright (2010) American Chemical Society.

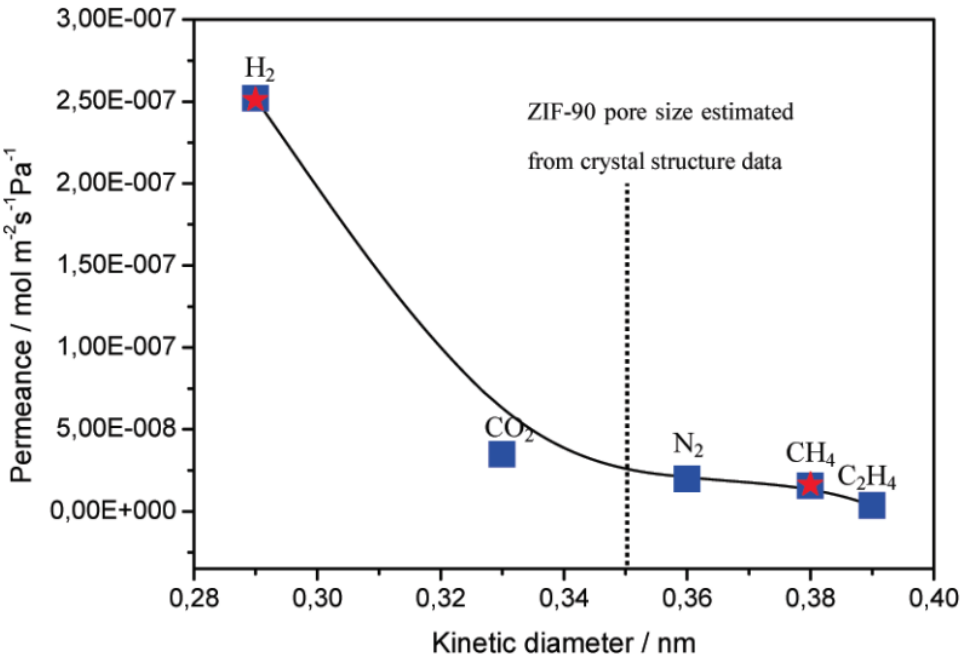

Figure 1-11. Single gas permeances of different gases on the ZIF-90 membrane at 200 °C as a function of their kinetic diameter. The pentacles show the permeances of H_2 and CH_4 from an equimolar binary mixture. Copyright (2017) American Chemical Society.

Secondary growth (also called seeded growth) is the most commonly used method for preparing MOF membranes. In this method, pre-synthesized nanosized crystalline seeds are coated on the surface of the substrate and immerse the substrate with the crystalline seeds into the precursor solution. During the synthesis process, the pre-coated seeds provide nucleation centers, thus separating the nucleation step and growth step of crystal growth. This method allows for shorter reaction times and better control of the membrane structure. [58] The challenge of secondary growth for membrane preparation is how to effectively immobilize the nanoscale MOF crystalline seeds on the substrate to provide uniform nucleation sites. The preparation of a uniform seed layer becomes the critical process of this method. For instance, Jin's group [59] developed a facile technique which is called reactive seeding method. In this technique, the seed layer was created by the reaction between the Al_2O_3 substrate and the organic precursor, then the membrane was fabricated by secondary growth (**Figure 1-12**). Single-gas permeation results

indicated that the MIL-53 membrane has a high intensity and it shows high selectivity for dehydration. The secondary growth method proved to be essential for achieving uniform and well intergrowth of MOF membrane.

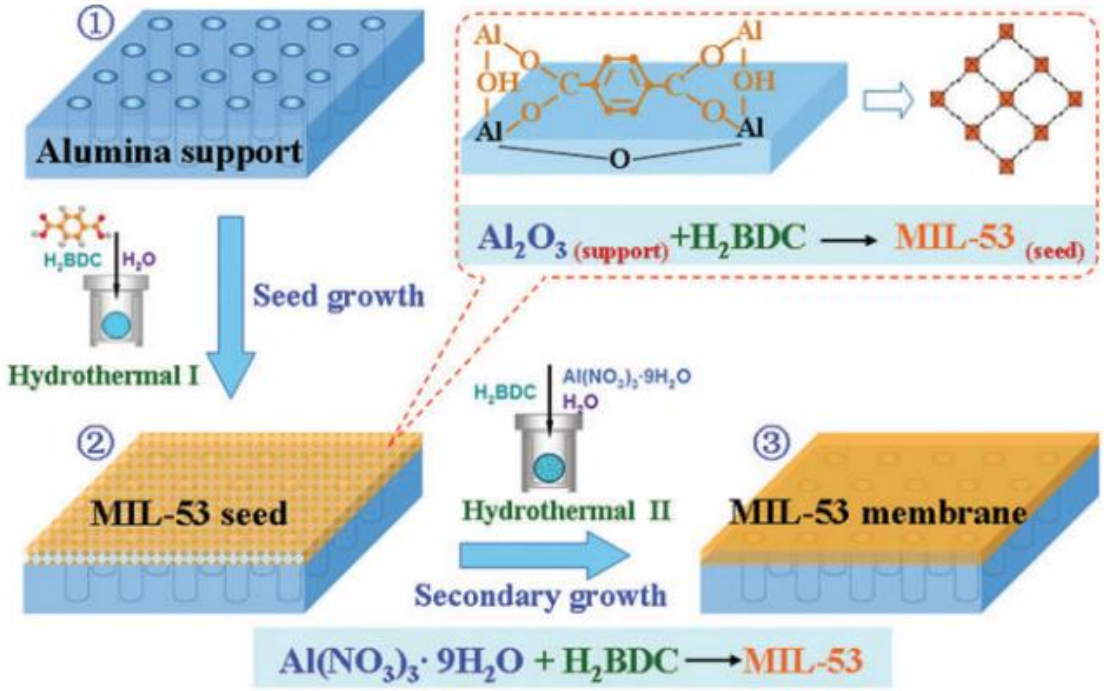

Figure 1-12. Schematic diagram of the preparation of the MIL-53 membrane on alumina support via the RS method. Copyright (2011) Royal Chemical Society.

In addition to the above two methods, layer-by-layer growth is suitable for the preparation of some MOF membranes that can be nucleated rapidly at room temperature or low temperature. [60, 61] Chemical solution deposition and electrospinning technology are suitable for some specific MOFs that can be synthesized by vapor phase deposition or electrochemical reaction [62, 63], which limits its wide range of applications. In short, the development of high quality MOF membranes has not been as rapid as that of MOFs due to the influence of the synthesis conditions and the weak bonding between MOF crystals and the substrate. The development of new MOF membranes with high quality is a worthwhile research topic, since MOF membranes can be used not only for molecules separation but also for catalysis, sensing, and fluorescence.

1-4-2. Crystal orientation control in MOF membranes

Crystal orientation in MOF membrane will affect the diffusion of gases. Unlike polymer membranes which rely on dissolving gas molecules for permeation, it is difficult for gas to pass through the membrane when the crystal grows in the direction of the absence of pores. Direct synthesis of MOF membranes with orientation is more difficult because the growth direction of crystals on the substrate is difficult to control. Most of the directly synthesized MOF membranes are randomly grown. How to develop a defect-free MOF membrane with controllable microstructure remains a big challenge, especially for MOFs which has 1D channels. Because the gas can only diffuse in the pore from one side so it is especially important to control the growth of crystal orientation. Fang et al. [64] developed a few-molecular-layer thin metal-organic framework (MOF) nanosheets without using surfactant by direct synthesis method. It is also the first time to achieve a highly oriented and flexible MOF membrane. In this method, highly oriented nanosheets are directly filtered by vacuum filtration to obtain epitaxially oriented membranes with stacking along the c-axis of the crystal structure (**Figure 1-13)**.

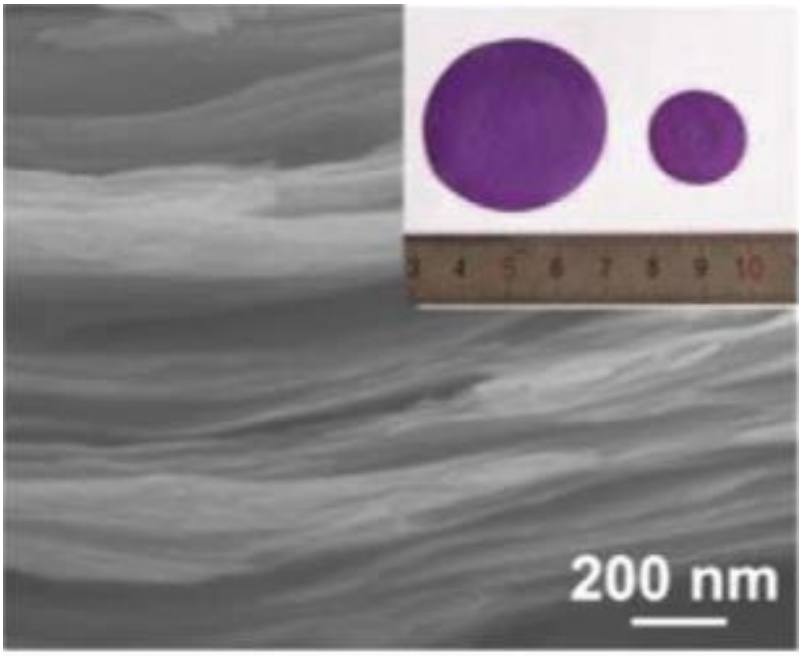

Figure 1-13. Cross-section SEM image of the Cu_2(CuTCPP) membrane. Copyright (2019) Elsevier.

Preparation of oriented membrane from oriented seed layer is a feasible way since the oriented seed provided a nucleation center where the membrane can be grown along the crystal direction of the seed crystals during secondary growth. Liu's group [65] developed a (111)-oriented UIO-66 membranes through pre-deposition of a (111)-oriented UIO-66 seed layer. Firstly, they used a dynamic air-liquid interface-assisted assembly technology to deposit an oriented seed monolayer, then an oriented UIO-66 membrane was prepared by secondary growth. Similar work also reported from Liu's group, a highly c-oriented NH_2-MIL-125 membrane [66] was prepared on porous α-Al_2O_3 substrates by combining oriented seeding and controlled in-plane epitaxial growth **(Figure 1-14)**. Huang et al. [67] also achieved in-plane epitaxial growth of the ZIF-95 seed layer by vapor-assisted in-plane epitaxial growth method, resulting in oriented and well-intergrown ZIF-95 membrane. In addition to the preparation of highly oriented seed layers using some techniques, the direct synthesis of some seed crystals with orientation is also a method to prepare oriented membranes. For example, the typical crystal morphology of the ZIF-69 hexagonal prism elongated along the c-axis, causing the c-axis of the rod-shaped crystals to be easily parallel to the base because the rod-shaped crystals tend to "lie on the substrate". Lai et al. [68] synthesized ZIF-69 seeds which look like a flat hexagonal prism with two hexagonal pyramid heads, in which most of the hexagonal face (c-face) would be facing upwards (**Figure 1-15)**. The c-oriented seed layer successfully helped prepare the c-oriented ZIF-69 membrane during secondary growth.

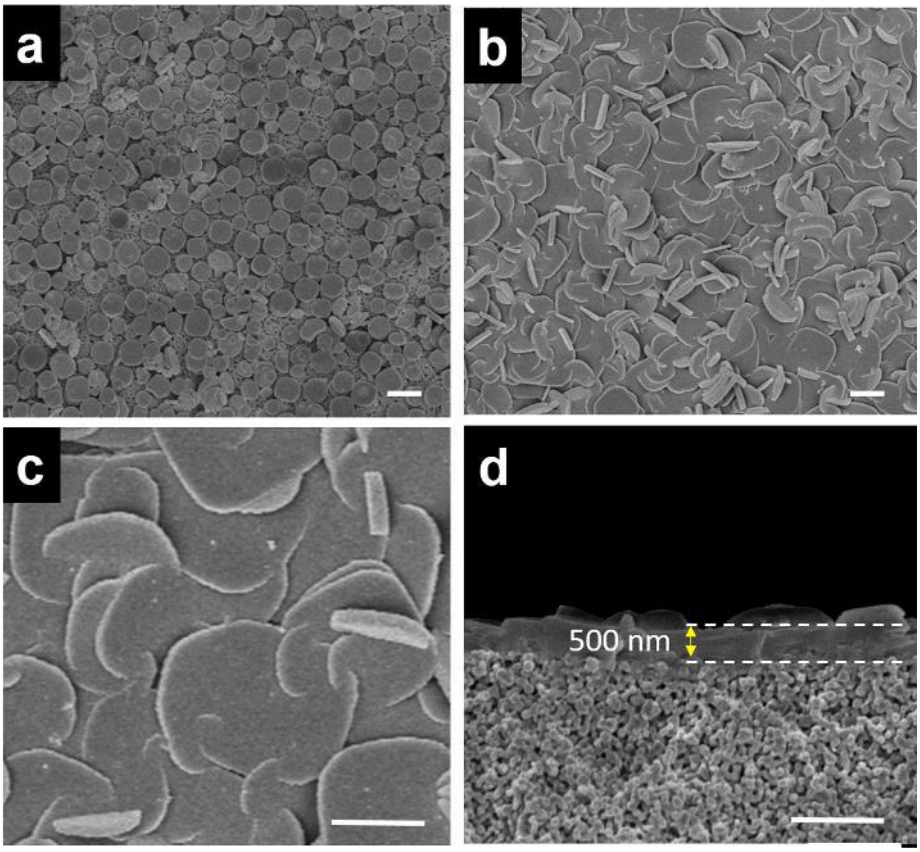

Figure 1-14. SEM images of a) prepared NH_2-MIL-125(Ti) seed layer; b, c) top and d) cross-section of prepared NH_2-MIL-125(Ti) membrane after secondary growth on the α-Al_2O_3 substrate. Scale bar: 1 μm. Copyright (2018) Wiley Online Library.

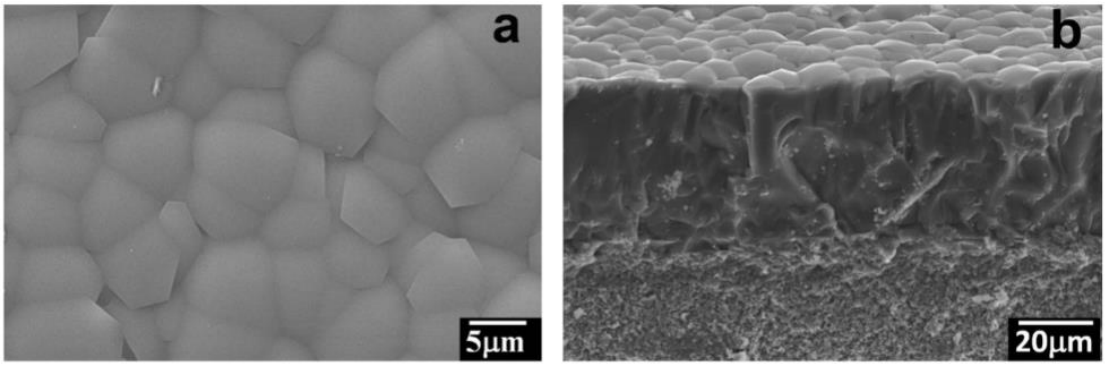

Figure 1-15. (a) Top view of ZIF-69 membrane by secondary growth. (b) Cross-section view of ZIF-69 membrane by secondary growth. Copyright (2011) Elsevier.

In some cases, randomly seed crystals can also be used to prepare oriented membranes, especially for some 2D MOFs. Because the growth rate of each axis of 2D MOFs is different, there may be a tendency for the growth direction during the growth

process. Wang et al. [69] reported a b-axis-oriented ZIF-L membrane-based random seeds. The ZIF-L crystals are a 2D leaf-shaped structure with a longer b-axis length than the a-axis and c-axis, so the preferred orientation can be ascribed to the fastest growth along the b-axis in the secondary growth. During in the secondary growth process, the crystals with the b-axis parallel or almost parallel to the substrate surface will have competition for space with their lateral neighbors. Due to the fastest growth along the b-axis, they will grow upright and their b-axis is upright on the substrate in order to obtain enough space for growth (**Figure 1-16)**. Even though the pore channels are parallel to the c-axis, the gas can diffuse through the pathway of ZIF-L between the adjacent layers due to the flexibility of the 2D ZIF-L. Interestingly, after PEI modification of the substrate, a c-axis-oriented ZIF-L layer was successfully obtained by filtration-deposition and c-axis-oriented ZIF-L film was prepared through secondary growth (**Figure 1-17)**, so the gas can be sieved by the pore of the ZIF-L.

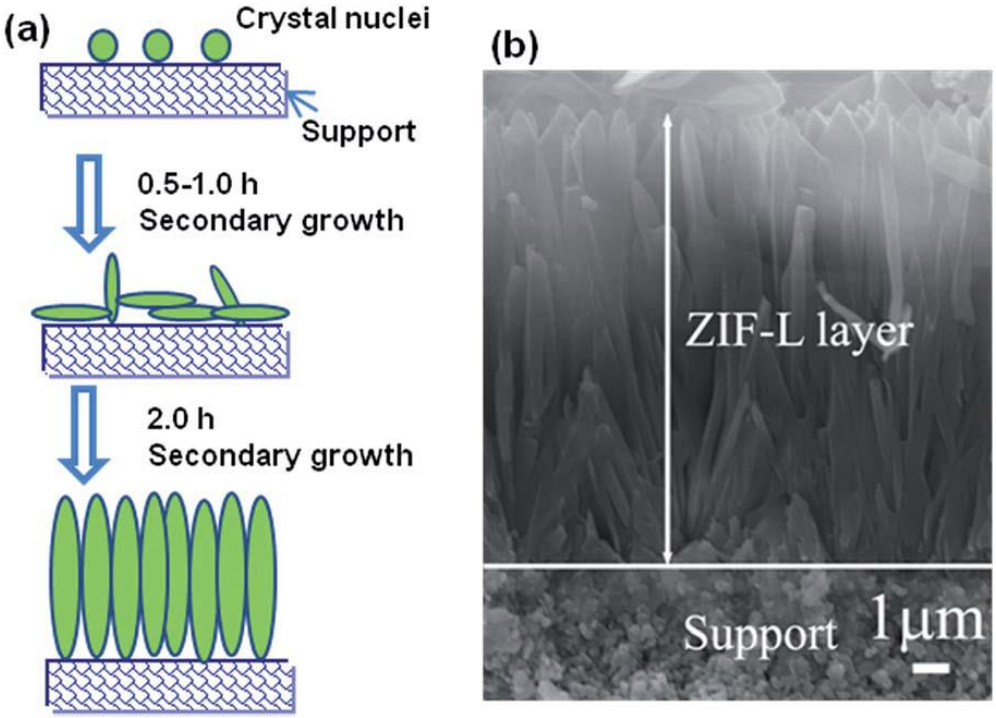

Figure 1-16. Schematic illustration of b-oriented ZIF-L film formation (a), the cross-sectional SEM image of the ZIF-L film (b). Copyright (2015) Royal Chemical Society.

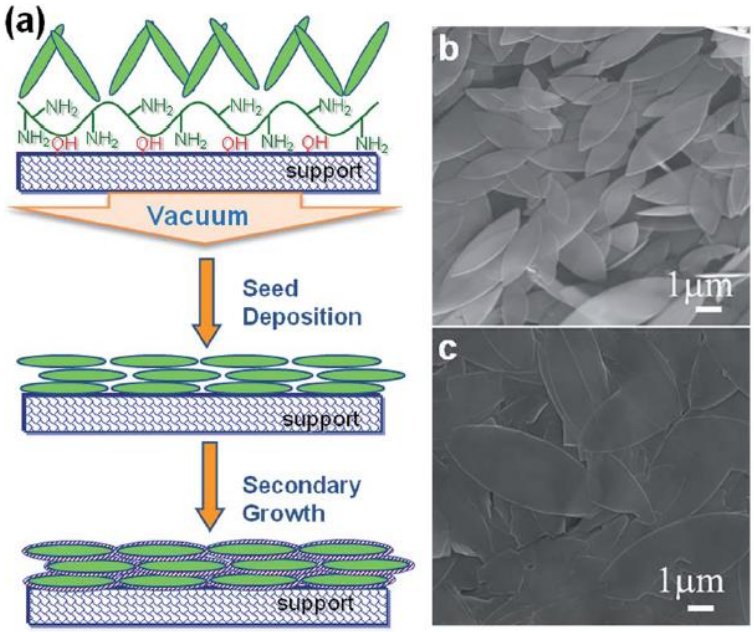

Figure 1-17. (a) Schematic illustration of PEI-assisted filtration-deposition of ZIF-L and the secondary growth, (b) SEM images of ZIF-L seeding after vacuum filtration, (c) ZIF-L membranes after 0.5 h of secondary growth. Copyright (2015) Royal Chemical Society.

Similarly, Yang et al. [70] developed a highly oriented ZIF-7 membrane from randomly oriented seed layers through effectively controlling the crystal size and morphology of MOF crystals and manipulating the orientation of MOF membrane through evolutionary selection in a Van der Drift-type growth. The randomly oriented seed layer of ZIF-7 crystal is nearly spherical in shape, while they prepared oriented membranes by modulating the morphology of ZIF-7 into a nanorod-like structure to control the direction of membrane growth (**Figure 1-18)**. Then the MOF nanorods will grow into the oriented film along the direction of 101.

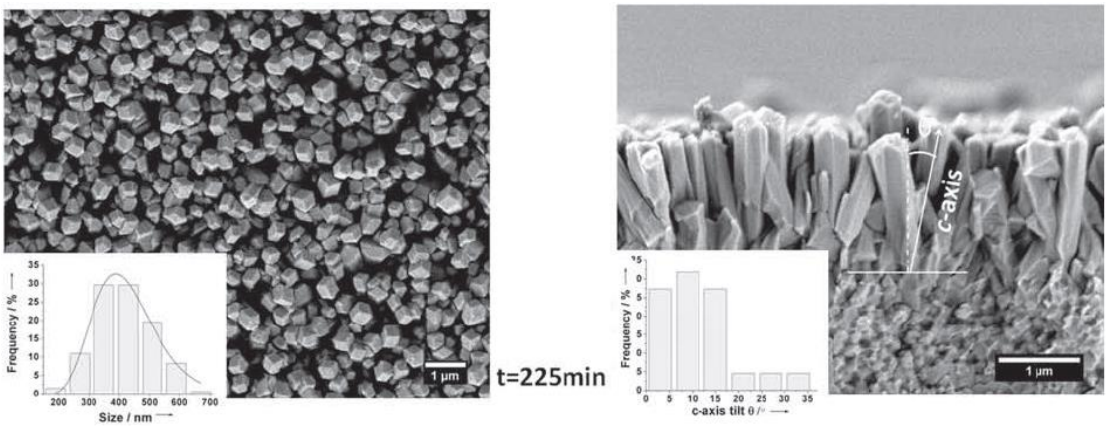

Figure 1-18. SEM top views and cross sections of the ZIF-7 membranes obtained after 225 min. Copyright (2010) Wiley Online Library.

For some 2D MOFs, it is difficult to control the growth along with the c-axis since the large aspect ratio of the a-axis and b-axis. Instead, the preparation of a-axis or b-axis oriented membrane becomes much easier. So some researchers utilize the interlattice of 2D sheet through vertically aligning nanocrystals to construct dense membranes. Nunes et al. [71] synthesized an oriented and vertically grown ZIF-L membrane on a polymeric mesoporous support. The vertically aligned nanochannels between the interlattice of ZIF-L can effectively separate H_2 and other gases **(Figure 1-19)**, and the H_2/C_3H_8 separation factor can reach 516. Coincidentally, Caro's group [72] also fabricated vertically aligned 2D covalent organic framework (COF) layers as gas separation membranes, the gas transport channels are straight slit-like pore channels formed by the distance between the interlayers of parallel 2D COF sheets. The distance between COF layers is usually 0.3-0.4 nm, which is more suitable for H_2 separation than nm-sized pore apertures.

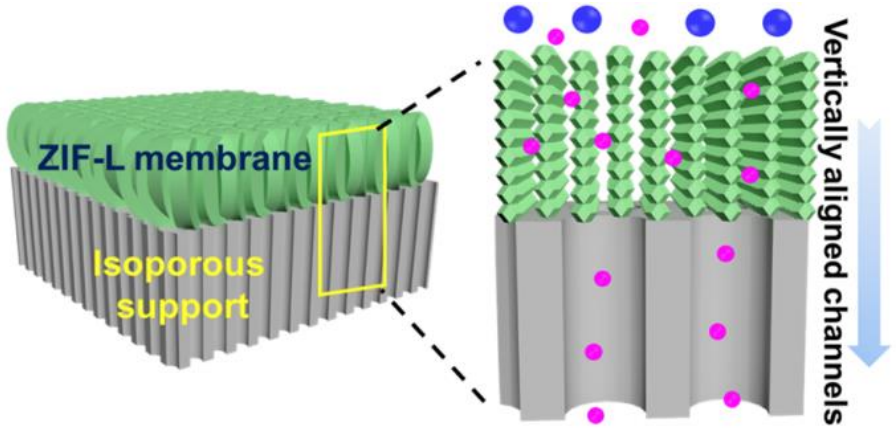

Figure 1-19. Molecular transport mechanism in the ZIF-L membrane. Copyright (2020) American Chemical Society.

In all studies of oriented membranes, the orientation of the crystal is very important for MOFs containing 1D channels. The direction of the channel can directly influence gas transportation, especially for 3D structured MOFs possessing 1D pores. However, for some 2D layered MOFs, even if the oriented growth is parallel to the growth direction of the substrate, there is a possibility of gas transport through the interlayer because of its flexible structure.

1-5. Significance and purpose of this thesis

MOFs can be flexibly adjusted the pore size at the molecular level and also can realize the chemical modification of pore channels through the functionalization of organic ligands, which makes them exhibit promising applications in adsorption, separation, and membrane-based applications. The purpose of this thesis is to synthesize MOFs for selective adsorption of gases by controlling the structure of MOF crystals and to prepare MOF membranes for gas separation by adjusting the crystal growth. In this thesis, a MOF that can capture O_2 from the air and reversibly release the captured O_2 at high temperatures was synthesized through controlling reaction conditions. Although many researchers have developed MOFs with interaction bonding sites for gas adsorption and separation. However, rare MOFs have been reported to capture oxygen from the air.

The separation of oxygen, argon, and nitrogen are difficult by membrane separation because the molecular kinetic diameter of them are similar (O_2 ≈ 0.35 nm, Ar ≈ 0.34 nm, N_2 ≈ 0.36 nm). Moreover, the boiling points of oxygen and argon are also very close (O_2 ≈ -183 °C, Ar ≈ -185.8 °C), making it difficult to separate oxygen and argon even by distillation. Therefore, this thesis is very meaningful for separating oxygen from the air. In addition, this thesis also developed a series of 3D and stable MOFs with excellent CO_2/N_2 and C_2H_2/C_2H_4 separation performance.

Despite the great progress in the field of MOFs, the application of MOF membranes is still in its infancy. Crystallization of MOFs on porous substrates has been a challenge for the fabrication of such MOF membranes is to construct defect-free MOF layers, which is often difficult due to the poor adhesion bond between MOF crystals and the surface of a substrate. So controlling the growth of MOF crystals is particularly important: Not only orientation control but also control of crystal intergrowth. This thesis also focuses on controlling the growth of 2D Cu(II) based MOF crystals on substrates into membranes for gas separation. A defect-free membrane with favorable crystal orientation was prepared for efficient H_2 separation. Two high-quality heterobilayer membranes from isostructural MOFs also were constructed for CO_2/N_2 and CO_2/CH_4 separation. Therefore, this thesis contributes to not only clear guides towards designing MOFs for gas selective adsorption but also the fabrication of membrane for gas separation.

1-6. References

1 H.J. Buser, D. Schwarzenbach, W. Petter, A. Ludi, *Inorg. Chem.*, 1977, **16**, 2704-2710.

2 A.F. Wells, Structural inorganic chemistry (fifth ed), *Oxford University*, 1984.

3 B.F. Hoskins, R. Robson, *J. Am. Chem. Soc.*, 1989, **111**, 5962-5964.

4 B.F. Abrahams, B.F. Hoskins, R. Robson, *Chem. Commun.*, 1990, 60-61.

5 R. Matsuda, R. Kitaura, S. Kitagawa, Y. Kubota, T. C. Kobayashi, S. Horike, M. Takata, *J. Am. Chem. Soc.*, 2004, **126**, 14063-14070.

6 Y. Inubushi, S. Horike, T. Fukushima, G. Akiyama, R. Matsuda, S. Kitagawa, *Chem. Commun.*, 2010, **46**, 9229-9231.

7 H. Yang, T. X Trieu, X. Zhao, Y. Wang, *Nanoscale*, 2018, **10**, 6205-6211.

8 H. Yang, T. X Trieu, X. Zhao, Y. Wang, P. Feng, X. Bu, *Angew. Chem. Int. Ed.*, 2019, **58**, 11757-11762.

9 L. Zhu, X.Q. Liu, H.L. Jiang, L.B. Sun, *Chem. Rev.*, 2017, **117**, 8129-8176.

10 M. Mon, R. Bruno, J. Ferrando-Soria, L. Bartella, L. Di Donna, M. Talia, R. Lappano, M. Maggiolini, D. Armentano, E. Pardo,. *Mater. Horiz.*, 2018, **5**, 683-690.

11 N. Stock, S. Biswas, *Chem. Rev.*, 2012, **112**, 933-969.

12 S. Kitagawa., *Chem. Soc. Rev.*, 2014, **43**, 5415-5418.

13 M. Eddaoudi, J. Kim, N. Rosi, D. Vodak, J. Wachter, M. O'Keeffe, O. M. Yaghi, *Science*, 2002, **295**, 469-472.

14 J. Gascon, F. Kapteijn, *Angew. Chem. Int. Ed.*, 2010, **49**, 1530-1532.

15 Y. Li, R.T Yang, *Langmuir*, 2007, **23**, 12937-12944.

16 M.A Moreira, J.C Santos, A.F.P Ferreira, J.M Loureiro, F. Ragon, P. Horcajada, K.E. Shim, Y.K. Hwang, U.H Lee, J.S. Chang, C. Serre, A.E. Rodrigues, *Langmuir*, 2012, **28**, 5715-5723.

17 L. Valenzano, B. Civalleri, S. Chavan, G. T. Palomino, C. O. Areán, S. Bordiga, *J. Phys. Chem. C*, 2010, **114**, 11185-11191.

18 P.L. Llewellyn, S. Bourrelly, C. Serre, A. Vimont, M. Daturi, L. Hamon, G.D. Weireld, J.S. Chang, D.Y. Hong, Y.K. Hwang, S.H. Jhung, G. Férey, *Langmuir*, 2008, **24**, 7245-7250.

19 D.A. Berry, K.M. Ng, *AIChE J*, 1997, **43**, 1751-1762.

20 G. Naidu, S. Jeong, M.A.H Johir, A.G Fane, J. Kandasamy, S. Vigneswarana, *Water Res.*, 2017, **123**, 321-331.

21 I. Ahmed, S.H. Jhung, *Chem. Eng. Sci.*, 2017, **310**, 197-215.

22 H. Strathmann, *AIChE J.*, 2001, **47**, 1077-1087.

23 S. Kitagawa, R. Kitaura, S. Noro, *Angew. Chem. Int. Ed.*, 2004, **43**, 2334-2375.

24 X. Peng, W. Wang, R. Xue, Z. Shen, *AIChE J*, 2006, **52**, 994-1003.

25 F.M.A. Noa, M. Abrahamsson, E. Ahlberg, O. Cheung, C.R. Göb, C.J. McKenzie, L. Öhrström, *Chem*, 2021, **7**, 2491-2512.

26 O. Barreda, G. Bannwart, G.P.A Yap, Eric D. Bloch, *ACS Appl. Mater. Interfaces*, 2018, **10**, 11420-11424.

27 D. O'Nolan, A. Kumar, M.J. Zaworotko, *J. Am. Chem. Soc.*, 2017, **139**, 8508-8513.

28 O. Shekhah, Y. Belmabkhout, K. Adil, P.M. Bhatt, A.J. Cairns, M. Eddaoudi, *Chem Commun*, 2015, **51**, 13595-13598.

29 A. Huang, L. Wan, J. Caro, *Mater. Res. Bull.*, 2018, **98**, 308-313.

30 Z. Niu, X. Cui, T. Pham, G. Verma, P.C. Lan, C. Shan. H. Xing, K.A. Forrest, S. Suepaul, B. Space, A. Nafady, A.M. Al-Enizi, S. Ma, *Angew. Chem. Int. Ed.*, 2021, **133**, 5343-5348.

31 K.J. Chen, H.S. Scott, D.G. Madden, T. Pham, A. Kumar, A. Bajpa, M. Lusi, K.A. Forrest, B. Space, J.J. PerryIV, M.J. Zaworotko, *Chem*, 2016, **1**, 753-765.

32 Q.L. Qian, X.W. Gu, J. Pei, H.M. Wen, H. Wu, W. Zhou, B. Li, G. Qian, *J. Mater. Chem. A*, 2021, **9**, 9248-9255.

33 R. Matsuda, R. Kitaura, S. Kitagawa, Y. Kubota, R.V. Belosludov, T.C. Kobayashi, H. Sakamoto, T. Chiba, M. Takata, Y. Kawazoe, Y. Mita, *Nature*, 2005, **436**, 238 – 241.

34 Y. Chen, Z. Qiao, D. Lv, C. Duan, X. Sun, H. Wu, R. Shi, Q. Xia, Z. Li, *Chem. Eng. J.*, 2017, **328**, 360-367.

35 R.W. Flaig, T.M. O. Popp, A.M. Fracaroli, E.A. Kapustin, M.J. Kalmutzki, R.M. Altamimi, F. Fathieh, J.A. Reimer and O.M. Yaghi, *J. Am. Chem. Soc.*, 2017, **139**, 12125–12128.

36 M. Fujimura, S. Kusaka, A. Masuda, A. Hori, Y. Hijikata, J. Pirillo, Y. Ma, R. Matsuda, *Small*, 2021, **17**, 2004351.

37 S. Adhikari, S. Fernando, *Ind. Eng. Chem. Res.,* 2006, **45**, 875-881.

38 M.T. Ravanchi, T. Kaghazchi, A. Kargari, *Desalination*, 2009, **235**, 199-244.

39 H. Strathmann. *J. Membr. Sci.*, 1981, **9**, 121-189.

40 Y. Huang, R.W Baker, *Ind. Eng. Chem. Res.*, 2010, **49**, 3760-3768.

41 L.M. Robeson, *Curr Opin Solid State Mater Sci.*, 1999, **4**, 549-552.

42 G. Maier, *Angew. Chem. Int. Ed.,* 1998, **37**, 2960-2974.

43 K.W Lee, B.K Seo, S.T Nam, M.J Han, *Desalination*, 2003, **159**, 289-296.

44 W.H. Lee, J.G Seong, X. Hu, *J. Polym. Sci.*, 2020, **58**, 2450-2466.

45 H.B. Park, J. Kamcev, L.M Robeson, M. Elimelech, B.D. Freeman, *Science*, 2017, **356**, eaab0530.

46 R. Swaidan, B. Ghanem, E. Litwiller, I. Pinnau, *Macromolecules*, 2015, **48**, 6553-6561.

47 T. Tomita, K. Nakayama, H. Sakai, *Micropor Mesopor Mat*, 2004, **68**, 71-75.

48 W.C Wong, L.T.Y Au, C.T Ariso, K.L Yeung, *J. Membr. Sci.*, 2001, **191**, 143-163.

49 X. Xu, W. Yang, J. Liu, L. Lin, *Adv. Mater.*, 2000, **12**, 195-198.

50 Y. Liu, Z. Ng, E. A. Khan, H-K. Jeong, C.b. Ching, Z. Lai, *Micropor Mesopor Mat*, 2009, **118**, 296–301.

51 H. Guo, Y. Zhu, S. Qiu, J.A. Lercher, H. Zhang, *Adv. Mater.*, 2010, **22**, 4190–4192.

52 L. Fan, M. Xue, Z. Kang, H. Li, S. Qiu, *J. Mater. Chem.*, 2012, **22**, 25272–25276.

53 V. Chernikova, O Shekhah, Y Belmabkhout, M. Eddaoudi, *ACS Appl. Nano Mater.*, 2020, **3**, 6432-6439.

54 Y.S. Li, F.Y. Liang, H. Bux, A. Feldhoff, W. Yang, J. Caro, *Angew. Chem. Int. Ed.,* 2010, **122**, 558-561.

55 A. Huang, W. Dou, J. Caro, *J. Am. Chem. Soc.*, 2010, **132**, 15562–15564.

56 B. Ghalei, K. Wakimoto, C.Y. Wu, A.P. Isfahani, T. Yamamoto, K. Sakurai, M. Higuchi, B.K. Chang, S. Kitagawa, E. Sivaniah, *Angew. Chem. Int. Ed.*, 2019, **58**, 19034-19040.

57 M. Mozafari, S.F. Seyedpour, S.K. Salestan, A. Rahimpour, A.A. Shamsabadi, M.D. Firouzjaei, M.R. Esfahani, A. Tiraferri, H. Mohsenian, M. Sangermano, M. Soroush, *J. Membr. Sci.*, 2019, **588**, 117200.

58 Y. Yoo, Z. Lai, H.K. Jeong, *Micropor Mesopor Mat*, 2009, **123**, 100-106.

59 Y. Hu, X. Dong, J. Nan, W. Jin, X. Ren, N. Xu, Y.M. Lee, *Chem Commun*, 2011, **47**, 737-739.

60 Y. Ma, Z. Dong, M. You, Y. Zhang, X. Feng, X. Ma, J. Meng, *Chem Commun*, 2019, **55**, 10146-10149.

61 X. Wang, S. Kusaka, A. Hori, R. Matsuda, *Chem. Asian J.*, 2021, **16**, 2018-2021.

62 H.T. Kwon, H.K. Jeong, A.S. Lee, H.S. An, T. Lee, E. Jang, J.S. Lee, J. Choi, *Chem Commun*, 2016, **52**, 11669-11672.

63 X. Zhang, Y. Li, C.V. Goethem, K. Wan, W. Zhang, J. Luo, I.F.J. Vankelecom, J. Fransaer, *Matter*, 2019, **1**, 1285-1292.

64 M. Tian, F. Pei, M. Yao, Z. Fu, L. Lin, G. Wu, G. Xu, H. Kitagawa, X. Fang, *Energy Storage Mater.*, 2019, **21**, 14-21.

65 J. Yan, Y. Sun, T. Ji, L. Liu, M. Zhang, Y. Liu, *J. Membr. Sci.*, 2021, **635**, 119515.

66 Y. Sun, Y. Liu, J. Caro, X. Guo, C. Song, Y. Liu, *Angew. Chem. Int. Ed.,* 2018, **130**, 16320-16325.

67 X. Ma, Z. Wan, Y. Li, X. He, J. Caro, A. Huang, *Angew. Chem. Int. Ed.,* 2020, **59**, 20858-20862.

68 Y. Liu, G. Zeng, Y. Pan, Z. Lai, *J. Membr. Sci.*, 2011, **379**, 46-51.

69 Z. Zhong, J Yao, R Chen, Z Low, M He, JZ Liu, H. Wang, *J. Mater. Chem. A.,* 2015, **3**, 15715-15722.

70 Y. S. Li, H. Bux, A. Feldhoff, G.L. Li, W.S. Yang, J. Caro, *Adv.Mater.*, 2010, **22**, 3322-3326.

71 S. Wang, J. Liu, B. Pulido, Y. Li, D. Mahalingam, S.P. Nunes, *ACS Appl. Nano Mater.*, 2020, **3**, 3839-3846.

72 H. Fan, M. Peng, I. Strauss, A. Mundstock, H. Meng, J. Caro, *J. Am. Chem. Soc.*, 2020, **142**, 6872-6877.

Chapter 2

Trapping and Releasing Oxygen in the Air by Metal–Organic Framework with Light and Heat

2-1. Introduction

Metal-organic frameworks (MOFs) have attracted great attention in gas storage, [1,2] molecular recognition, [3] and catalysis, [4,5] due to their versatile structures and various potential applications. It is constructed from the blend of organic linkers, resulting in a three-dimensional (3D) skeletal structure embedded with metal-containing nodes. Trapping and releasing of oxygen have wide applications in many fields such as oxygen sensors, [6] medical, [7] and aerospace industries. [8] So far, porous carbons and the zeolite NaX have been widely studied for oxygen storage. [9,10] However, the activated carbons and zeolite are suffering from the disadvantage of poor control ability. Instead, the ability to tune the pore geometry and chemically controllability of MOFs make them excellent candidates for oxygen storage applications. [11-13] However, the adsorption of oxygen at ambient temperatures and 1 bar in MOFs is difficult to achieve due to the weak interactions between the MOFs and the oxygen. Therefore, it is necessary to develop MOFs with specific interaction ability for oxygen.

The SIFSIX (SIFSIX, hexafluorosilicate (SiF_6^{2-}) series MOFs grew rapidly in recent years and they have excellent CO_2 adsorption and acetylene/ethane separation.[14,15] These MOFs are synthesized by combining M^{2+} ions (e.g., Cu^{2+}, Zn^{2+}, Ni^{2+} or Co^{2+}.) with N-donor organic linkers to form a two-dimensional grid, then the grids are pillared with SiF_6^{2-} anions to form a porous and regular three-dimensional framework. 9,10-Di(4-pyridyl)anthracene (dpa) has photosensitizing and oxygen trapping abilities. it can be converted to 9,10-di(4-pyridyl)anthracene endoperoxide (epo) under UV-light (380 nm) irradiation in an oxygen environment. In this reaction, anthracene reacts with oxygen to form endoperoxide with singlet oxygen. [16,17] Interestingly, oxygen can be released from epo at high temperatures. Both the dpa and epo are suitable for the synthesis of SIFSIX MOFs since they possessed two pyridine moieties to form a coordination bond with metal ions, furthermore, the endoperoxide in epo can maintain in the structure because SIFSIX MOFs can be synthesized at room temperature.

In this work, we synthesized a series of new MOFs using $CoSiF_6$, $NiSiF_6$, $CdSiF_6$ and, $ZnSiF_6$ with dpa ligand. Compounds $[Ni(dpa)(H_2O)_4]\cdot SiF_6$ and $[Co(dpa)_2(CH_3OH)(SiF_6)]$ have 1D chain and 2D layer structure respectively. Compounds $[Cd(dpa)_2(SiF_6)]$ and $[Zn(dpa)_2(SiF_6)]$ have the 3D framework structure like SIFSIX series MOFs. $[Zn(dpa)_2(SiF_6)]$ can maintain stability after removal of the solvent and it exhibits the property of trapping oxygen under photoirradiation. We also synthesized two new MOFs using $ZnSiF_6$ and $CdSiF_6$ with epo ligand (Compounds $[Zn(epo)_2(SiF_6)]$ and $[Cd(epo)_2(SiF_6)]$). Oxygen bonded to anthracene ring can be observed from the single crystal structure, the endoperoxide of the two MOFs can release the oxygen at 140 ℃.

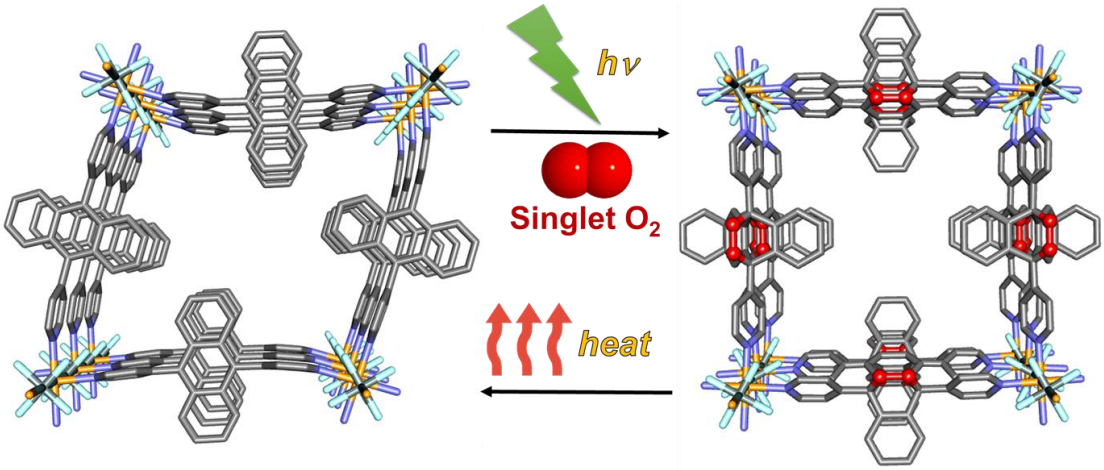

Graphic abstract

2-2. Experimental

Chemicals

Zinc hexafluorosilicate (Aldrich, 99%). Nickel hexafluorosilicate (Aldrich, 99%). Ethyl acetate (Nacalai, 99%). Methanol (wako, 99.8%). Ethanol (Wako, 99.5%). 1-Methyl-2-pyrrolidinone (TCI, 99%). 9,10-dibromoanthracene (TCI, 98%), Pyridine-4-boronicacid (Aldrich, 90%). K_2CO_3 (TCI, 99%), $Pd(PPh_3)_4$ (TCI, 97%), 1,2-Dimethoxyethane (Wako, 99.0%), $Cd(OH)_2$ (Wako, 95%), $Co(OH)_2$ (Wako, 56.0~64.0%),

H_2SiF_6 (Wako, 40.0~45.0%), Cadmium hexafluorosilicate was prepared through neutralizing fluorosilicic acid with Cadmium oxide and then filtering, evaporating, crystallization, centrifugal separation and drying. Cobalt hexafluorosilicate was obtained using the same method.

Synthesis of ligand 9,10-di(pyridine-4-yl)anthracene (dpa) and 9,10-di(4-pyridyl)anthracene endoperoxide (epo)

Dpa: 9,10-dibromoanthracene (500 mg, 1.50 mmol), Pyridine-4-boronicacid (440 mg, 3.50 mmol), K_2CO_3 (828 mg, 6.00 mmol), $Pd(PPh_3)_4$ (50 mg,0.04 mmol) and H_2O: DME: Ethanol (6 ml:10.5 ml:4.5 ml) were successively add to a 20 ml reaction vessels. The reaction mixture was heated to 160 ℃ in the microwave for 40 mins. After the reaction mixture was cooled to room temperature, ethyl acetate was added to dissolve the product then the catalyst was removed by filtering. Next, water was added to wash the solution and keep the ethyl acetate layer using a separator funnel. The removal of the solvent under reduced pressure yielded crude solid. The crude solid was dissolved in ethyl acetate again and purified by recrystallization, then the pale yellow crystals were obtained. Yield (250mg, 50%). ^{1}H NMR ($CDCl_3$-d^6, δppm): 8.879 (m, 4H, pyridine-2),7.609 (m, 4H, anthracene-1), 7.456 (m, 4H, pyridine-3), 7.405 (t,4H, anthracene-2).

Epo: Preparation of a solution by dissolving 500 mg dpa in 100ml acetone in a 100ml vial. The solution was irradiated with a UV lamp (144 W) for 8 h. Then evaporating the acetone to get the crude solid. After adding acetone to dissolve the solid again, the insoluble substance is the product that can be separated by filtration. ^{1}H NMR ($CDCl_3$-d^6, δppm): 8.934 (m, 4H, pyridine-2),7.623 (m, 4H, epidioxidoanthracene-1), 7.289 (m, 4H, pyridine-3), 7.145 (t,4H, epidioxidoanthracene-2).

Synthesis of single crystals

$[Zn(dpa)(CH_3OH)_2(H_2O)_2]\cdot SiF_6$: The single crystal of $[Zn(dpa)(CH_3OH)_2(H_2O)_2]\cdot SiF_6$ was synthesized as follows. Slow diffusion of a methanol solution of Zinc hexafluorosilicate (0.01 mM) into a chloroform solution of dpa (0.02 mM). colorless

blocks were obtained after 1 d.

$Zn(dpa)_2$ (SiF_6): Single crystals of $Zn(SiF_6)(dpa)_2$ were synthesized as follows. Slow diffusion of a methanol solution of Zinc hexafluorosilicate (0.01 mM) into a N-methylpyrrolidone(NMP) solution of dpa (0.02 mM). colorless blocks were obtained after 1 d. Powder samples of $Zn(SiF_6)_2(dpa)_2$ were synthesized as follows. 10 ml of Zinc hexafluorosilicate/MeOH solution (0.01 mM) was directly mixed with 10 ml of dpa/NMP solution (0.02 mM)

$Cd(dpa)_2(SiF_6)$, $([Ni(dpa)(H_2O)_4]\ SiF_6)$, and **$[Co(dpa)_2(CH_3OH)(SiF_6)]$:** They are synthesized using the same way with $Zn(dpa)_2((SiF_6)$, only changing the metal salt.

$Zn(epo)_2(SiF_6)$ and $Cd(epo)_2(SiF_6)$: The synthesis of single crystals and powder samples of $Zn(SiF_6)(epo)_2$ and $Cd(SiF_6)(epo)_2$ are the same as $Zn(SiF_6)(dpa)_2$, only just replacing the dpa with the epo.

Characterization and photoreaction experiment

Single crystal X-ray diffraction data were collected on a RIGAKU XtaLab P200 CCD system with VariMax Mo Optic with Mo$K\alpha$ radiation (λ = 0.71073 Å) and a confocal monochromator, with the constant temperature of 93 K by flowing low-temperature nitrogen gas. The structure was solved by direct methods and refined on F2 by full-matrix leastsquares methods using the SHELXTL package. All non-hydrogen atoms were refined with anisotropic thermal parameters. The hydrogen atoms attached to carbon positions were placed in geometrically calculated positions. ^{1}H NMR spectra measured on a Bruker AC 300 spectrometer at 300 MHz, using tetramethylsilane (δ = 0) as an internal reference. X-ray diffraction (XRD) patterns of the samples were measured by a Rigaku X-ray diffractometer with Cu $K\alpha$ radiation. TGA was performed using a Rigaku TP-EVO2 SL DyTG/DTA TypeJ under N_2 stream scanning from 30 ℃ to 500 ℃ with the temperature ramp of 5 ℃/min. UV-visible absorption spectra for samples were recorded on a JASCO model V-650 spectrophotometer. The UV irradiation device using UV-light in 380 nm at 25 °C and 24% relative humidity.

2-3. Results and discussion

Crystal structure of MOFs based dpa ligand

We first synthesized the MOF crystals using $ZnSiF_6$ and dpa in $CHCl_3$/Methanol solution which was widely applied for the synthesis of other SIFSIX series MOFs. However, due to the coordination of H_2O and CH_3OH to the metal, the SiF_6^{2-} linkers failed to connect the metal (**Figure 2-1**). We found that N-methylpyrrolidone (NMP) can form CH-π interactions with benzene rings, so we chose NMP/methanol solution to synthesis SIFSIX crystals. As expected, we have successfully synthesized the 3D porous SIFSIX pillared MOFs using $ZnSiF_6$ and dpa, as shown in **Figure 2-2**, the NMP molecule forms CH-π bond (3.6 Å) with dpa and serves as a bridge between two dpa. The SiF_6^{2-} linkers successfully bridge the two-dimensional sheet created by Zn^{2+} and dpa ligand forming a 3D compound $[Zn(dpa)_2(SiF_6)]$ with a monoclinic space group *P 2₁/c*.

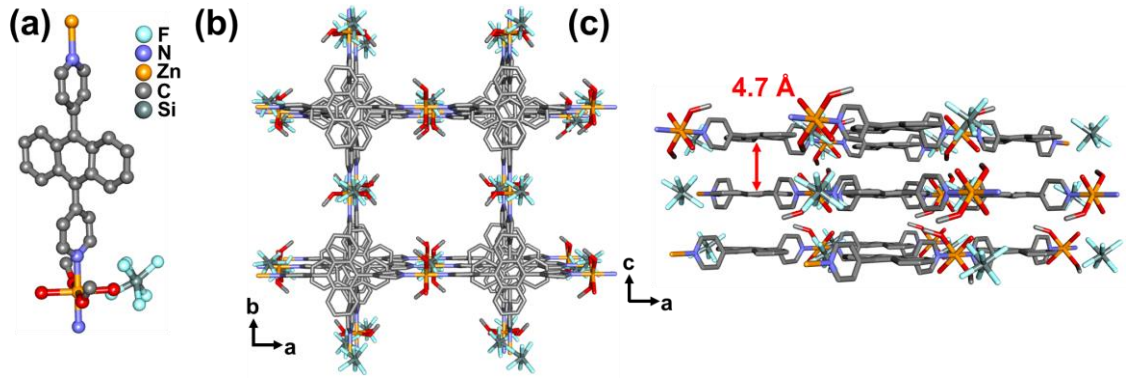

Figure 2-1. Crystal structures of $[Zn(dpa)(H_2O)_4]\cdot SiF_6$: coordination environment around the zinc(II) center (a), Packing structure viewed along [110] (b) and [101] (c).

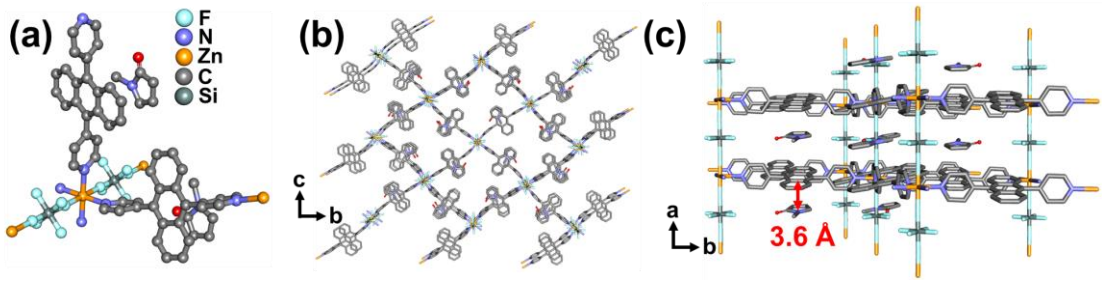

Figure 2-2. Crystal structures of $[Zn(dpa)_2(SiF_6)]$: coordination environment around the zinc(II) center (a), Packing structure viewed along [011] (b) and [110] (c).

Subsequently, other MOFs also were obtained by slow diffusion of a methanol solution of different metal hexafluorosilicate into an NMP solution of dpa/epo at room temperature. Single-crystal X-ray diffraction analysis reveals that compound $[Ni(dpa)(H_2O)_4]\cdot SiF_6$ crystallizes in a tetragonal system with the *P 4₂/mnm* space group. As shown in **Figure 2-3** (a)-(c), the nickel (II) ion is six-coordinated by two nitrogen atoms from dpa ligand and four H_2O molecules. The ligands link the nickel(II) centers to form a 1D chain, which is stabilized by the interactions between anthracene of dpa stacking to 3D networks. The grids with a size of 16.192 Å ×16.192 Å (Ni−Ni distance) are filled by free SiF_6^{2-} dianions having interactions with the coordinated H_2O molecules by hydrogen bonds (O···F 1.926 Å).

Compound $[Co(dpa)_2(CH_3OH)(SiF_6)]$ crystallize in the orthorhombic space group *C m c e*. The cobalt(II) center is coordinated with four nitrogen atoms of dpa in the equatorial plane while the axial positions are occupied by one oxygen atom of water, and one fluorine atom from SiF_6^{2-} anion (**Figure 2-3** (d)-(f)). In this case, the SiF_6^{2-} linkers don't serve as a bridging chain to link the 2D sheet. Instead, the sheets pack together by interactions between anthracene of dpa leading to a non-porous structure. Interestingly, in the structure of compound $[Cd(dpa)_2(SiF_6)]$ has a similar coordination environment with $[Zn(dpa)_2(SiF_6)]$, the SiF_6^{2-} linkers successfully bridge the two-dimensional sheet created by Cd^{2+} and dpa ligand forming a 3D network (**Figure 2-3** (g)-(i)), but the monoclinic space group *C 2/m*, which is different with $[Zn(dpa)_2(SiF_6)]$. Crystallographic parameters of those compounds were shown in **Table 2-1.**

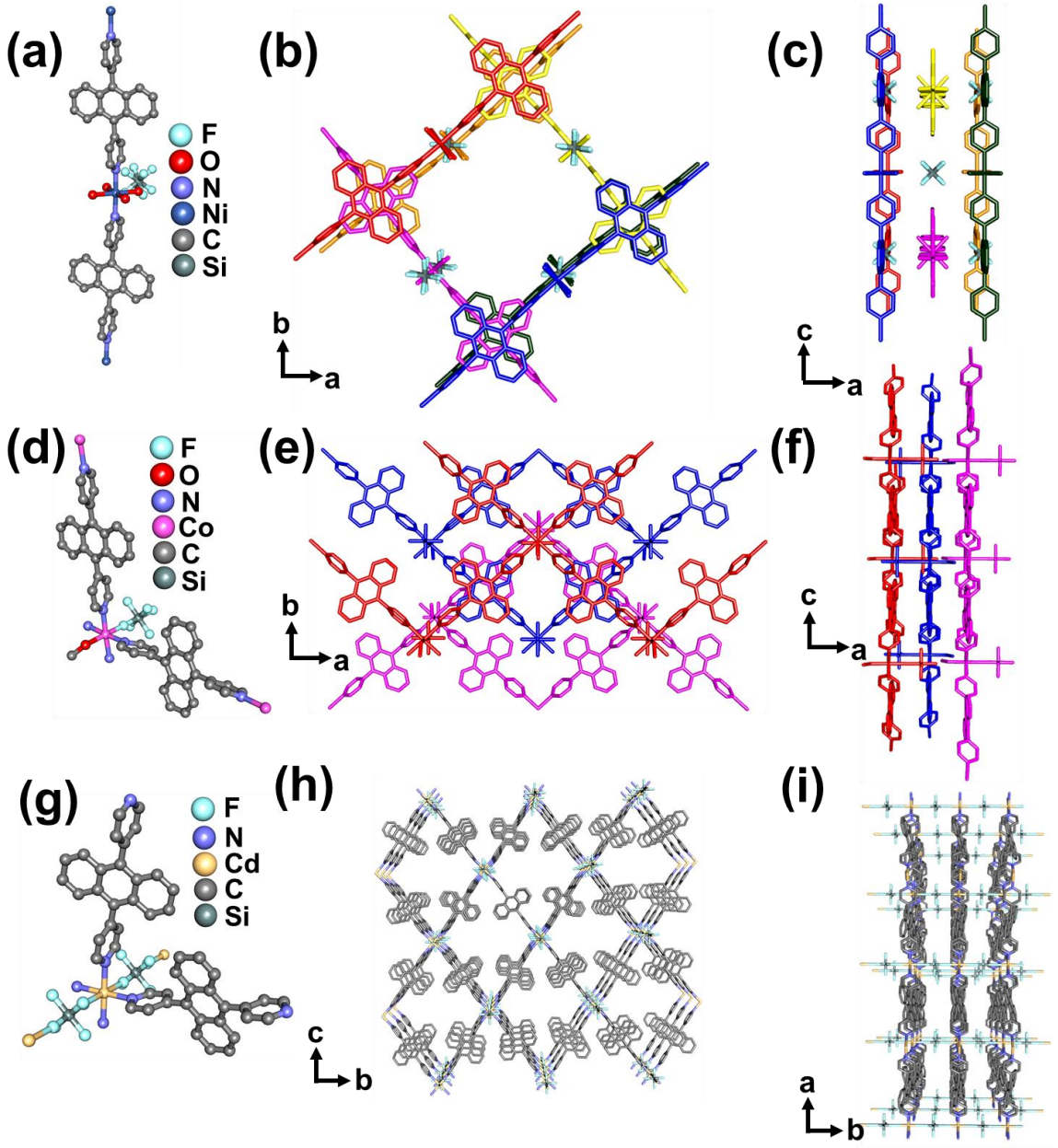

Figure 2-3. Crystal structures of $[Ni(dpa)(H_2O)_4]\cdot SiF_6$: coordination environment around the nickel(II) center (a), Packing structure viewed along [001] (b) and [110] (c). Crystal structures of $[Co(dpa)_2(CH_3OH)(SiF_6)]$: coordination environment around the cobalt(II) center (d), Packing structure viewed along [001] (e) and [110] (f). Crystal structures of $[Cd(dpa)_2(SiF_6)]$: coordination environment around the cadmium(II) center (a), Packing structure viewed along [011] (b) and [110] (c).

Table 2-1. Crystallographic parameters of those compounds

	$[Zn(dpa)_2(SiF_6)]$	$[Cd(dpa)_2(SiF_6)]$	$[Co(dpa)_2(CH_3OH)(SiF_6)]$
Crystal System	Monoclinic	Monoclinic	Orthorhombic
Space Group	*P 2₁/c*	*C 2/m*	*C m c a*
a (Å)	7.6219(2)	19.1372(7)	23.8107(12)
b (Å)	11.3557(4)	25.5614(7)	20.7193(9)
c (Å)	19.3988(5)	7.8538(2)	18.1666(9)
α (°)	90 °	90 °	90 °
β (°)	91.628(2) °	91.428(3) °	90 °
γ (°)	90 °	90 °	90 °
V ($Å^3$)	3603.90(16)	3840.7(2)	8962.3(7)
Z	2	2	8
Diffractometer	CCD	CCD	CCD
μ(mm^{-1})	0.396	0.336	0.475
Radiation type	Mo *Kα*	Mo *Kα*	Mo *Kα*
Radiation wavelength	0.71073	0.71073	0.71073
F(000)	892.0	928.0	3688
Goodness of fit	1.166	1.167	1.039
Temperature (K)	93K	93K	93K
Reflections collected	28412	23825	29819
Independent	8472	5033	5882
R_1 ($I > 2.00\sigma(I)$)[a]	5.47 %	4.28 %	4.21 %
wR_2 ($I > 2.00\sigma(I)$)[b]	20.03 %	13.50 %	12.43 %

	$[Ni(dpa)(H_2O)_4]\cdot SiF_6$	$[Zn(epo)_2(SiF_6)]$	$[Cd(epo)_2(SiF_6)]$
Crystal System	Tetragonal	Tetragonal	Orthorhombic
Space Group	*P 4₂/m n m*	*I 4 c m*	*P n n a*
a (Å)	21.9283(8)	21.8242(5)	24.2602(8)
b (Å)	21.9283(8)	21.8242(5)	15.2698(14)
c (Å)	9.7013(7)	15.0349(6)	19.8413(7)
α (°)	90 °	90 °	90 °
β (°)	90 °	90 °	90 °
γ (°)	90 °	90 °	90 °
V ($Å^3$)	4664.9(5)	7161.1(4)	7350.2(8)
Z	4	4	4
Diffractometer	CCD	CCD	CCD
μ(mm^{-1})	0.484	0.405	0.357
Radiation type	Mo *Kα*	Mo *Kα*	Mo *Kα*
Radiation wavelength	0.71073	0.71073	0.71073
F(000)	1240.0	1912.0	1984.0

Goodness of fit	1.074	1.071	1.073
Temperature (K)	93K	93K	93K
Reflections collected	33866	28398	85670
Independent	3423	4700	9786
R_1 ($I > 2.00\sigma(I)$)[a]	11.89 %	5.20 %	12.94 %
wR_2 ($I > 2.00\sigma(I)$)[b]	31.09 %	16.54 %	37.67 %

	$[Zn(dpa)(H_2O)_2(CH_3OH)_2]\cdot SiF_6$
Crystal System	Tetragonal
Space Group	*P* 4_3 *2 2*
a (Å)	15.6536(5)
b (Å)	15.6536(5)
c (Å)	19.2658 (11)
α (°)	90 °
β (°)	90 °
γ (°)	90 °
V ($Å^3$)	4720.8(4)
Z	4
Diffractometer	CCD
$\mu(mm^{-1})$	0.612
Radiation type	Mo $K\alpha$
Radiation wavelength	0.71073
F(000)	1528.0
Goodness of fit	1.263
Temperature (K)	93K
Reflections collected	34495
Independent	4757
R_1 ($I > 2.00\sigma(I)$)[a]	11.93 %
wR_2 ($I > 2.00\sigma(I)$)[b]	32.47 %

[a]$R_1 = \sum||F_o|-|F_c||/\sum|F_o|$, [b]$wR_2 = [\sum w|F_o^2-F_c^2|^2/\sum w(F_o^2)^2]^{1/2}$

Stability of MOFs based dpa ligand

In order to characterize the crystallinity and stabilities of these MOF compounds, the PXRD of all these compounds in their different states (simulated, as-synthesized and degassed) were measured and compared. All of the as-synthesized samples were exchanged with ethanol for 3 days and heated at 100 ℃ for degassing. As shown in **Figure 2-4**, the PXRD patterns of EtOH exchanged and degassed of $[Ni(dpa)(H_2O)_4]\cdot SiF_6$ $[Cd(dpa)_2(SiF_6)]$ are completely inconsistent with the simulated. The result indicates the

poor stability of them. PXRD results show that $[Co(dpa)_2(CH_3OH)(SiF_6)]$ can maintain its structures after degassing, indicating this 2D layer structure is quite stable. However, no matter of $[Cd(dpa)_2(SiF_6)]$ or $[Ni(dpa)(H_2O)_4]\cdot SiF_6$, the PXRD patterns are well match with $[Co(dpa)_2(CH_3OH)(SiF_6)]$ after the solvent exchange (**Figure 2-5** left). In addition, the TG curves (**Figure 2-6**) of these compounds after the solvent exchange are similar. So we speculate that the 1D $[Ni(dpa)(H_2O)_4]\cdot SiF_6$ and 3D $[Cd(dpa)_2(SiF_6)]$ change to 2D layer structures after solvent exchange. As for $[Zn(dpa)_2(SiF_6)]$, it can maintain its structure after ethanol exchanging and degassing at 100 ℃ from the PXRD results (**Figure 2-5** (b)).

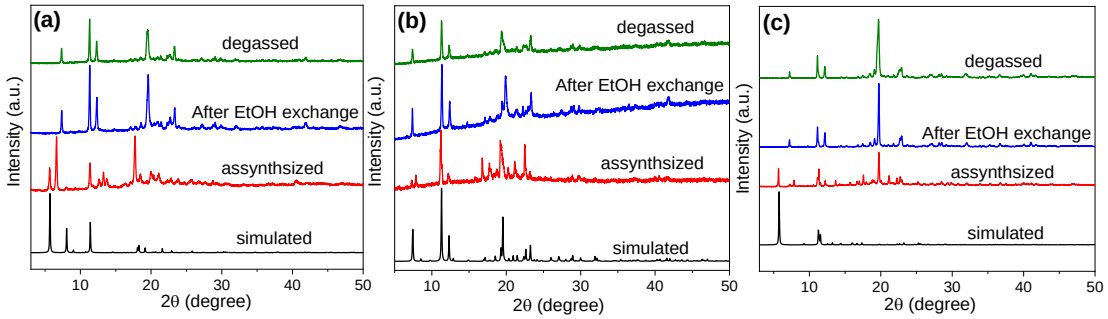

Figure 2-4. PXRD patterns for simulated, assynthesized, after EtOH exchange and degassed samples of $[Co(dpa)_2(CH_3OH)(SiF_6)]$, $[Cd(dpa)_2(SiF_6)_2]$ and $[Ni(dpa)(H_2O)_4]\cdot SiF_6$.

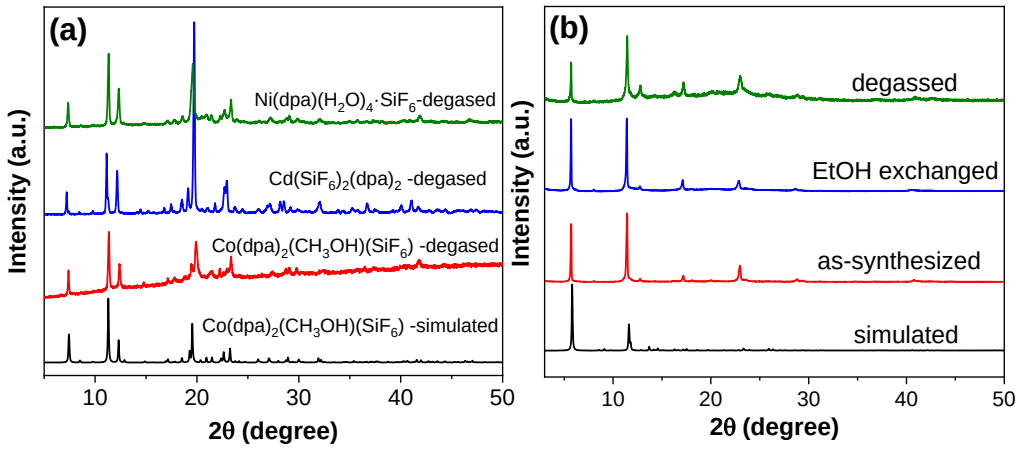

Figure 2-5. (a): PXRD patterns for simulated of $[Co(dpa)_2(CH_3OH)(SiF_6)]$ and degassed samples of $[Co(dpa)_2(CH_3OH)(SiF_6)]$, $[Cd(dpa)_2(SiF_6)_2]$ and $[Ni(dpa)(H_2O)_4]\cdot SiF_6$. (b):

PXRD patterns for simulated, assynthesized and degassed samples of $[Zn(dpa)_2(SiF_6)_2]$

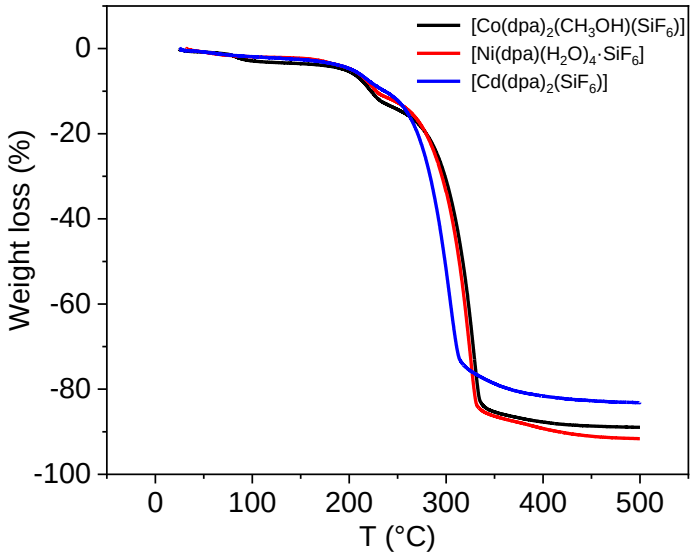

Figure 2-6. Thermal gravimetric analysis (TGA) curve of $[Co(dpa)_2(CH_3OH)(SiF_6)]$, $[Cd(dpa)_2(SiF_6)_2]$ and $[Ni(dpa)(H_2O)_4]\cdot SiF_6$.

Structure of MOFs based epo ligand

Compounds $[Zn(epo)_2(SiF_6)]$ and $[Cd(epo)_2(SiF_6)]$ were directly synthesized using Cd^{2+}/Zn^{2+} with epo ligand. They are feature a SIFSIX MOF structure (**Figure 2-7**), in both of the two structures, epo bridged zinc(II) ions to form two-dimensional square lattices, which were further pillared by SiF_6^{2-} anions to construct a 3D structure. Compounds $[Zn(epo)_2(SiF_6)]$ has a tetragonal space group *I 4 c m*. While zinc and cadmium are the same groups in the periodic table, but interestingly, compounds $[Cd(epo)_2(SiF_6)]$ has rhombus lattices with an orthorhombic space group *P n n a*. The coordination of singlet oxygen and anthracene is clearly visible in both of the two compounds, all of the coordinated oxygens are toward to the lamellar spacing.

On the contrary to compound $[Cd(dpa)_2(SiF_6)]$, compound $[Cd(epo)_2(SiF_6)]$ is stable after solvent exchange and degas which evident from their PXRD patterns ((**Figure 2-8**). Compound $[Zn(epo)_2(SiF_6)]$ also shows good stability after solvent exchange and degas

(**Figure 2-8**).

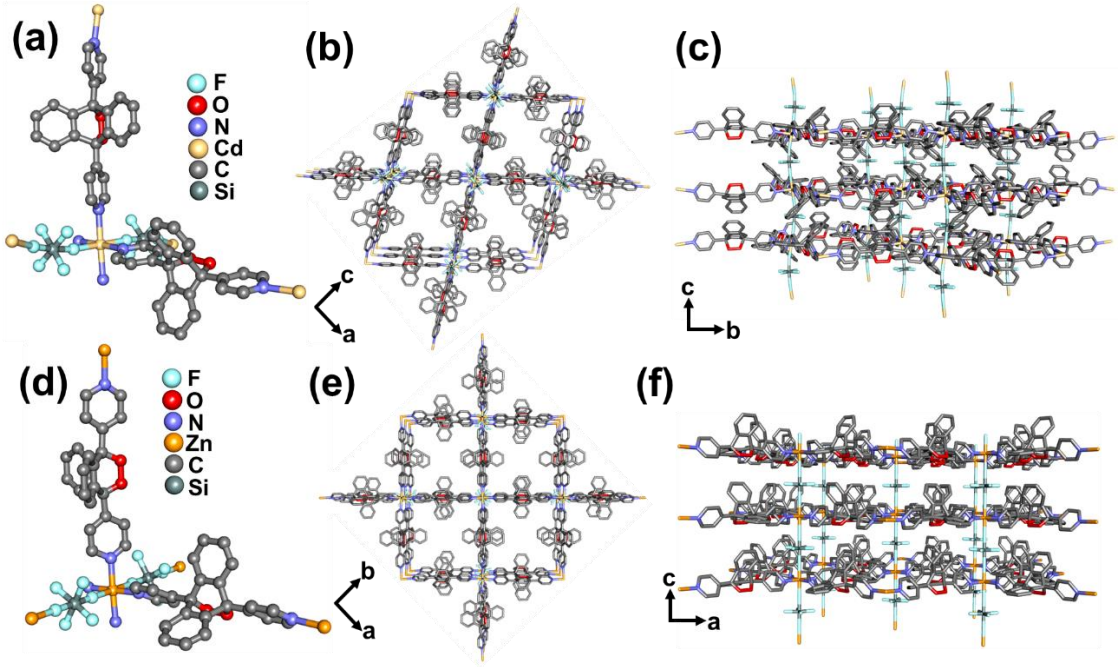

Figure 2-7. Crystal structures of [Cd(epo)$_2$(SiF$_6$)]: coordination environment around the cadmium(II) center (a), Packing structure viewed along [011] (b) and [110] (c). Crystal structures of [Zn(epo)$_2$(SiF$_6$)]: coordination environment around the zinc(II) center (d), Packing structure viewed along [011] (e) and [110] (f).

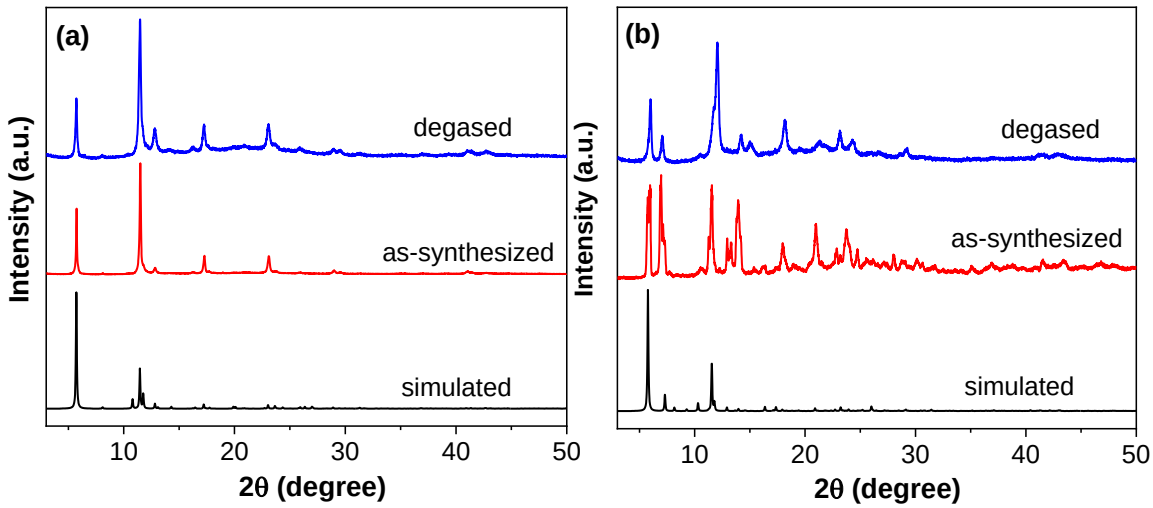

Figure 2-8. Figure 4 PXRD patterns for simulated, assynthesized and degassed samples of [Zn(epo)$_2$(SiF$_6$)] (a) and [Cd(epo)$_2$(SiF$_6$)] (b).

Oxygen capture property in air under UV irradiation

Dpa ligand exhibits photosensitizing and oxygen trapping abilities in liquid solutions, it can transfer epo under oxygen and UV-light (380 nm) in DMF or acetone solution. However, this reaction cannot occur in the solid state. **Figure 2-9** shows the ^{1}H NMR spectra before UV irradiation and after UV irradiation of dpa ligand under the condition of solid phase exposure to air. The unchanged spectra indicate that this reaction did not happen.

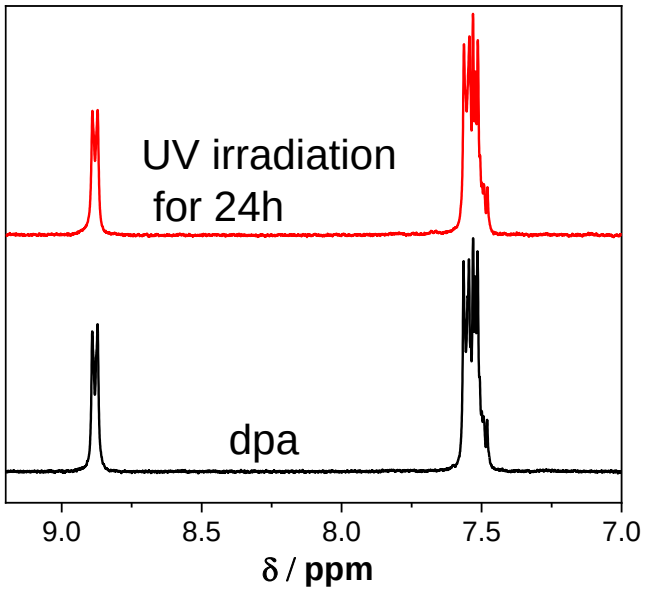

Figure 2-9. ^{1}H NMR spectrum of dpa after 24 hours photo irradiation.

The photoreaction properties of the [Zn(dpa)$_2$(SiF$_6$)] also were investigated in solid phase in an open air atmosphere. **Figure 2-10** shows the time-course change of ^{1}H NMR spectra dissolved in DMSO-d^6 after photoirradiation for [Zn(dpa)$_2$(SiF$_6$)]. The peaks in NMR spectrum assigned to dpa decreased with increasing photoirradiation time whereas those of epo increased. It is noteworthy that the conversion ratio after photoirradiation was estimated to be ≈ 55% after 8 hours. The ratio of epo is continues to increase with longer irradiation time. However, new peaks in NMR spectra that do not correspond to either dpa or epo, are also started to appear. The appearance of these new peaks in NMR

spectra are caused by the decomposition of epo and it appears that the long-time photoirradiation can promote rearrangement and decomposition of epo linkers resulting in structural damage, [18] that have been confirmed by PXRD. After 12h UV irradiation, the PXRD spectra intensity of $[Zn(dpa)_2(SiF_6)]$ was decreased and some new peaks appeared. The time dependent PXRD measurement study of $[Zn(dpa)_2(SiF_6)]$ compound during photoirradiation revealed that the PXRD patterns remained unchanged up to 8h of photoirradiation (**Figure 2-11**). In order to explore if it is because of the porous structure of $[Zn(dpa)_2(SiF_6)]$ that it can react with O_2, we also carried out the photoirradiation under exposure to air using $[Cd(dpa)_2(SiF_6)]$, $[Ni(dpa)_2(SiF_6)]$ and $[Co(dpa)_2(SiF_6)]$ after degassing. **Figure 2-12** shows all of these three compounds cannot react with O_2 after photoirradiation for 24h. The reason can be attributed to their non-porous structure, where oxygen molecules cannot enter the interior of the structure to participate in the photoreaction. **Figure 2-13** shows the packing structure of $[Co(dpa)_2(CH_3OH)(SiF_6)]$ and dpa ligands, from which we can see that they are densely packed into a non-porous structure. These results indicate the essential of the porous structure for the reaction with O_2 in solid phase. The amount of trapped oxygen is about 40 mg O_2 per gram $[Zn(dpa)_2(SiF_6)]$ at room temperature and 1 bar calculated from the ^1H NMR data analysis.

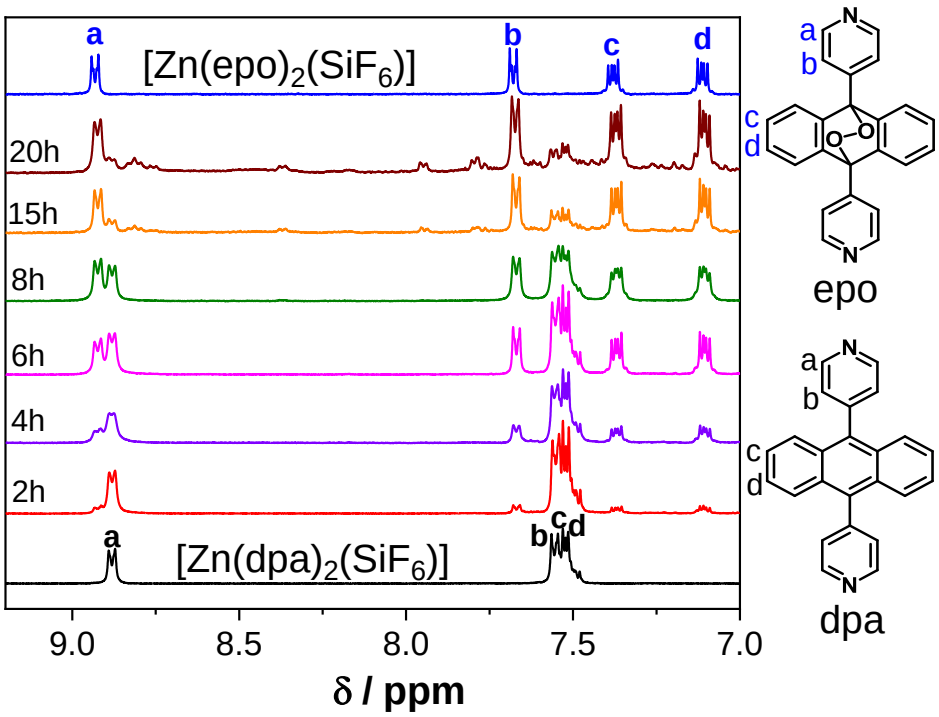

Figure 2-10. Time-course change of ^{1}H NMR spectra of $[Zn(dpa)_2(SiF_6)]$ digested in Chloroform-d after photoirradiation.

Because the simulated PXRD of the $[Zn(dpa)_2(SiF_6)]$ and $[Zn(epo)_2(SiF_6)]$ are similar, it is difficult to determine the structural changes between the two compounds by PXRD. So the solid state luminescent properties of the $[Zn(dpa)_2(SiF_6)]$, $[Zn(dpa)_2(SiF_6)]$ after UV irradiation for 8h, and $[Zn(epo)_2(SiF_6)]$ were investigated in solid phase. As shown in **Figure 2-14**, the peaks at 330-430 nm characterize the anthracene moiety. The intensity of $[Zn(dpa)_2(SiF_6)]$ is much higher than $[Zn(epo)_2(SiF_6)]$. After UV irradiation, the peaks between λ_{em} = 320-430 nm were decreased, while the emission peak around 260 nm attributed to pyridine remains unchanged, suggesting that $[Zn(dpa)_2(SiF_6)]$ can be converted to $[Zn(epo)_2(SiF_6)]$ by reaction with oxygen under UV irradiation.

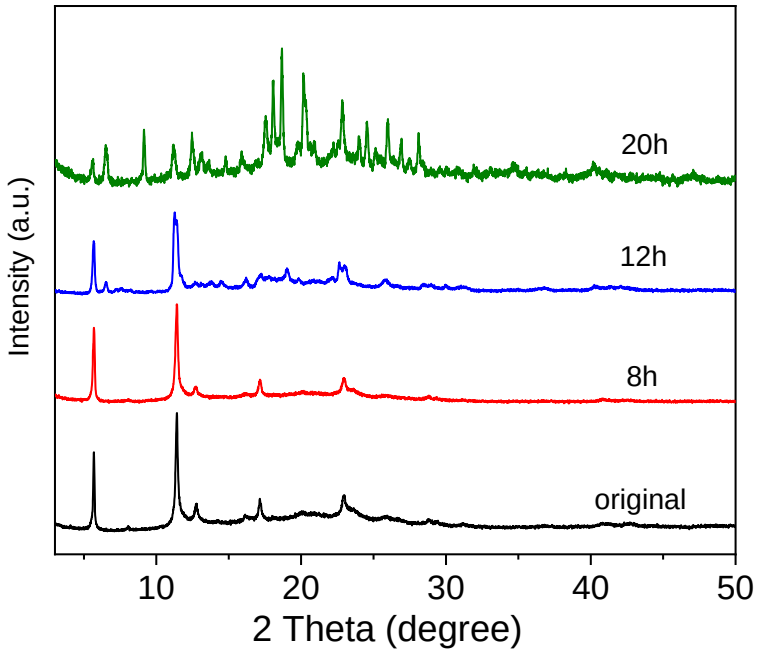

Figure 2-11. PXRD patterns of $[Zn(dpa)_2(SiF_6)_2]$ after different photo irradiation time.

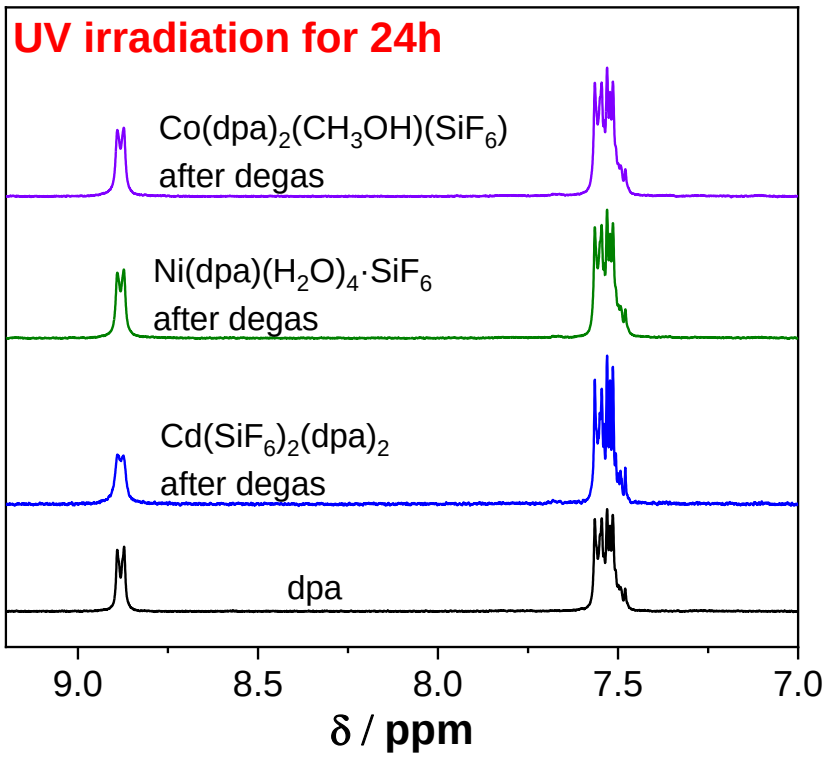

Figure 2-12. ^1H NMR spectrum of $[Co(dpa)_2(CH_3OH)(SiF_6)]$, $[Cd(dpa)_2(SiF_6)_2]$ and $[Ni(dpa)(H_2O)_4]\cdot SiF_6$ after 24 hours photo irradiation.

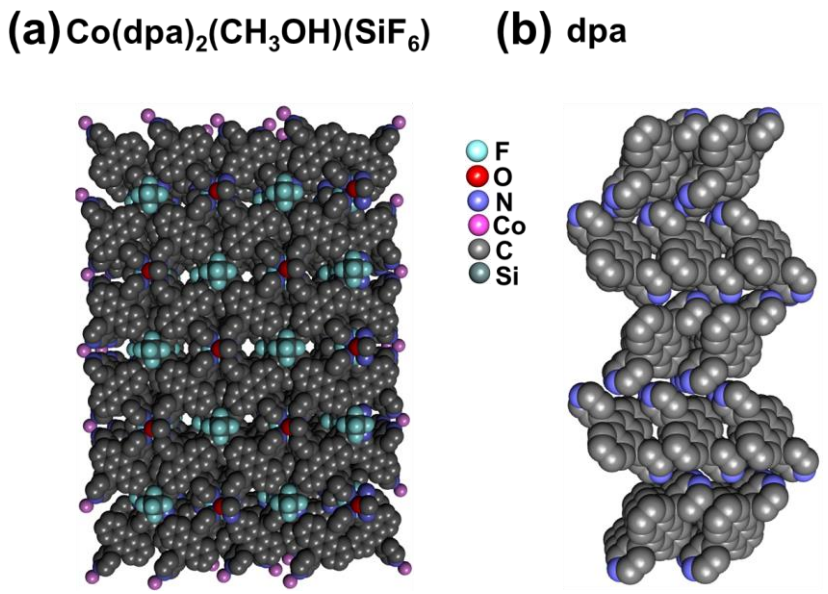

Figure 2-13. Packing structure of [Co(dpa)$_2$(SiF$_6$)] and dpa ligand using spacefill model.

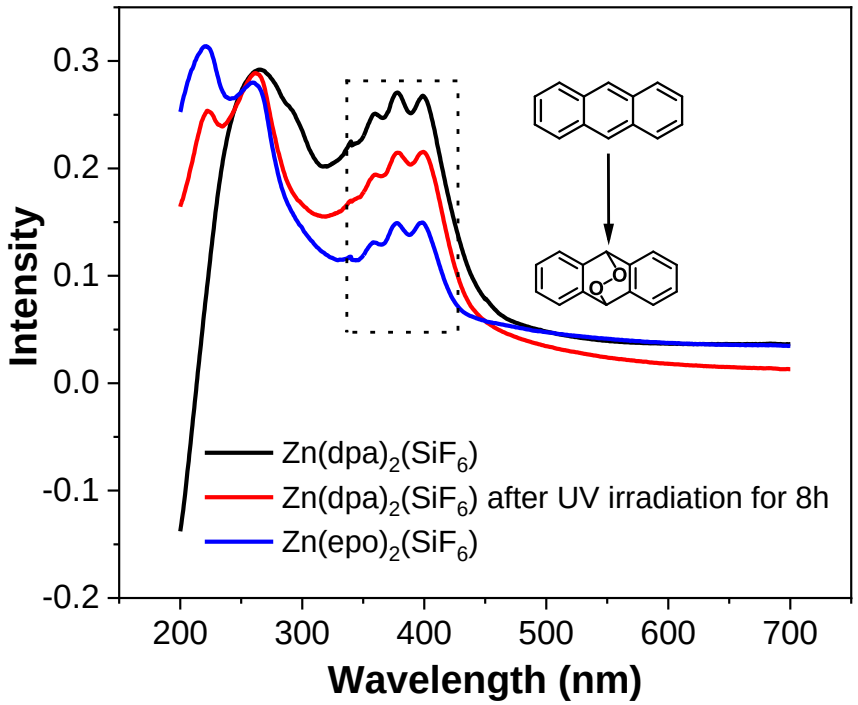

Figure 2-14. Solid-state UV-Vis absorption spectra.

Oxygen releasing property after heating

Both of the compounds [Zn(epo)$_2$(SiF$_6$)] and [Cd(epo)$_2$(SiF$_6$)] have endoperoxide in

the framework. To confirm the release of oxygen and the recovery of original $[Zn(dpa)_2(SiF_6)]$ from $[Zn(epo)_2(SiF_6)]$, we measure the ^1H NMR spectra after heating the samples of the $[Zn(epo)_2(SiF_6)]$ for 24h at different temperatures. The results show that 90% of the endoperoxide form of anthracene can be maintained in the framework when the temperature of the samples was maintained at 80 °C, indicating the good stabilities of endoperoxide form of anthracene in $[Zn(epo)_2(SiF_6)]$. The coordinated oxygen is released upon complete decomposition of endoperoxide form of anthracene when sample was heated at 140 °C for 24h. ^1H NMR spectra about the release of oxygen at different temperatures demonstrated the coordinated oxygen retention at different temperatures heating for 24 h. Moreover, the release of O_2 molecules from $[Zn(epo)_2(SiF_6)]$ and $[Cd(epo)_2(SiF_6)]$ were also observed in the form weight loss in thermosgravimetric analyses (**Figure 2-16**). The TGA data of both $[Zn(epo)_2(SiF_6)]$ and $[Cd(epo)_2(SiF_6)]$ show a significant drop around 140 °C, which correspond to the results obtained from the ^1H NMR spectra. These results indicate that O_2 is rapidly released from the frameworks when the temperature exceeds 130 °C. Similarly, we measured the ^1H NMR of $[Zn(dpa)_2(SiF_6)]$, which was first UV irradiate for 8 hours and then heated to 140 °C for 24 h. The result in **Figure 2-17** shows that it also can release all the O_2 molecules that are trapped in the form of endoperoxide.

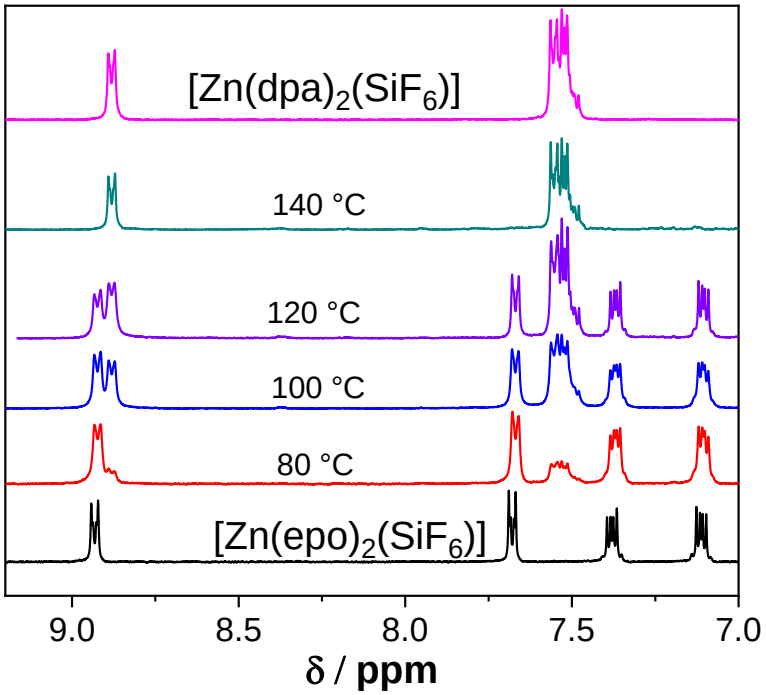

Figure 2-15. Time-course change of ^{1}H NMR spectra of [Zn(dpa)$_2$(SiF$_6$)] digested in Chloroform-d after photoirradiation.

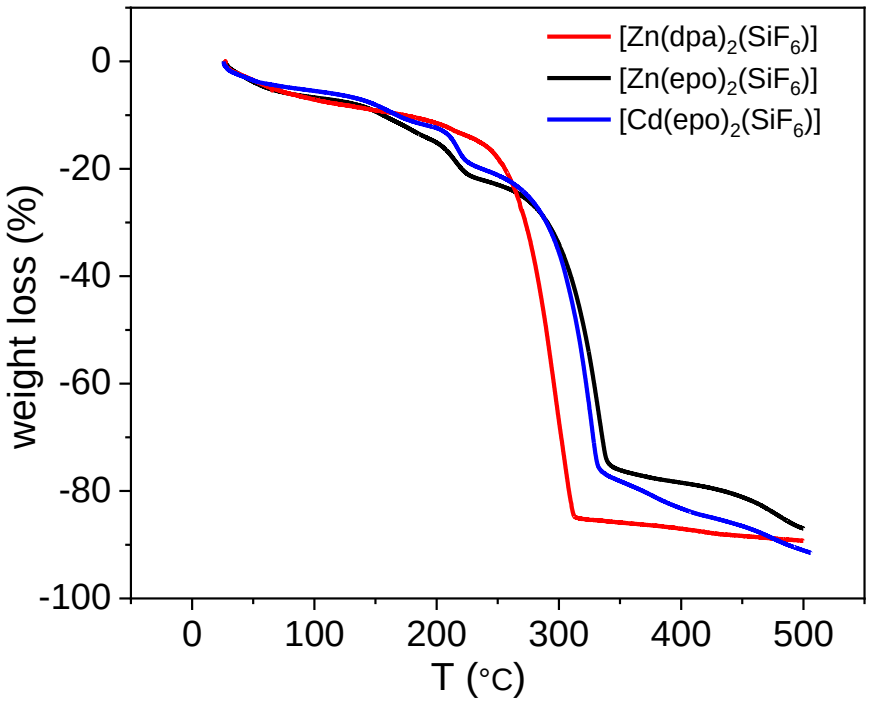

Figure 2-16. Thermal gravimetric analysis (TGA) curve of [Zn(dpa)$_2$(SiF$_6$)$_2$], [Zn(epo)$_2$(SiF$_6$)$_2$] and [Cd(dpa)$_2$(SiF$_6$)$_2$].

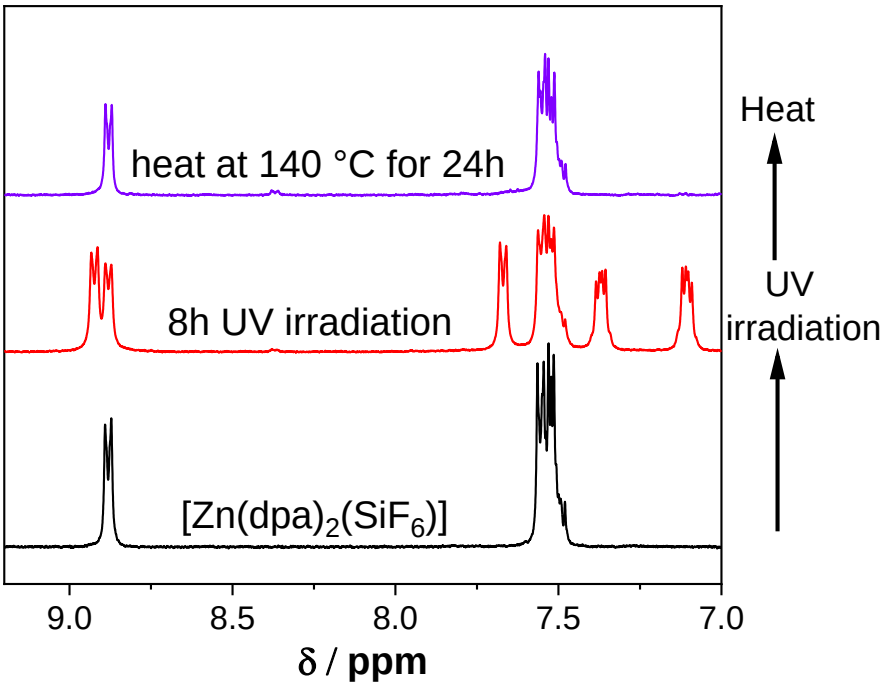

Figure 2-17. ^{1}H NMR spectrum of [Zn(dpa)$_2$(SiF$_6$)] which first UV irradiate for 8 hours and then heated to 140 °C for 24h.

2-4. Conclusions

In summary, we synthesized a MOF ([Zn(dpa)$_2$(SiF$_6$)]) with the ability to trap the O_2 from air and release oxygen molecules after heating. It is very surprising that MOFs can capture oxygen directly from the air. We also demonstrated that porous structure is necessary for photoreaction with singlet oxygen in gas phase. We believe that this highly selective oxygen-capturing material will provide a new method for separating oxygen from the air.

2-5. References

1 H. Li, M. Eddaoudi, M. O'Keeffe, O.M. Yaghi, *Nature*, 1999, **402**, 276-279.

2 D. Alezi, Y. Belmabkhout, M. Suyetin, P. M. Bhatt, Ł. J. Weseliński, V. Solovyeva, K. Adil, I. Spanopoulos, P. N. Trikalitis, A. H Emwas, M. Eddaoudi, *J. Am. Chem. Soc.*, 2015, **137**, 13308-13318.

3 R. Matsuda, R. Kitaura, S. Kitagawa, Y. Kubota, T. C. Kobayashi, S. Horike, M.

Takata, *J. Am. Chem. Soc.*, 2004, **126**, 14063 – 14070.

4 P. García-García, M. Müller, A Corma, *Chem. Sci.*, 2014, 5, 2979-3007.

5 J. Liu, L. Chen, H. Cui, J. Zhang, L. Zhang, C. Y. Su, *Chem. Soc. Rev.*, 2014, **43**, 6011-6061.

6 C. McDonagh, C. Kolle, A.K. McEvoy, D.L. Dowling, A.A.Cafolla, S.J.Cullen, B.D.MacCraith, *Sensor Actuat B-chem.*, 2001, **74**, 124-130.

7 F. Sjöberg, M. Singer. *J. Intern. Med.*, 2013, **274**, 505-528.

8 D. Hirsch, J. Williams, H. Beeson, *J. Test. Eval.*, 2008, **36**, 69-72.

9 L. A. Mitchell, T. M. Tovar, M. D. LeVan, *Carbon*, 2014, **74**, 120-26.

10 Y. Wang, B. Helvensteijn, N. Nizamidin, A. M. Erion, L. A.Steiner, L. M. Mulloth, B. Luna, M. D. LeVan, *Langmuir*, 2011, **27**, 10648 – 10656.

11 D. Alezi, Y. Belmabkhout, M Suyetin, P. M. Bhatt, Ł. J. Weseliński, V. Solovyeva, K. Adil, I. Spanopoulos, P. N. Trikalitis, A.H. Emwas, M. Eddaoudi, *J. Am. Chem. Soc.*, 2015, **137**, 13308-13318.

12 J.B. DeCoste, M.H Weston, P.E Fuller, T.M. Tovar, G.W. Peterson M.D. LeVan O. K. Farha,, *Angew. Chem. Int. Ed.*, 2014, **126**, 14316-14319.

13 Y Tang, X. Wang, Y. Wen, X. Zhou, Z. Li, *Ind. Eng. Chem. Res.*, 2020, **59**, 6219-6225.

14 S. Subramanian, M. J. Zaworotko, *Angew. Chem. Int. Ed.*, 1995, **34**, 2127-2129.

15 S. Noro, R. Kitaura, M. Kondo, S. Kitagawa, T. Ishii, H. Matsuzaka, M. Yamashita, *J. Am.Chem. Soc.*, 2002, **124**, 2568-2583.

16 M. Fujimura, S. Kusaka, A. Masuda, A. Hori, Y. Hijikata, J. Pirillo, Y. Ma, R. Matsuda, *Small*, 2020, **17**, 2004351.

17 W. Fudickar, T. Linker, *J. Org. Chem.*, **2017**, 82, 9258-9262.

18 J. M Aubry, C Pierlot, J Rigaudy, S. Reinhard, Acc. *Chem. Res.*, 2003, **36**, 668-675.

Chapter 3

Modulation of the coordination networks and crystallinity of SIFSIX pillared metal-organic frameworks

3-1. Introduction

Metal-organic frameworks (MOFs), also known as porous coordination polymers (PCPs) are some of the most rapid growth porous materials in gas storage, [1,2] sensor, [3,4] and proton conduction. [5,6] It is constructed from the blend of organic linkers, resulting in a three-dimensional (3D) skeletal structure embedded with metal-containing node. The SIFSIX series are one kind of MOFs, which are recently emerged as promising porous materials exhibiting high CO_2, CH_4, and hydrocarbons storage duo to the strong electrostatic interactions from the inorganic anions that the pore walls. [7-9] Although the first SIFSIX material (SIFSIX-3-Zn) was reported more than 20 years ago, [10] SIFSIX series grow rapidly in the last decades and they exhibit excellent gas storage and separation performances. [11,12] These MOFs are synthesized by combining M^{2+} ions (e.g., Cu^{2+}, Zn^{2+}, Ni^{2+}, Co^{2+}, Fe^{2+}) with organic linkers to form two dimensional grids, then these grids are pillared with SiF_6^{2-} anions to form a porous and regular three-dimensional framework. So far, SIFSIX-3-M ([M(4,4'-bipyridine)$_2$(SiF_6)]) have been synthesized from different metals (SIFSIX-3-Cu, Zn, Ni, Co, Fe), among them, both SIFSIX-3-Cu and SIFSIX-3-Zn exhibit excellent performance for acetylene capture from ethylene [13,14]. Thallapally et al. [15] reported that SIFSIX-3-Co can selectively remove CO_2 from flue gas. SIFSIX-3-Ni not only shows exceptional CO_2 capture and H_2S tolerance but also can maintain its stability in both CO_2-humidity (with up to 80% RH) and CO_2-air environment.[16] Besides, SIFSIX-3-Ni and SIFSIX-3-Fe exhibit high isosteric heat of adsorption for Xe and preferential adsorption of Xe over Kr [17]. Thus, the development of MOF family based SIFSIX platform can expand the variety of potential applications. Furthermore, longer organic linker often results in interpenetrated structure and low stability, restricting their gas storage and separation applications. [18-20] Benefit from not exceptionally long linkers and relatively larger pore size than SIFSIX-3-M, 4,4'-

bipyridine and 1,2-bis(4-pyridyl)ethane can be a choice to construct SIFSIX series for gas storage. Currently, although some research groups reported the two-dimensional(2D) structure using Ni^{2+}, Co^{2+}, Zn^{2+} and 4,4'-bipyridine and 1,2-bis(4-pyridyl)ethane SiF_6^{2-} dianions didn't coordinate with metal but coordinated with water through hydrogen bonds in these structures [21]. These non-porous 2D structures greatly limit their application potential. Because of the huge potential application value of SIFSIX MOFs of different metals, we pursue synthesizing three-dimensional SIFSIX MOFs using different metals and exploring their gas storage and separation properties.

In this work, we synthesized single crystals of SIFSIX-1-Ni, Co, Cd and SIFSIX-7-Cd, Ni, Zn at room temperature using slow diffusion routes in a glass tube except that SIFSIX-1-Cd and SIFSIX-1-Zn. SIFSIX-1-Cd and SIFSIX-1-Zn were synthesized by directly mixing both of the ligand solution in N-methylpyrrolidone(NMP) and metal salt solution in methanol. All of these MOFs have 3D porous structures. In particular, SIFSIX-1-Ni, SIFSIX-1-Co, and SIFSIX-7-Ni can maintain their structure even after the removal of the solvents. Sorption properties of all these frameworks using CO_2, N_2, C_2H_2, C_2H_4 and C_2H_6 gases as well as the potential adsorption selectivity for CO_2/N_2 and C_2H_2/C_2H_4 gas mixtures were further studied to investigate the gas adsorption and separation performance.

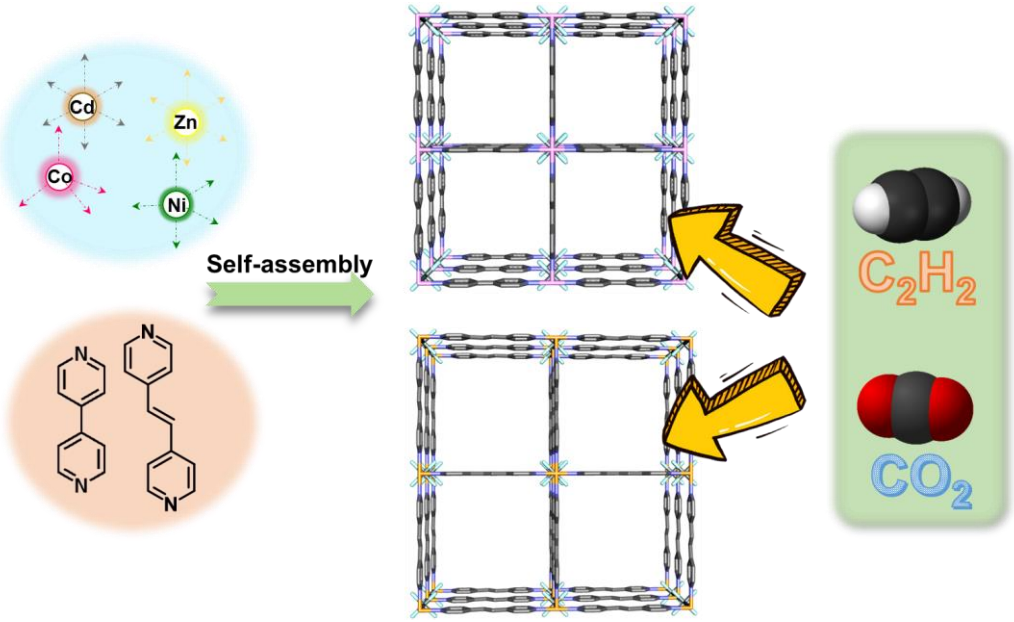

Graphic abstract

3-2. Experimental

Chemicals

Zinc hexafluorosilicate (Aldrich, 99%). Nickel hexafluorosilicate (Aldrich, 99%). Methanol (Wako, 99.8%). 1-Methyl-2-pyrrolidinone (TCI, 99%). 4,4′-bipyridine (TCI, 98%), 1,2-bis(4-pyridyl)ethane (TCI, 98%), $Cd(OH)_2$ (Wako, 95%), $Co(OH)_2$ (Wako, 56.0~64.0%), H_2SiF_6 (Wako, 40.0~45.0%), Cadmium hexafluorosilicate was prepared through neutralizing fluorosilicic acid with Cadmium oxide and then filtering, evaporating, crystallization, centrifugal separation, and drying. Cobalt hexafluorosilicate was obtained using the same method.

Synthesis of single crystals

SIFSIX-1-Ni: Slow diffusion of a methanol solution of nickel hexafluorosilicate (0.005 mM) into a NMP solution of 4,4′-bipyridine (0.01 mM). Light blue blocks were obtained after 10 d.

SIFSIX-1-Co: Slow diffusion of a methanol solution of cobalt hexafluorosilicate (0.01 mM) into a NMP solution of 4,4′-bipyridine (0.01 mM). Pink blocks were obtained after 3 d.

SIFSIX-1-Cd: Slow diffusion of a methanol solution of cadmium hexafluorosilicate (0.02 mM) into a NMP solution of 4,4′-bipyridine (0.02 mM). Colourless blocks were obtained after 1d.

SIFSIX-7-Ni: Slow diffusion of a methanol solution of Nickel hexafluorosilicate (0.005 mM) into a NMP solution of 1,2-bis(4-pyridyl)ethane (0.01 mM). Light blue blocks were obtained after 10 d.

SIFSIX-7-Zn: Slow diffusion of a methanol solution of zinc hexafluorosilicate (0.02 mM) into a NMP solution of 1,2-bis(4-pyridyl)ethane (0.02 mM). Colourless blocks were obtained after 1d.

SIFSIX-7-Cd: Slow diffusion of a methanol solution of cadmium hexafluorosilicate (0.02 mM) into a NMP solution of 1,2-bis(4-pyridyl)ethane (0.02 mM). Colourless blocks were obtained after 1 d.

Characterization

X-ray diffraction (XRD) patterns of the MOF membranes and MOF powders were measured from a Rigaku X-ray diffractometer with Cu *Kα* radiation. Single crystal X-ray diffraction data were collected on a RIGAKU XtaLab P200 CCD system with VariMax Mo Optic with Mo*K*α radiation (λ = 0.71073 Å) and a confocal monochromator, with the constant temperature of 93 K by flowing low-temperature nitrogen gas. The structure was solved by direct methods and refined by full-matrix least-squares cycles using SHELXs1. All non-hydrogen atoms were refined with anisotropic thermal parameters. Hydrogen atoms attached to carbon atoms were located at geometrically calculated positions and refined with isotropic thermal parameters Gas adsorption experiments were carried out using a microtrac-BEL BELSorp-max automated gas adsorption analyzer equipped with a cryostatic temperature controller.

Calculation of Isosteric Heat of Gas Adsorption (Q_{st})

The isosteric heat of adsorption (Q_{st}) for the C_2H_2, C_2H_4, and C_2H_6 adsorption of SIFSIX-1-Ni and SIFSIX-7-Ni are calculated via virial method. The adsorption isotherms used for the calculations are the ones measured at 273 K and 298 K (**Figure 3-6, 3-7, 3-**

10, and 3-11). At first, the adsorption data are fitted using the virial-type equation:

$$InP = InN + 1/T \sum_{i=0}^{m} a_i N^i + \sum_{j=0}^{n} b_j N^j$$

Where, P is the pressure expressed in Torr, N is the amount adsorbed in mmol g^{-1}, T is the temperature in K, a_i and b_i are virial coefficients, and m, n represent the number of coefficients required to adequately describe the isotherms. Next, the Clausius-Clapeyron equation was used to calculate the isosteric heat of gas adsorption based the the values of the virial coefficients a_0. The equation was shown below:

$$Q_{st} = -R \sum_{i=0}^{m} a_i N^i$$

Here, Q_{st} is the coverage-dependent isosteric heat of adsorption and R is the universal gas constant.

All of the fitted parameter values are summarized in **Figure 3-13 and Figure 3-14.**

Prediction of the Gases Adsorption Selectivity by IAST

IAST (ideal adsorption solution theory) was used to estimate the composition of the adsorbed phase from experimental single-component isotherm data and predict the selectivity of the binary mixture C_2H_2/C_2H_4 and CO_2/N_2. Dual-site Langmuir-Freundlich equation (DSLF) was used to perform the integrations required by IAST:

$$q = \frac{q_{m,1} b_1 P^{n_1}}{1 + b_1 P^{n_1}} + \frac{q_{m,2} b_2 P^{n_2}}{1 + b_2 P^{n_2}}$$

Here, P is the pressure of the bulk gas at equilibrium with the adsorbed phase (Pa), q is the adsorbed amount of adsorbent (mol kg^{-1}), $q_{m,1}$ and $q_{m,2}$ are the saturation capacities of sites 1 and 2 (mol kg^{-1}). b_1 and b_2 are the affinity coefficients of sites 1 and 2 (Pa^{-1}), and n_1 and n_2 represent the deviations from an ideal homogeneous surface.

The fitted parameter values are summarized in **Table 3-3 to Table 3-10.**

IAST binary-gas adsorption selectivities for a binary mixture of components A and B were defined as:

$$S_{A/B} = \frac{q_A / P_A}{q_B / P_B}$$

where q_A, q_B are the molar fraction of A and B in the adsorbed phase, respectively, P_A, P_B are molar fraction of A and B in the bulk phase, respectively.

3-3. Results and discussion

Structure of MOFs based dpa ligand

All of the 6 MOFs were obtained using NMP/MeOH solution. The previously reported 2D structures of different frameworks constructed using metal ions (Ni^{2+}, Co^{2+}, Zn^{2+}) and organic linkers (4,4'-bipyridine and 1,2-bis(4-pyridyl)ethane) reveal that metal ions are axially coordinated by water molecules and limited their network expansion in the third dimension through bridging coordination of SiF_6^{2-}. So we chose NMP/MeOH solution to limit the effect of coordination competition from water molecules. SIFSIX-1-Ni, SIFSIX-1-Co, and SIFSIX-1-Cd were crystallized in tetragonal crystal system and *P4/m m m* space group. The crystallographic data and selected geometrical parameters are placed in **Table 3-1**. **Figure 3-1** (a)-(c) shows the coordination environment of SIFSIX-1-Ni, SIFSIX-1-Co, and SIFSIX-1-Cd. In the structure of SIFSIX-1-Ni, the disorder was present through the splitting of the aromatic ring. Nickel (II) center coordinates with four nitrogen atoms of four different 4,4′-bipyridine (Ni−N 2.086 Å), and two fluorine atoms of two different silicon hexafluoride anions (Ni−F 2.057 Å). Similarly, the Co−N bond and Co−F bond distances are 2.131 Å and 2.073 Å respectively in SIFSIX-1-Co. The Cd−N and the Cd−F bond distances are 2.316 Å and 2.265 Å, which is slightly longer than SIFSIX-1-Co and SIFSIX-1-Ni. The bipyridine ligands bridge the M(II) centers to produce a 2D sheet. The SiF_6^{2-} linkers serve as bridging ligands to link the 2D sheet and create a three-dimensional porous structure. The grids size is 11.36 × 11.36 Å in SIFSIX-1-Co (Co···Co distance), which is an example of these three MOFs to demonstrate (**Figure 3-1** (d)-(f)).

In the structure of SIFSIX-7-Ni, Cd, Zn (**Figure 3-2** (a)-(c)), molecule disorder in ethenyl moiety was observed in the three compounds. All of them were crystallized in the triclinic space group *C 2/m*. The crystallographic data are placed in **Table 3-2.** The

coordination geometry of the M^{2+} cations is same as that of SIFSIX-1-M. The Ni-N bond and Ni-F bond distances are 2.068 Å and 2.025 Å respectively, which are a little shorter than Cd-N (2.318 Å) and Cd-F (2.274 Å) bond respectively. As for SIFSIX-7-Zn, the Zn-N bond and Zn-F bond are 2.141 Å and 2.105 Å respectively. The grids of SIFSIX-7-Zn with a size of 13.48 × 13.48 Å (Zn···Zn distance) form a 3D structure with high porosity (**Figure 3-2** (d)-(e)). We also tried to use $CoSiF_6$ and 1,2-bis(4-pyridyl)ethane to synthesize SIFSIX-7-Co, unexpectedly, the only amorphous powder was generated. So, it is difficult for Co to form 3D SIFSIX pillared MOFs.

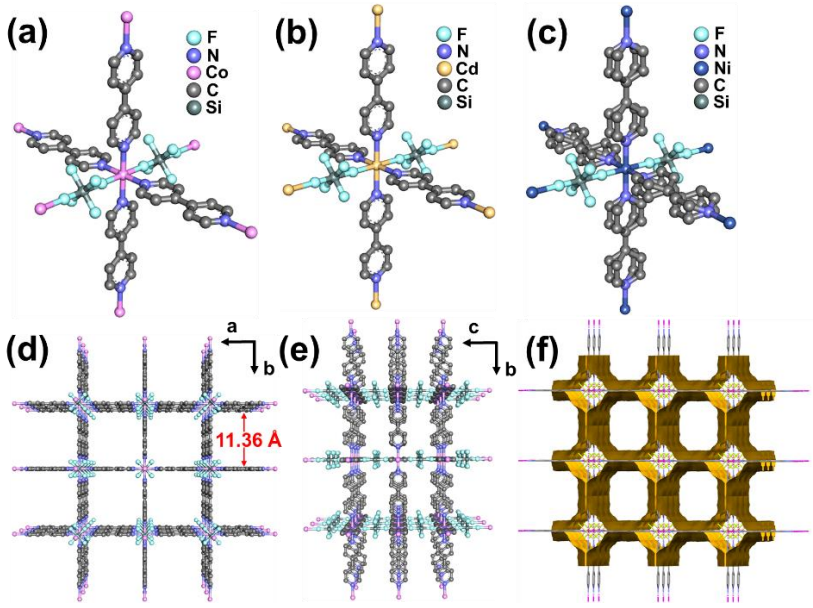

Figure 3-1. Crystal structures of (a) SIFSIX-1-Co. (b) SIFSIX-1-Cd. (c) SIFSIX-1-Ni. (d) 3D framework of SIFSIX-1-Co viewed along the 001 direction and (e) 3D framework of SIFSIX-1-Co viewed along the 100 direction. (f) The void structure of SIFSIX-1-Co with a probe radius of 1.2 Å.

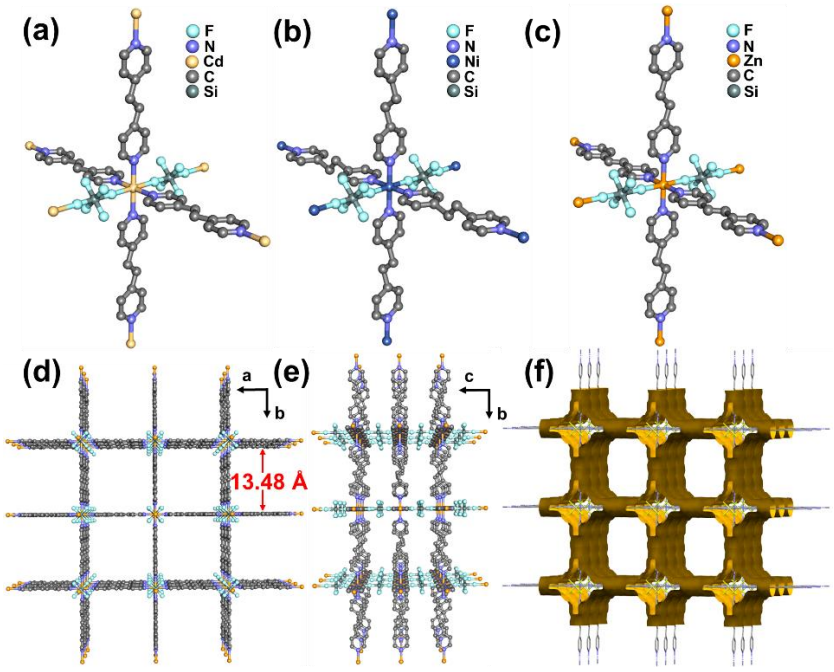

Figure 3-2. Crystal structures of (a) SIFSIX-7-Cd. (b) SIFSIX-7-Ni. (c) SIFSIX-1-Zn. (d) 3D framework of SIFSIX-7-Zn viewed along the 001 direction and (e) 3D framework of SIFSIX-1-Co viewed along the 100 direction. (f) The void structure of SIFSIX-7-Zn with a probe radius of 1.2 Å

Table 3-1. Crystal Data and Refinements for SIFSIX-1-M (M = Co, Ni, Cd)

	Co	Ni	Cd
Crystal System	Tetragonal	Tetragonal	Tetragonal
Space Group	*P4/nbm*	*P4/nbm*	*P4/nbm*
a (Å)	16.0607(5)	15.9497(4)	16.5397(5)
b (Å)	16.0607(5)	15.9497(4)	16.5397(5)
c (Å)	7.6013(4)	7.5668(3)	7.9420(4)
α (°)	90 °	90 °	90 °
β (°)	90 °	90 °	90 °
γ (°)	90 °	90 °	90 °
V (Å^3)	1960.73(16)	1924.94(12)	2172.63(17)
Z	2	2	2
Diffractometer	CCD	CCD	CCD
μ(mm^{-1})	0.505	0.572	0.562
Radiation type	Mo *Kα*	Mo *Kα*	Mo *Kα*
Radiation wavelength	0.71073	0.71073	0.71073
F(000)	518.0	520.0	560.0

Goodness of fit	1.160	1.053	1.044
Temperature (K)	93K	93K	93K
Reflections collected	4286	15908	20671
Independent	1375	1415	1605
R_1 ($I > 2.00\sigma(I)$)[a]	5.50 %	3.20 %	4.05 %
wR_2 ($I > 2.00\sigma(I)$)[b]	13.75 %	9.77 %	11.57 %

[a]$R_1 = \sum||F_o|-|F_c||/\sum|F_o|$, [b]$wR_2 = [\sum w|F_o^2-F_c^2|^2/\sum w(F_o^2)^2]^{1/2}$

Table 3-2. Crystal Data and Refinements for SIFSIX-7-M (M =Ni, Zn, Cd).

	Zn	Ni	Cd
Crystal System	Triclinic	Triclinic	Triclinic
Space Group	*C 2/m*	*C 2/m*	*C 2/m*
a (Å)	19.2732(7)	19.0506(8)	19.7467(5)
b (Å)	19.2689(7)	19.0536(8)	19.7655(5)
c (Å)	7.6688(2)	7.5081(4)	7.9736(2)
α (°)	90	90	90
β (°)	89.888(3)	90.002(4)	90.028(2)
γ (°)	90	90	90
V (Å^3)	2847.98(16)	2725.3(2)	3112.12(14)
Z	1	1	1
Diffractometer	CCD	CCD	CCD
μ(mm^{-1})	0.481	0.408	0.396
Radiation type	Mo *Kα*	Mo *Kα*	Mo *Kα*
Radiation wavelength	0.71073	0.71073	0.71073
F(000)	580.0	576.0	616.0
Goodness of fit	1.107	1.337	1.191
Temperature (K)	93K	93K	93K
Reflections collected	34564	35165	41481
Independent	3636	2969	4286
R_1 ($I > 2.00\sigma(I)$)[a]	6.01 %	9.94 %	4.20 %
wR_2 ($I > 2.00\sigma(I)$)[b]	17.98%	32.41 %	12.21 %

[a]$R_1 = \sum||F_o|-|F_c||/\sum|F_o|$, [b]$wR_2 = [\sum w|F_o^2-F_c^2|^2/\sum w(F_o^2)^2]^{1/2}$

Stability of MOFs

PXRD was used to characterize the crystallinity and purity of the six SIFSIX MOFs. **Figure 3-3** shows that the PXRD patterns of all of the as-synthesized samples are a good match with the simulated patterns from the single-crystal structure. To investigate the stability after removing the solvent, we used methanol to exchange the guest solvents in

the samples several times and degas at 100 °C for 12h. PXRD results show that peaks of SIFSIX-1-Cd, SIFSIX-1-Co, SIFSIX-1-Ni, and SIFSIX-7-Ni remain unchanged and the structures are maintained after degassing but the peak intensity of SIFSIX-1-Cd was greatly reduced, demonstrating the poor thermostability of SIFISX-1-Cd. In the case of SIFSIX-7-Cd and SIFSIX-7-Zn, the PXRD patterns were changed during the ethanol exchange step, indicating the transformation structural instability. As we can see, both of SIFSIX-1-Cd and SIFSIX-7-Cd exhibit unstable structures, the reason could be the long bond of Cd-N than Ni and Co are prone to breakage. In brief, among the six MOFs, SIFSIX-1-Co, Ni and SIFSIX-7-Ni can keep the stability after degassing and they can be used for future study.

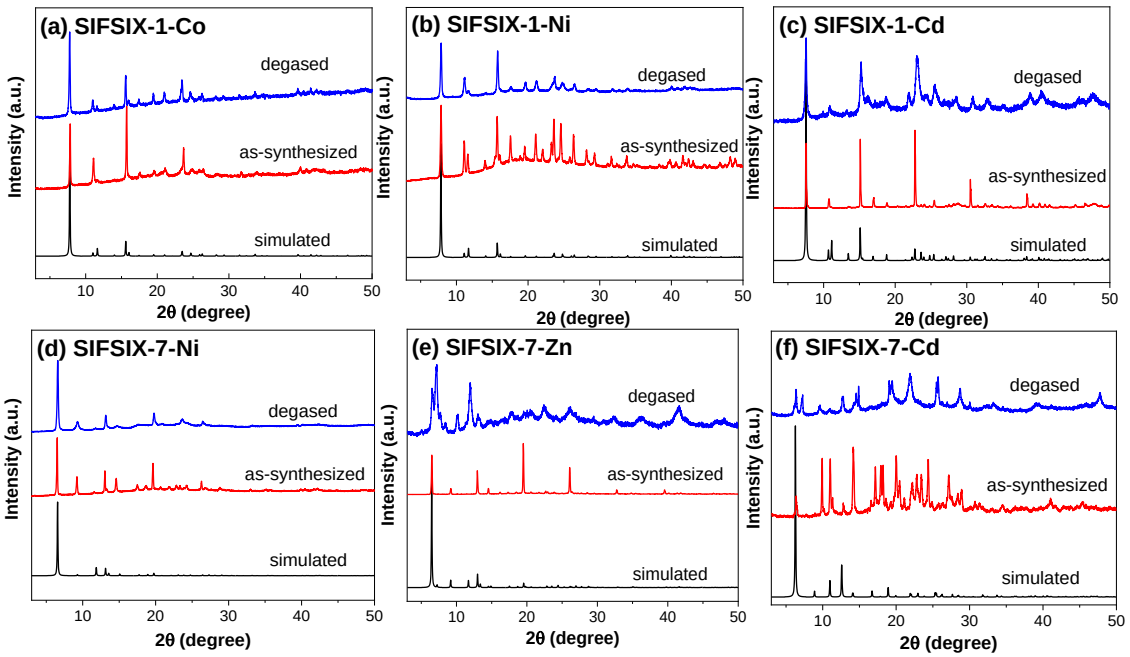

Figure 3-3. PXRD of simulated, as-synthesized, and degassed of SIFSIX-7-Ni

Except for using NMP/MeOH solution, we also obtained powder of SIFSIX-1-Ni and SIFSIX-1-Co using anhydrous solutions such as CH_3Cl/MeOH, EtOH/MeOH. However, the single crystals couldn't be formed and the crystallinity is much lower than NMP/MeOH solution. Those SIFSIX pillared MOFs not only can be crystallized into single crystals but also have high crystallinity.

As we mentioned previously, the existence of water may lead to the disruption of the 3D structure due to the coordination of metals with water molecules. So we investigated the stability of SIFSIX-1-Ni and SIFSIX-1-Co when exposed to a humid environment. After one week, we observed new peaks in PXRD pattern that correspond to 2D phase, and this peak became stronger after one month (**Figure 3-4** (a) and (b)**)**, indicating that the transformation from 3D to 2D phase occurred for SIFSIX-1-Ni. As for SIFSIX-1-Co, the 3D phase almost disappeared after 1 week and completely changed to the 2D phase in 1 month (**Figure 3-4** (c) and (d)**)**. So SIFSIX-1-Ni has better moisture stability than SIFSIX-1-Co, while both can be transformed to 2D phase from in humid environment. When they are stored in a dry environment, the 3D structure can remain even after a month. Interestingly, SIFSIX-7-Ni although exhibits similar transformation from 3D to the 2D phase, the reversal can be achieved by immersing the samples in methanol (**Figure 3-4** (e)**)**. This phenomenon is completely different from SIFSIX-1-Ni and SIFSIX-1-Co, which couldn't be restored to their original phase after soaking in methanol (**Figure 3-4** (f)**)**. In addition, the revisable transformation of SIFSIX-7-Ni exhibits cyclic properties of structural changes and repeated phase changes can be realized by controlling the environment. So we can easily suppress the 3D to 2D phase transformation by simply controlling the humidity in the environment.

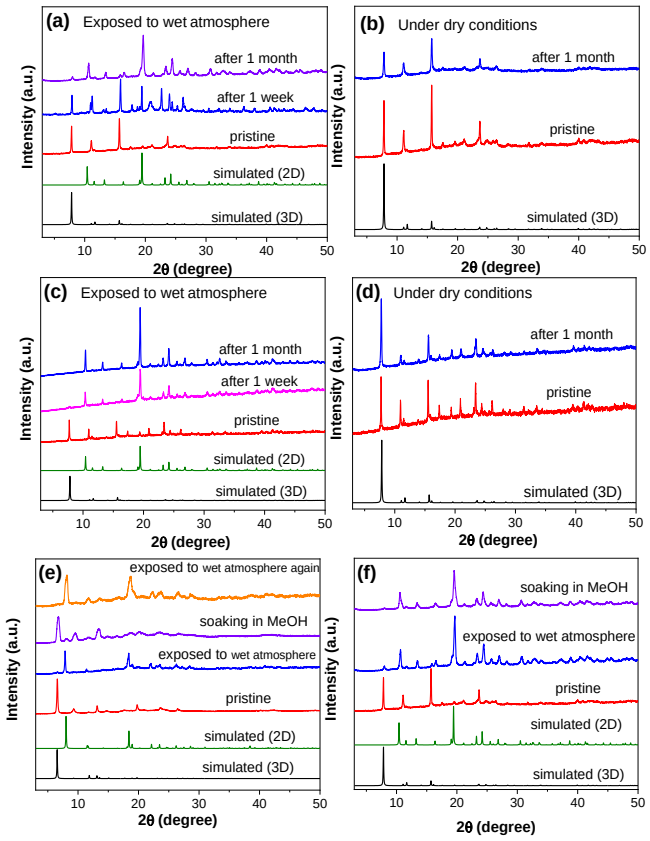

Figure 3-4. (a) and (b): PXRD patterns of SIFSIX-1-Ni after exposing to wet atmosphere and dry conditions. (c) and (d): PXRD patterns of SIFSIX-1-Co after exposing to wet atmosphere and dry conditions. (e): PXRD patterns of SIFSIX-7-Ni after exposing in air and soaking in methanol for 10 min and simulated of 2D and 3D phase. (f): PXRD patterns of SIFSIX-1-Ni after exposing in air and soaking in methanol and simulated of 2D and 3D phase.

Gas sorption and IAST selectivities of SIFSIX-1-Co and SIFSIX-1-Ni

The gas sorption properties of SIFSIX-1-Ni and SIFSIX-1-Co were studied with N_2 at 77K, CO_2 at 194.7K, and C_2H_2 at 189.5K. SIFSIX-1-Ni has a similar sorption property to SIFSIX-1-Co. The type I sorption isotherm in **Figure 3-5** indicates the microporous structure of SIFSIX-1-Ni and SIFSIX-1-Co. To further study the selective adsorption of SIFSIX-1-Ni and SIFSIX-1-Co, we measured the different gas sorption isotherms at 273K and 298 K, as shown in **Figure 3-6**, both of the SIFSIX-1-Ni and SIFSIX-1-Co

show preferential adsorption for C_2H_2 over C_2H_4 and C_2H_6. The uptake in 1 bar for C_2H_2 of SIFSIX-1-Ni is 8.14 mmol/g at 273 K and 7.23 mmol/g at 298 K, which is much higher than C_2H_4 (5.67 mmol/g at 273 K and 3.41 mmol/g at 298 K) and C_2H_6 (5.60 mmol/g at 273 K and 3.73 mmol/g at 298 K). The adsorption capacity of SIFSIX-1-Co is similar to SIFSIX-1-Ni. In addition, the SIFSIX-1-Ni and SIFSIX-1-Co also have a high affinity for CO_2 with high capacity (**Figure 3-7)**. The uptake in 1 bar for CO_2 of SIFSIX-1-Ni is 6.61 mmol/g at 273 K and 3.43 mmol/g at 298 K. They have the potential for the CO_2/N_2 separation.

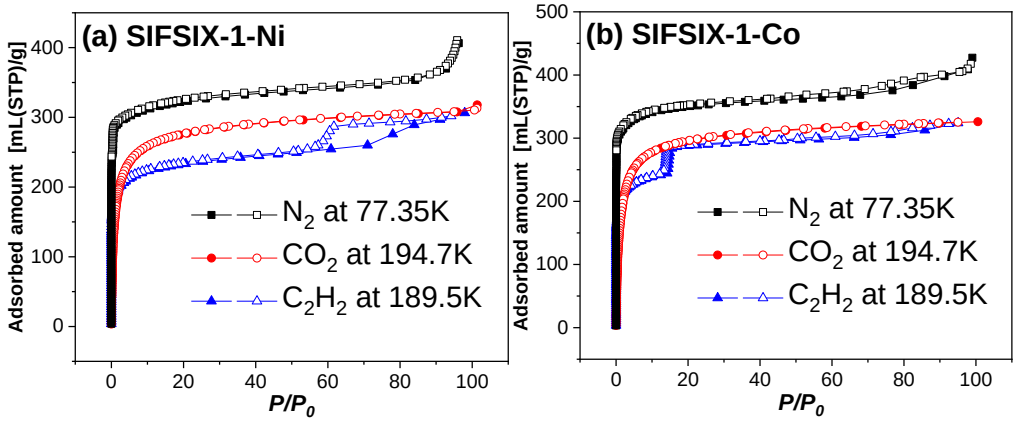

Figure 3-5. N_2, CO_2 and C_2H_2 sorption isotherms of (a) SIFSIX-1-Ni and (b) SIFSIX-1-Co at the boiling point.

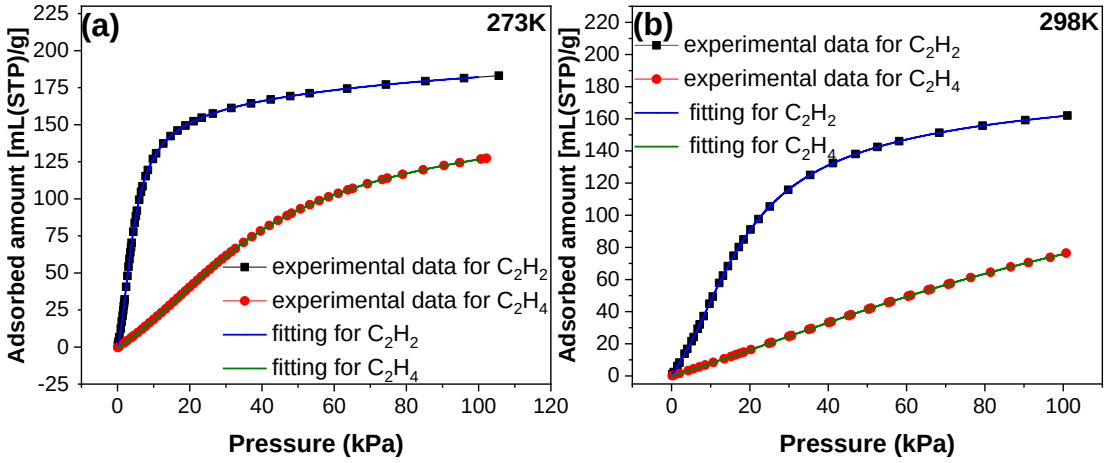

Figure 3-6. Dual site Langmuir fitting curves of C_2H_2 and C_2H_6 adsorption isotherms for SIFSIX-1-Ni. Dots are experimental data; lines are fitting curves.

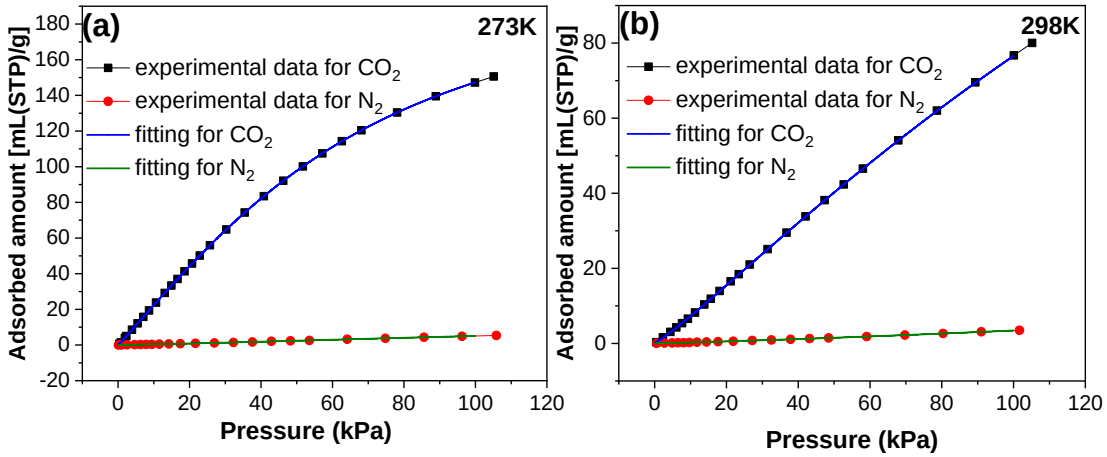

Figure 3-7. Dual site Langmuir fitting curves of CO_2 and N_2 adsorption isotherms for SIFSIX-1-Ni. Dots are experimental data; lines are fitting curves.

Table 3-3. Dual site Langmuir fitting parameters for C_2H_2 adsorption for SIFSIX-1-Ni

C_2H_2	273K	298K
$q_{m,1}$	124.55584	110.16024
$q_{m,1}$	107.73067	83.11693
b_1	0.05643	0.03729
b_2	0.0715	0.00208
n_1	1.94301	0.92866
n_2	0.60522	2.18569
R^2	0.999991	0.999997

Table 3-4. Dual site Langmuir fitting parameters for C_2H_4 adsorption for SIFSIX-1-Ni

C_2H_4	273K	298K
$q_{m,1}$	129.82807	228.0738
$q_{m,1}$	41.92595	30.44213
b_1	0.01086	0.00342
b_2	0.000141528	0.000147785
n_1	1.14043	0.99258
n_2	2.48696	2.03044
R^2	0.999997	0.999996

Table 3-5. Dual site Langmuir fitting parameters for CO_2 adsorption for SIFSIX-1-Ni

CO_2	273K	298K
$q_{m,1}$	147.70501	286.75437
$q_{m,1}$	74.39916	301.14066

b_1	0.01387	0.00062264
b_2	0.000409053	0.0017
n_1	1.0566	0.12801
n_2	1.88251	1.14993
R^2	0.999999	0.999995

Table 3-6. Dual site Langmuir fitting parameters for N_2 adsorption for SIFSIX-1-Ni

N_2	273K	298K
$q_{m,1}$	86.3058	69.41059
$q_{m,1}$	5.1123	9.39784
b_1	0.00058608	0.0000123406
b_2	0.000096143	0.00303
n_1	0.87732	1.67364
n_2	1.9666	0.9143
R^2	0.999856	0.999832

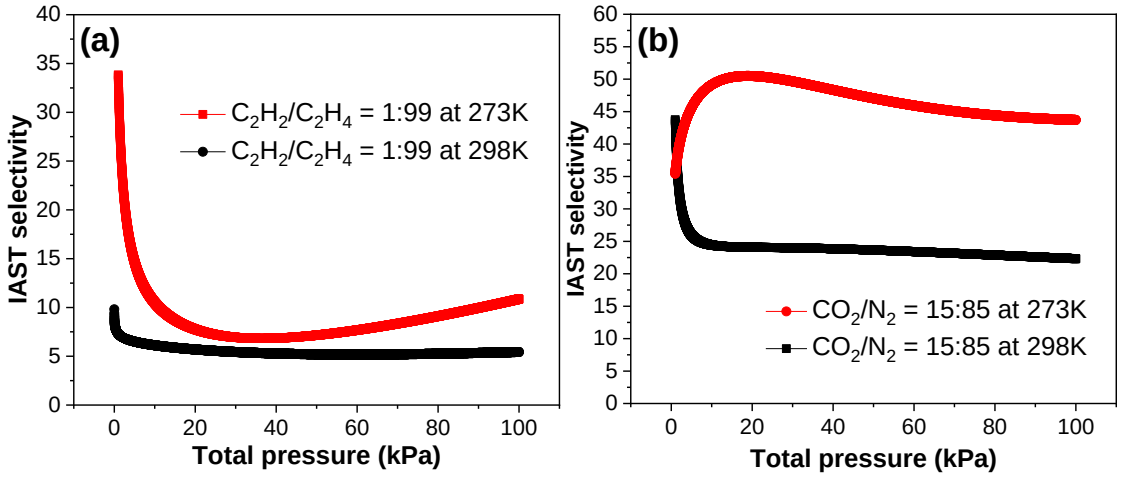

Figure 3-8. IAST selectivities of SIFSIX-1-Ni at different temperatures: (a) C_2H_2/C_2H_4; (b) CO_2/N_2.

Ideal Adsorbed Solution Theory (IAST) was applied to investigate the potential adsorption selectivities of SIFSIX-1-Ni and SIFSIX-1-Co for C_2H_2/C_2H_4 and CO_2/N_2. The fitting parameters are gathered in **Table 3-3 – 3-6.** In industrial applications, the polymer-grade C_2H_4 often contains trace amounts of C_2H_2 (about 1%). The combustion of coal in air generates flue gas with a relatively low CO_2 concentration (15-16%), while the bulk of the effluent is mainly composed of N_2. So we set the mixture ratio to 1/99 for

C_2H_2/C_2H_4 and 15/85 for CO_2/N_2. The results were shown in **Figure 3-8**. SIFSIX-1-Ni displays a high selectivity of 43.7 at 273 K in 1 bar conditions with CO_2/N_2 mixed in a 15/85 molar ratio and 22.3 at 298K and 1 bar, which is higher than some reported MOFs with high CO_2/N_2 selectivity.[22,23] In addition, the IAST selectivity is 5.44 for C_2H_2/C_2H_4 (1/99) mixtures at 298 K and 10.86 at 273K in 1 bar. These values also surpass the values reported for some microporous MOFs for C_2H_2/C_2H_4 separation.[24] The results confirm that the SIFSIX-1-Ni can be used in the CO_2 capture from coal-fired power plants and purification of ethylene in industrial production.

Gas sorption and IAST selectivities of SIFSIX-7-Ni

The adsorption property of SIFSIX-7-Ni was also investigated. The type I sorption isotherms of N_2 at 77K, CO_2 at 273K, and C_2H_2 at 189.5K are displayed in **Figure 3-9** indicating the characteristics of the micropores. Sorption isotherms of CO_2, N_2, C_2H_2, C_2H_4, and C_2H_6 for SIFSIX-7-Ni at 273 and 298 K up to 1 bar were measured to explore the abilities for adsorption and separation for these gases. As shown in **Figure 3-10**, SIFSIX-7-Ni also shows a higher adsorption amount of C_2H_2 than C_2H_4 and C_2H_6 at 273K and 298K. C_2H_2/C_2H_4 selectivity for SIFSIX-7-Ni was predicted by IAST (fitting parameters that are gathered in **Table 3-7 – 3-10**). The calculated adsorption selectivities for C_2H_2/C_2H_4 mixed in a 1:99 molar ratio was 2.65 at 273K and 2.97 at 298K, 1bar (**Figure 3-12** (a)). Since SIFSIX-7-Ni also has a high CO_2 adsorption amount than N_2 (**Figure 3-11)**, IAST selectivity was calculated for CO_2/N_2 mixtures. The selectivity can reach 23.5 at 273 K and 1 bar conditions with CO_2/N_2 mixed in a 15:85 molar ratio and 14.5 at 298K and 1 bar (**Figure 3-12** (b)). These values are lower than SIFSIX-1-Ni, the reason should be the lower CO_2 adsorption amount of SIFSIX-7-Ni compared to that of SIFSIX-1-Ni.

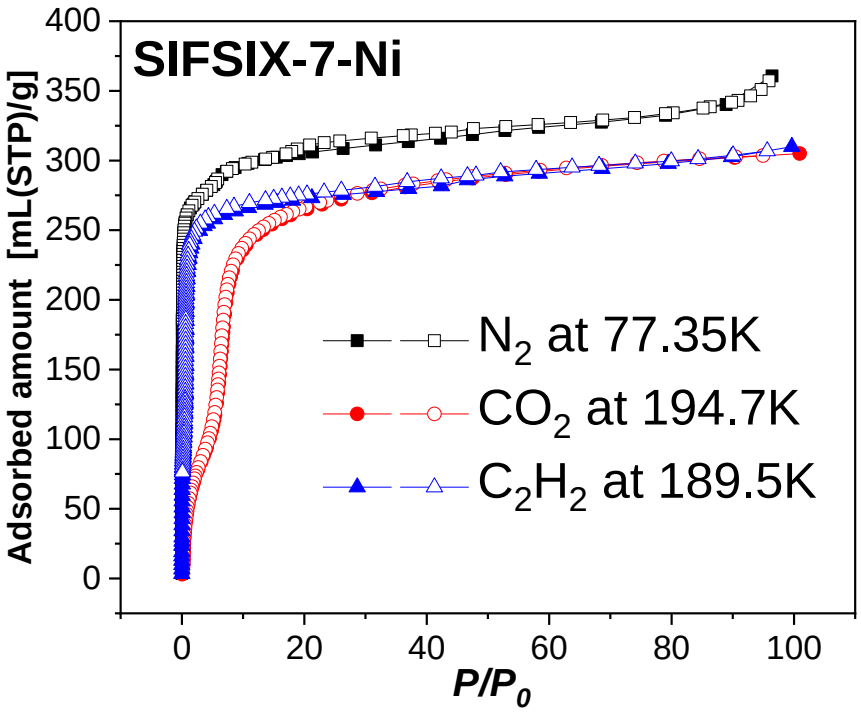

Figure 3-9. Figure 6. (a) N_2, CO_2 and C_2H_2 sorption isotherms of SIFSIX-7-Ni at the boiling point. (b)-(d) CO_2, N_2, C_2H_2, C_2H_4 and C_2H_6 sorption isotherms of SIFSIX-7-Ni at 273 and 298 K.

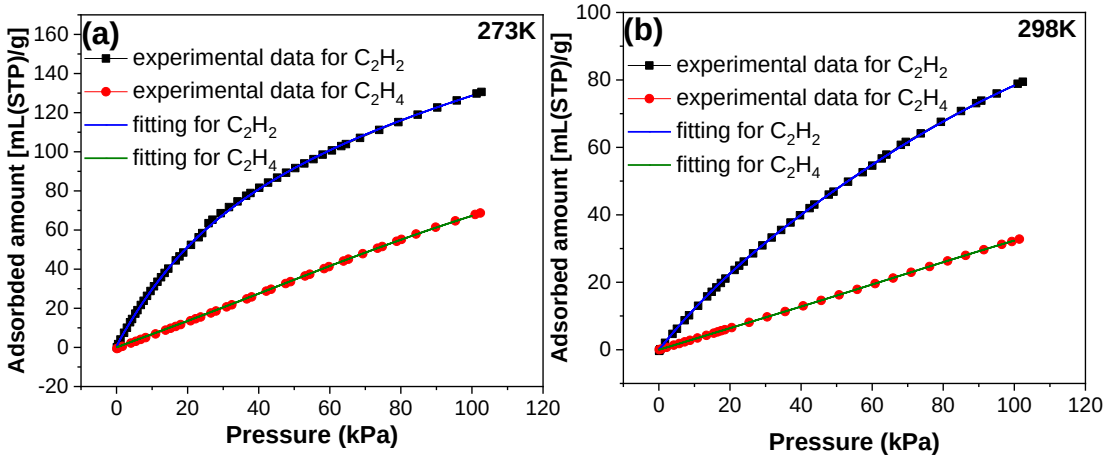

Figure 3-10. Dual site Langmuir fitting curves of C_2H_2 and C_2H_6 adsorption isotherms for SIFSIX-7-Ni. Dots are experimental data; lines are fitting curves.

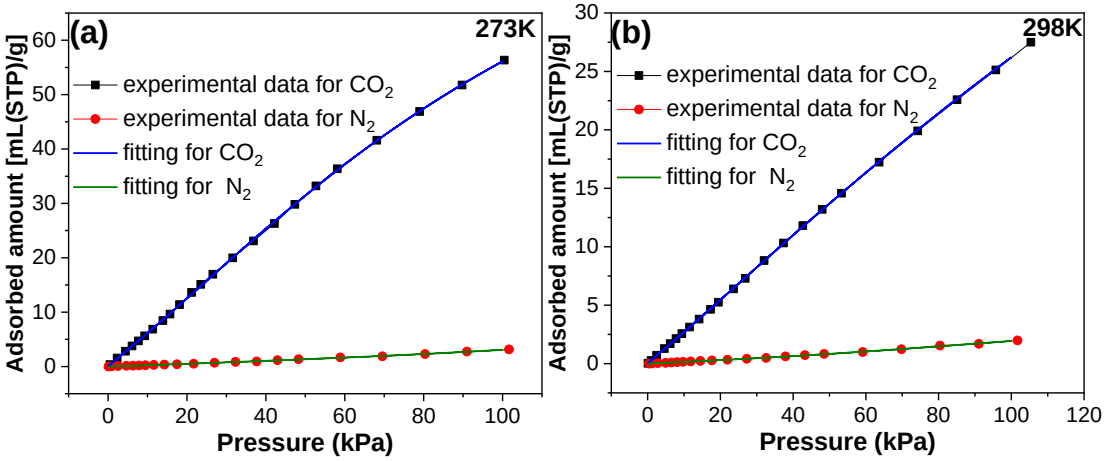

Figure 3-11. Dual site Langmuir fitting curves of CO_2 and N_2 adsorption isotherms for SIFSIX-7-Ni. Dots are experimental data; lines are fitting curves.

Table 3-7. Dual site Langmuir fitting parameters for C_2H_2 adsorption for SIFSIX-7-Ni

C_2H_2	273K	298K
$q_{m,1}$	1893.33392	125.93051
$q_{m,1}$	70.82406	22.73359
b_1	0.00164	0.01025
b_2	0.0142	0.00000229387
n_1	0.68384	1.01668
n_2	1.26921	2.85203
R^2	0.999820	0.999977

Table 3-8. Dual site Langmuir fitting parameters for C_2H_4 adsorption for SIFSIX-7-Ni

C_2H_4	273K	298K
$q_{m,1}$	166.61441	129.97313
$q_{m,1}$	50.69229	13.86537
b_1	0.0043	0.0024
b_2	0.0000598335	0.00000147546
n_1	0.97146	1.02018
n_2	2.04753	2.81052
R^2	0.999999	0.999998

Table 3-9. Dual site Langmuir fitting parameters for CO_2 adsorption for SIFSIX-7-Ni

CO_2	273K	298K
$q_{m,1}$	81.30177	327.14514

$q_{m,1}$	37.56552	127.55068
b_1	0.000683375	0.0004311
b_2	0.01654	0.00135
n_1	1.54927	0.50045
n_2	0.88622	1.12621
R^2	0.999892	0.999962

Table 3-10. Dual site Langmuir fitting parameters for N_2 adsorption for SIFSIX-7-Ni

N_2	273K	298K
$q_{m,1}$	33.13589	6.02151
$q_{m,1}$	31.48505	3.17813
b_1	0.00000000177801	0.00279
b_2	0.000643639	0.00000709055
n_1	3.45204	0.95527
n_2	1.07349	2.34763
R^2	0.998851	0.998921

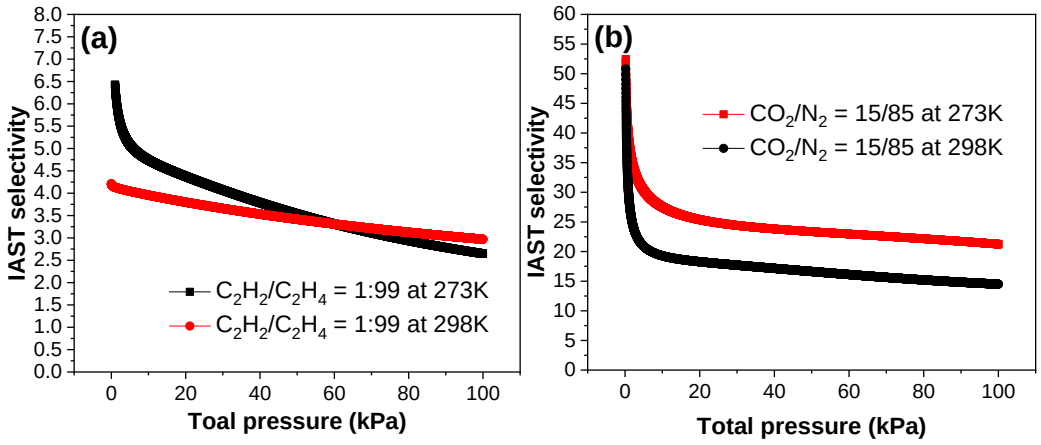

Figure 3-12. (a) N_2, CO_2 and C_2H_2 sorption isotherms of SIFSIX-7-Ni at the boiling point. (b)-(d) CO_2, N_2, C_2H_2, C_2H_4 and C_2H_6 sorption isotherms of SIFSIX-7-Ni at 273 and 298 K.

Calculation of the heat of adsorption(Q_{st})

What's more, we calculated the adsorption heat (Qst) of C_2H_2, C_2H_4, and C_2H_6 (The fitting parameters shown in **Figure 3-13** for SIFSIX-1-Ni and **Figure 3-13** for SIFSIX-1-Ni). **Figure 3-15** (a) shows the Q_{st} of SIFSIX-1-Ni, the Q_{st} of C_2H_2 is much higher than

that of C_2H_4 and C_2H_6, the Q_{st} value of C_2H_2 near-zero loading is 31.48 kJ·mol^{-1}. For C_2H_4 and C_2H_6, the zero-loading Q_{st} values are 21.67 and 20.63 kJ·mol^{-1}, respectively. This property is also similar to that of SIFSIX-1-Cu in which C_2H_2 molecules are bound through strong C–H···F hydrogen (H) bonding with the SiF_6^{2-} site and van der Waals (vdW) interactions with the 4,4′-bipyridine linkers. So SIFSIX-1-Ni exhibits exceptionally high C_2H_2 uptake than C_2H_4 and C_2H_6. The Q_{st} for C_2H_2, C_2H_4, and C_2H_6 of SIFSIX-7-Ni were also calculated based on the adsorption isotherms. As shown in **Figure 3-15** (b), SIFSIX-7-Ni has the Q_{st} of 28.92 kJ mol^{-1} at zero coverage for C_2H_2, while the Q_{st} at zero coverage was found to be 21.99 and 20.05 kJ mol^{-1} for C_2H_4 and C_2H_6, respectively. This difference could be that SIFSIX-7-Ni has a larger pore size and weaker vdW potential overlap resulting in a lower adsorption amount of C_2H_2, which also was proved in the structure of SIFSIX-2-Cu[13].

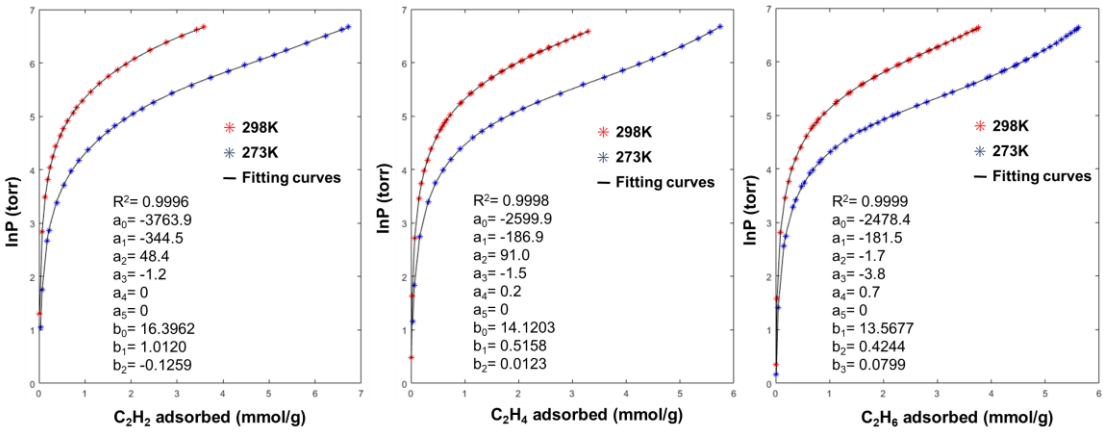

Figure 3-13. The details of virial equation (solid lines) fitting to the experimental adsorption data for SIFSIX-1-Ni.

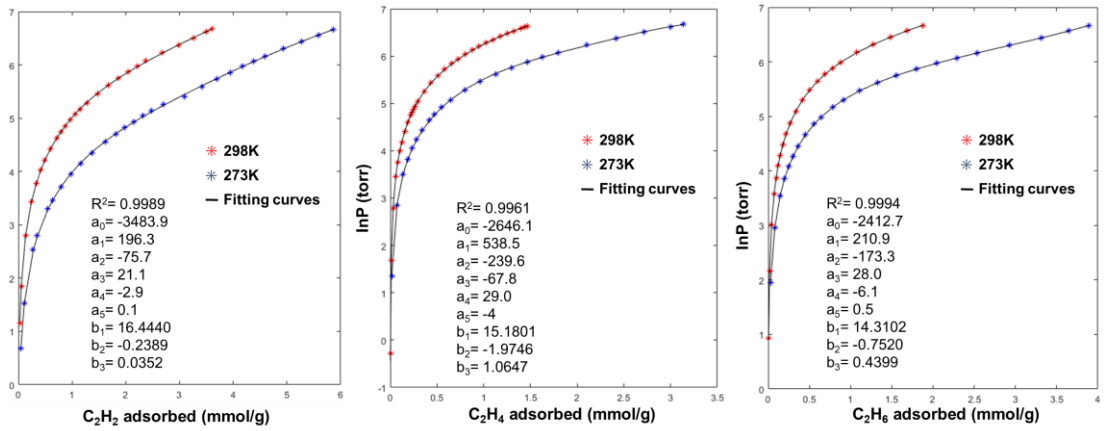

Figure 3-14. The details of virial equation (solid lines) fitting to the experimental adsorption data for SIFSIX-7-Ni.

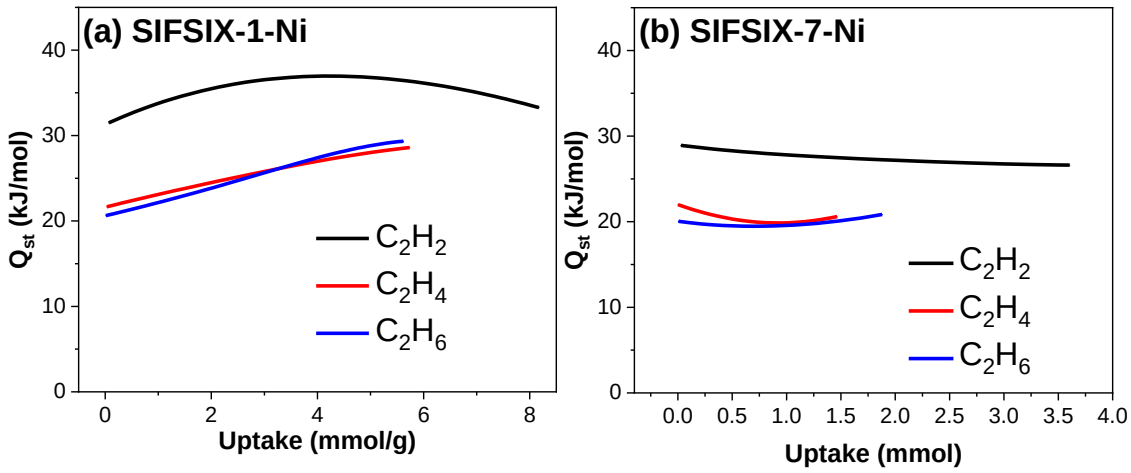

Figure 3-15. Calculated adsorption heat (Q_{st}) of C_2H_2, C_2H_4, and C_2H_6 of (a) SIFSIX-1-Ni and (b) SIFSIX-7-Ni estimated from virial expression fits at 273 and 298 K.

3-4. Conclusions

In summary, we synthesized single-crystal structures of three new SIFSIX MOFs based on 4,4'-bipyridine and three new MOFs based on 1,2-bis(4-pyridyl) ethane by self-assembly with metallic hexafluorosilicate. Moreover, SIFSIX-1-Ni, SIFSIX-1-Co, and SIFSIX-7-Ni can maintain their structures after removal of the solvents and they exhibit

permanent porosity. The study reveals that all the three materials are very promising for their applications in CO_2 capture from flue gas and in the removal of trace amounts of C_2H_2 from C_2H_4.

3-5. References

1 H. Li, M. Eddaoudi, M O'Keeffe, O. M Yaghi, *Nature*, 1999, **402**, 276-279.

2 R. Matsuda, R. Kitaura, S. Kitagawa, Y. Kubota, T. C. Kobayashi, S. Horike, M. Takata, *J. Am. Chem. Soc.*, 2004, **126**, 14063–14070.

3 D. Ma, B. Li, X. Zhou, Q. Zhou, K. Liu, G. Zeng, G. Li, Z. Shi, S. Feng. *Chem. Commun.*, 2013, **49**, 8964-8966.

4 M. Drobek, J. H Kim, M. Bechelany, C. Vallicari, A. Julbe, S. S. Kim, *ACS Appl. Mater. Interfaces*, 2016, **8**, 8323-8328.

5 G. K. H Shimizu, J. M Taylor, S. R Kim, *Science*, 2013, **341**, 354-355.

6 H. A Patel, N. Mansor, S. Gadipelli, D. J. L. Brett, Z. Guo, *ACS Appl. Mater. Interfaces*, 2016, **8**, 30687-30691.

7 S. Noro, S. Kitagawa, M. Kondo, K. Seki, *Angew. Chem. Int. Ed.*, 2000, **39**, 2082-2084.

8 P. Nugent, V. Rhodus, T. Pham, B. Tudor, K. Forrest, L. Wojtas, B. Space, M. J. Zaworotko, *Chem. Commun.*, 2013, **49**, 1606-1608.

9 P. Nugent, Y. Belmabkhout, S. D. Burd, A. J. Cairns, R. Luebke, K. Forrest, T. Pham, S. Q. Ma, B. Space, L. Wojtas, M. Eddaoudi, M. J. Zaworotko, *Nature*, 2013, **495**, 80-84.

10 S. Subramanian, M. J. Zaworotko, Angew. Chem. Int. Ed., 1995, **34**, 2127-2129.

11 J. Zheng, X. Cui, Q. Yang, Q. Ren, Y. Yang, H. Xing, *Chem. Eng. J.*, 2018, **354**, 1075-1082.

12 S. D. Burd, S. Q. Ma, J. A. Perman, B. J. Sikora, R. Q. Snurr, P. K. Thallapally, J. Tian, L. Wojtas, M. J. Zaworotko, *J. Am. Chem. Soc.*, 2012, **134**, 3663-3666.

13 X. Cui, K. Chen, H. Xing, Q. Yang, R. Krishna, Z. Bao, H. Wu, W. Zhou, X. Dong,

Y. Han, B. Li, Q. Ren, M. J. Zaworotko, B. Chen, *Science*, 2016, **353**, 141-144.

14 S. Mukherjee, N. Kumar, A. A Bezrukov, K. Tan, T. Pham, K. A. Forrest, K. A. Oyekan, O. T. Qazvini, D. G. Madden, B. Space, M. J. Zaworotko, *Angew. Chem. Int. Ed.*, 2021, **60**, 10902-10909.

15 S. K Elsaidi, M. H. Mohamed, H. T. Schaef, A. Kumar, M. Lusi, T. Pham, K. A. Forrest, B. Space, W. Xu, G. J. Halder, J. Liu, M. J. Zaworotko, P. K. Thallapally, *Chem. Commun.*, 2015, **51**, 15530-15533.

16 O. Shekhah, Y. Belmabkhout, K. Adil, P. M Bhatt, A. J. Cairns, M. Eddaoudi, *Chem. Commun.*, 2015, **51**, 13595-13598.

17 S. K Elsaidi, M. H Mohamed, C. M Simon, E. Braun, T. Pham, K. A. Forrest, W. Xu, D. Banerjee, B. Space, M. J. Zaworotko P. K. Thallapally, *Chem. Sci.*, 2017, **8**, 2373-2380.

18 C. Gu, Z. Yu, J Liu, D. S Sholl, *ACS Appl. Mater. Interfaces*, 2021, **13**, 11039-11049.

19 M. J. Lin, A. Jouaiti, N. Kyritsakas and M. W. Hosseini, *CrystEngComm*, 2011, **13**, 776-778.

20 M. J. Lin, A. Jouaiti, N. Kyritsakas and M. W. Hosseini, *CrystEngComm*, 2009, **11**, 189-191.

21 M. Y. Sun, X. Z. Wang, Z. Y Chen, X. P Zhou, D. Li, *Inorg. Chem.*, 2019, **58**, 12501-12505.

22 B. Zheng, Z. Yang, J. Bai, Y. Li, S. Li, *Chem. Commun.*, 2012, **48**, 7025−7027.

23 Z. Lu, F. Meng, L. Du, W. Jiang, H. Cao, J. Duan, H. Huang, H. He, *Inorg. Chem.*, 2018, **57**, 14018−14022.

24 H. M Wen, B. Li, H. Wang, R. Krishna, B. Chen, *Chem. Commun.*, 2016, **52**, 1166-1169.

Chapter 4

Fabrication of a kagomé-type MOF membrane by seeded growth on amino-functionalized porous Al_2O_3 substrate

4-1. Introduction

Metal-Organic Frameworks (MOFs) are a new class of crystalline porous solid materials for gas storage, [1,2] separations, [3,4] heterogeneous catalysis, [5] drug delivery [6] and so on. Their structures are one, two, or three-dimensional periodic networks formed by the bridging of metal ion-based nodes and organic ligands. An important essence of MOFs is the large specific surface area and tunable pore size, structure and functionality. [7-9] In the past few decades, MOF membranes for gas and liquid separations have been extensively studied. [10-12] However, it remains challenging to prepare a continuous and high-quality MOF membrane for practical gas separation applications, owing to the low affinity between the MOFs and substrates. For example, the direct growth of MOF membranes by immersing substrates in the solution of metal ions and organic ligands is the primary fabrication method. [13] However, it often leads to heterogeneous nucleation of MOF crystals resulting in the formation of defects, although chemical modification of substrates sometimes can improve it. [14,15] Instead of direct growth, the secondary growth method, where MOF membrane is grown from the substrate with seed MOF crystals, is regarded as a promising method. In the secondary growth method, the fabrication of a continuous seed layer is one of the key processes. Nevertheless, the preparation of a homogeneous seed layer is not easy due to the poor adhesion bond between MOF particle and surface of common substrate materials such as Al_2O_3. Some methods have been developed so far to prepare a uniform seed layer. [16-19] 3-aminopropyltriethoxysilane(APTEs) is used to chemically modifysubstrates to enhance the interaction between the substrate surface and MOF. [20,21] The layer-by-layer (LBL) growth method is a commonly used technique to fabricate thin MOF films known as surMOF by immersing the substrate into solutions of ligands and metal ions repeatedly. [22-24] However, the studies on the preparation of two-dimensional (2D) MOF membrane

by LBL growth are still limited since 2D MOF has high aspect ratio of crystals, which often prevents dense packing of crystals.

In this study, a new membrane based on [Cu(OEt-ipa)] (Kgm-OEt, OEt-ipa = 5-Ethoxyisophthalate) was prepared by secondary growth method on Al_2O_3 substrate. Kgm-OEt having an infinite kagom é-type 2D sheet structure. [25-27] Kgm-OEt is formed through the connection between Cu paddle-wheel units by the OEt-ipa ligands. The 2D sheets create two kinds of one-dimensional (1D) infinite channels along the c axis; one channel is triangular and contains only coordinated water molecules on the paddle wheel SBUs. Another pore has hexagonal geometry and contains all the alkoxy groups pointed towards the pore center. The cross-sectional size of the two channels is around 3.5 Å after the removal of coordinated solvent molecules. The channel is larger than the kinetic diameter of H_2 (2.89 Å) and smaller than those of N_2 (3.64 Å), CH_4 (3.80 Å) and C_2H_4 (4.20 Å). In this study, we employed a combination of surface modification of Al_2O_3 substrate and LBL seeding method to fabricate seed layer followed by the secondary solvothermal crystal growth forming continuous Kgm-OEt membrane (**Scheme 4-1**).

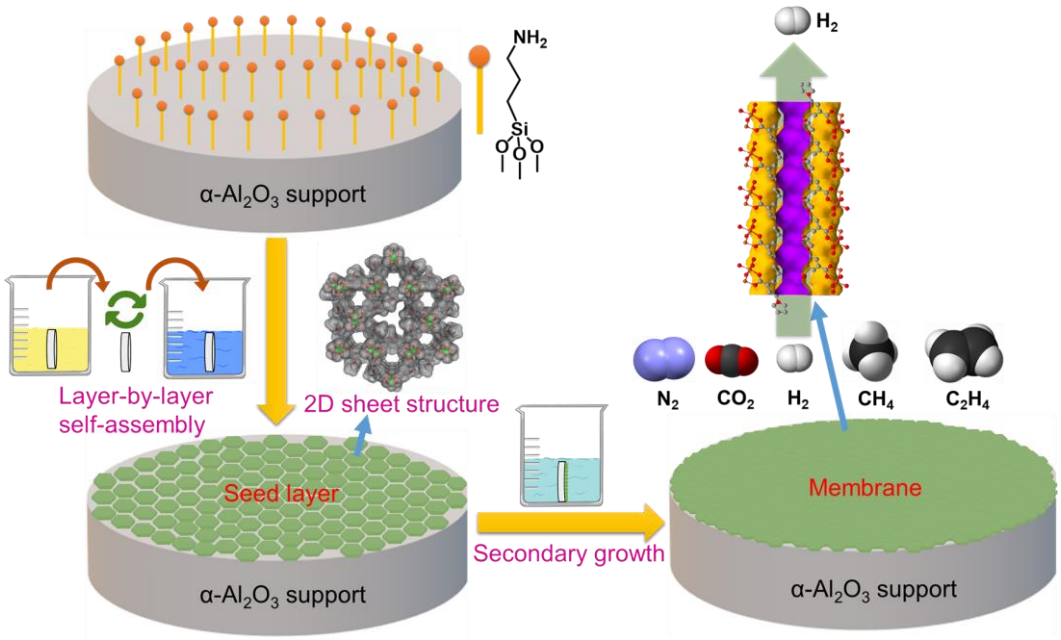

Graphical abstract

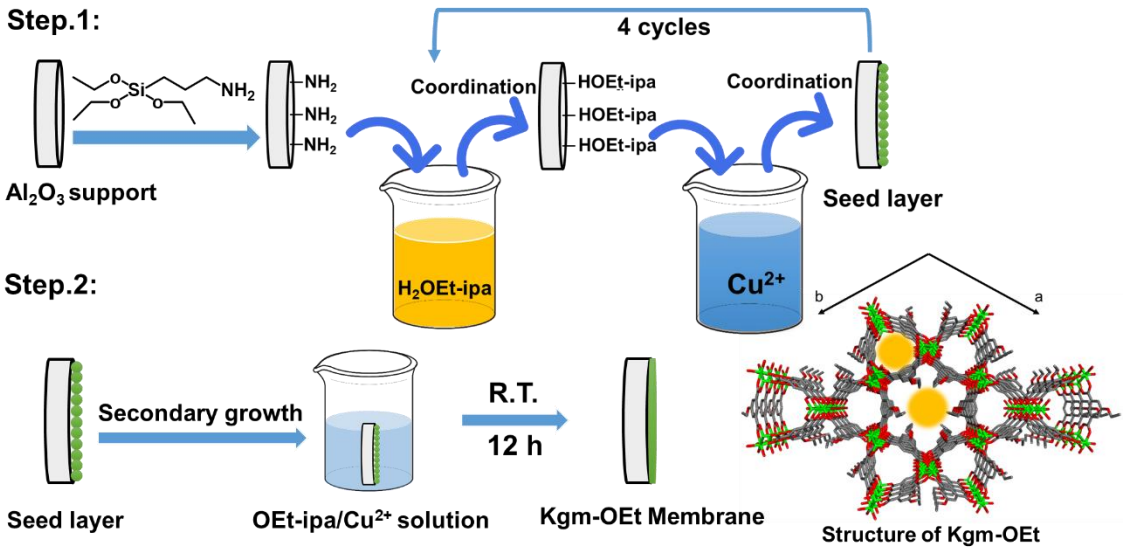

Scheme 4-1. Schematic diagram for the preparation of the membrane and the structure of Kgm-OEt. Atoms are colored as follows: Cu, green; O, red; C, gray.

2-2. Experimental

Chemicals

$Cu(NO_3)_2\ _3H_2O$ (wako, 99%). Methanol (wako, 99.8%). Dimethyl 5-hydroxyisophthalate (TCI, 98%). Ethyl iodide (TCI, 99%). Potassium carbonate (TCI, 99%). Acetone (Nacalai, 99.5%). Ethyl acetate (Nacalai, 99%). Hexane (Nacalai, 95%). NaOH (TCI, 97%). HCl (nacalai, 36%~38%). (3-aminopropyl) triethoxysilane (Aldrich, 99%).. Porous α-Al_2O_3 disks (Fraunhofer Institute IKTS, former HITK/Inocermic, Hermsdorf, Germany: 18 mm in diameter, 1.0 mm in thickness, 70 nm particles in the top layer) were used as substrates.

Synthesis of H_2OEt-ipa

H_2OEt-ipa was synthesized according to the procedures reported by Bloch et al. [24] with minor modifications. Dimethyl 5-hydroxyisophthalate (6.00 g, 28.55 mmol), ethyl iodide (4.57 mL, 57.1 mmol), K_2CO_3 (15.8 g, 114 mmol) and acetone (100 mL) were successively added to a 500 mL flask. The mixture was heated to 80 ℃ with stirring for 24 h. After the reaction mixture was cooled down to room temperature, water was added,

and the organic layer was separated. After evaporation of the solvent, the crude solids were separated by silica-gel column chromatography using dichloromethane as an eluent to obtain dimethyl 5-ethoxyisophthalate. In the second step, a mixture of dimethyl 5-ethoxyisophthalate (6.4 g, 27.1 mmol), sodium hydroxide (4.57 g, 114 mmol), water (50 mL) and methanol (150 mL) was heated to 50 ℃ and stirred for 1 day. After the removal of methanol under reduced pressure, hydrochloric acid was added to acidify the solution. The resulting precipitate was collected by filtration, washed with water, and dried under vacuum to obtain H_2OEt-ipa (5.68 g, yield:88.7%). ^{1}H NMR (300 MHz, DMSO-d_6): δ = 13.28 (s, 2H, OH), 8.06 (s, 1H, CH arom), 7.62 (s, 2H, CH arom), 4.14 (q, 2H, CH_2), 1.36 (t, 3H, CH_3).

APTEs modification on the Al_2O_3 substrate surface

Porous Al_2O_3 substrate was firstly activated by hydrochloric acid (2 M) for 24 h then heated in a solution of 3-aminopropyltriethoxysilane (APTEs) (0.06 ml) in 20 mL toluene for 3 h at 110 ℃ under argon atmosphere. Afterward, the APTEs-modified substrate was washed with water and dried before use.

Preparation of Kgm-OEt seed layer

APTEs-modified Al_2O_3 substrates were firstly immersed in a 50.0 mM H_2OEt-ipa in MeOH for 20 min and then in a 50.0 mM $Cu(NO_3)_2 \cdot 3H_2O$ in MeOH for 20 min at room temperature. In each step, the substrates were washed with MeOH. The whole procedure was repeated four cycles then dried at 80 ℃ for 3 h. For comparison, the same procedure was applied to unmodified Al_2O_3 substrates.

Preparation of Kgm-OEt membrane

A seeded Al_2O_3 substrate was vertically placed in a beaker filled with a precursor solution of 60 mg $Cu(NO_3)_2 \cdot 3H_2O$ (60 mg), H_2OEt-ipa (52.5 mg) and pyridine (20 μL) in MeOH (40 mL). After immersion for 12 h at room temperature, the substrate was taken out and rinsed with fresh MeOH to remove the loosely mounted powders on the surface,

and then immersed in 50 mL fresh methanol for another 12 h. Finally, the membrane was stored under a vacuum for use. Powder samples were collected from the mother solution.

Characterization

X-ray diffraction (XRD) patterns of the MOF membranes and MOF powders were measured by a Rigaku X-ray diffractometer with Cu *K*α radiation. Field emission scanning electron microscope (FESEM) pictures were taken by a JEOL JED-2300F, using an acceleration voltage of 15 kV. Thermogravimetric analysis (TGA) was performed using a Rigaku TP-EVO2 SL DyTG/DTA TypeJ under N_2 stream scanning from 30 to 500 ℃ with the temperature ramp of 5 ℃ min^{-1}.

Gas permeance measurement

The gas permeation measurements were conducted with a Wicke-Kallenbach setup (**Scheme 4-2**). The activation temperature was determined by TGA curve. Powder sample of Kgm-OEt shows the weight loss corresponding to the removal of the guest molecules at 80 ℃ and maintains its stability up to 300 ℃ (Figure. S8). Thus, as-prepared Kgm-OEt membranes were activated by N_2 sweeping at 100 ℃ prior to gas permeation experiments. Before measurement, the membrane was activated at 100 ℃ for 5 h in a N_2 gas stream. The volumetric flow rate and pressure drop was controlled by a microtrac-MRB BELCAT II. For the single gas measurements, the flow rate of the feed gas was set to 10 mL min^{-1}. For the mixed gas permeation measurement, a 1:1 mixture of gas was applied to the feed side of the membrane, and the feed flow rate was kept constant at 20 mL min^{-1} (10 mL min^{-1} for each gas). The permeate side was swept with He at 2 mL min^{-1}. The difference in the pressures of the feed and permeate side was kept constant at 10 kPa. The permeate gas was analyzed by an online gas chromatograph (Shimadzu Tracera BID-2010 Plus) using a molecular sieve capillary column. H_2 permeance of the unmodified Al_2O_3 substrate was ca. 1.8×10^{-6} mol m^{-2} s^{-1} Pa^{-1} at 25 ℃. The separation factor $\alpha_{i,j}$ of a binary mixture is defined as the ratio of the molar fractions X of the

component (i, j) in the permeate divided by the ratio of the molar fractions Y of (i, j) in the feed. The formula is shown below:

$$\alpha_{i,j} = \frac{X_i/X_j}{Y_i/Y_j}$$

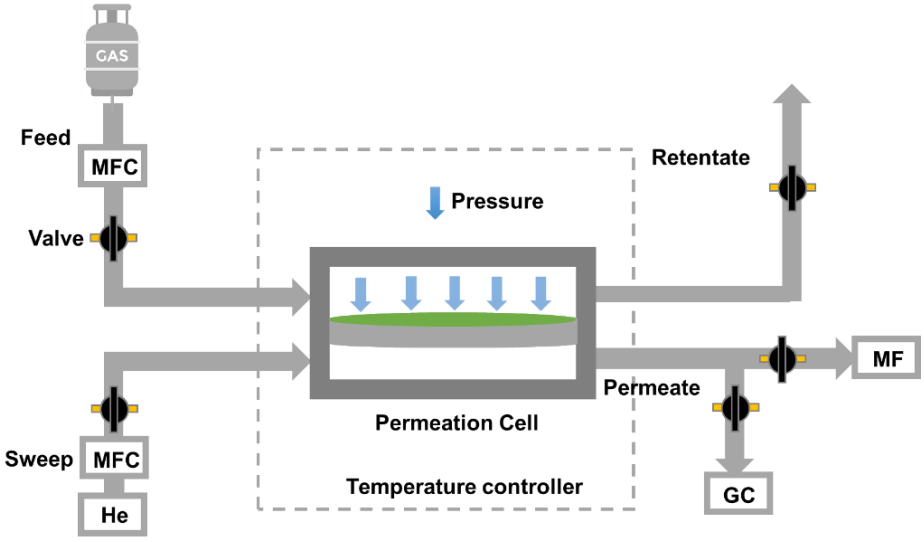

Scheme 4-2. Schematic image of the measurement setup for gas permeation experiment. MFC: mass flow controller. GC: gas chromatograph. MF: mass flow meter.

4-3. Results and discussion

Preparation of Kgm-OEt seed layer

The LBL method was applied to synthesize Kgm-OEt seed layer. Firstly, a layer of APTEs was deposited on an Al_2O_3 substrate through the reaction of ethoxysilane of APTEs and hydroxyl groups on the surface of Al_2O_3. Secondly, the seed layer was constructed by soaking the substrate into the solutions of H_2OEt-ipa and $Cu(NO_3)_2$ repeatedly. After the first seeding cycle, strong XRD peaks indicate the formation of Kgm-OEt crystals on the APTEs-modified substrate, while the weak XRD peaks suggest that almost no crystals were formed on the bare Al_2O_3 substrate (**Figure 4-1**). In addition, SEM images show that MOF crystals can grow on the surface of APTEs-modified substrate, while only the substrate surface is seen on the bare Al_2O_3 substrate (**Figure 4-**

2.). Optical images of the substrate also show that the color of the seed layer from the APTEs-modified substrate was green which was far deeper than that from the bare substrate (**Figure 4-3.**). These results indicate that APTEs modification promoted the growth rate of Kgm-OEt.

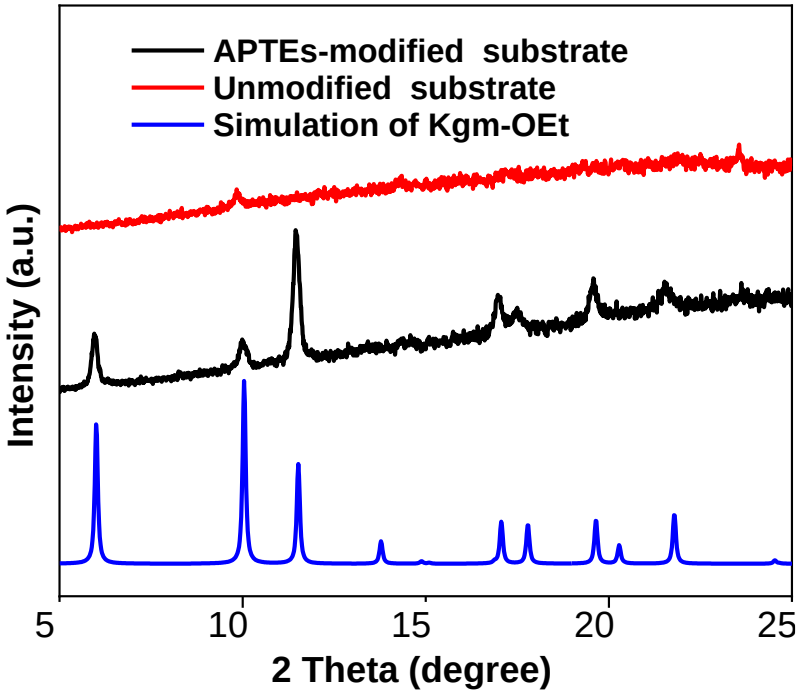

Figure 4-1. (a) XRD patterns of the seed layer after 1 cycle for the unmodified substrate and APTEs-modified substrate. (b) XRD patterns of the membrane with different cycle times.

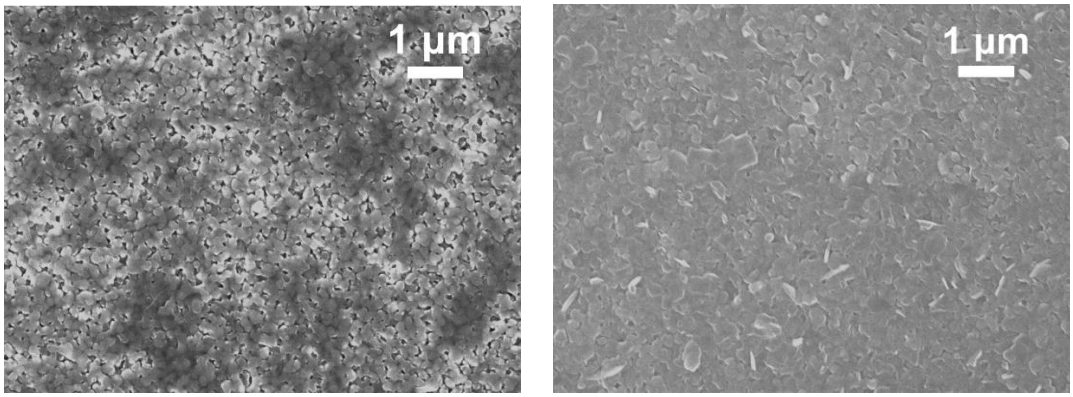

Figure 4-2. SEM images of the top view of seeded support after one cycle. Left: unmodified Al_2O_3 substrate. Right: APTEs modified Al_2O_3 substrate.

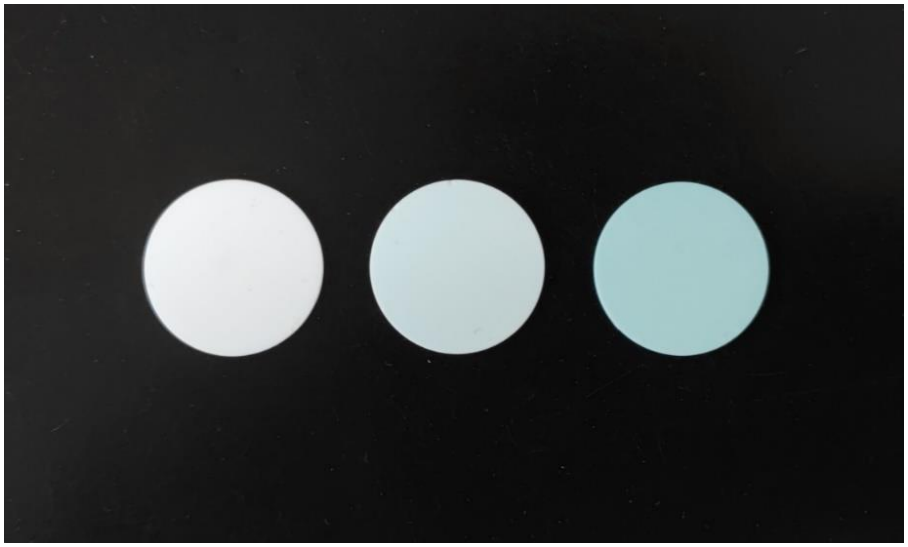

Figure 4-3. Optical images of the Al_2O_3 substrates. Left: unmodified Al_2O_3 substrate. Middle: unmodified Al_2O_3 substrate after one LBL cycle. Right: APTEs-modified Al_2O_3 substrate after one LBL cycle.

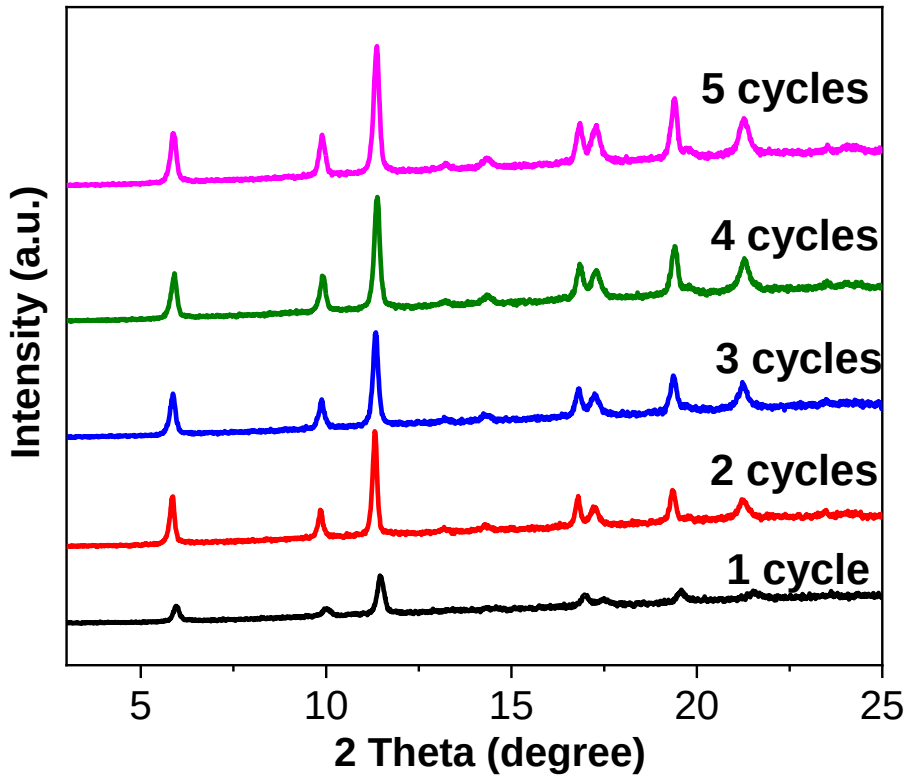

Figure 4-4. XRD patterns of the seed layer with different cycle times.

As the seeding cycle times increased, the intensity of XRD peaks in APTEs-modified Al_2O_3 substrate increased (**Figure 4-4**), indicating that denser Kgm-OEt seed layer was fabricated by LBL cycles. The intensity of XRD peaks was almost unchanged between four and five LBL cycles, and the SEM image shows that the seed layer completely covered the APTEs-modified substrate, thus four cycles can be enough for the deposition of the seed layer. In contrast, uncovered Al_2O_3 is still visible on the bare substrates even after seeding for four cycles (**Figure 4-5**). Notably, APTEs modification not only improves the growth of Kgm-OEt, but also results in the generation of particles with smaller sizes than those on bare substrate (400 nm and 1.2 μm, respectively, Figure **Figure 4-6**). The nucleation rate on the APTES-modified substrate might be faster than that on the unmodified one due to the higher density of ligand on the surface by $-NH_2$ groups, which may lead to the formation of smaller particles on the APTES-modified substrate. [28,29] The smaller particle size of the seed layer would be advantageous to form a continuous MOF membrane after the secondary growth, while larger particles tend to produce binary gaps between particles.

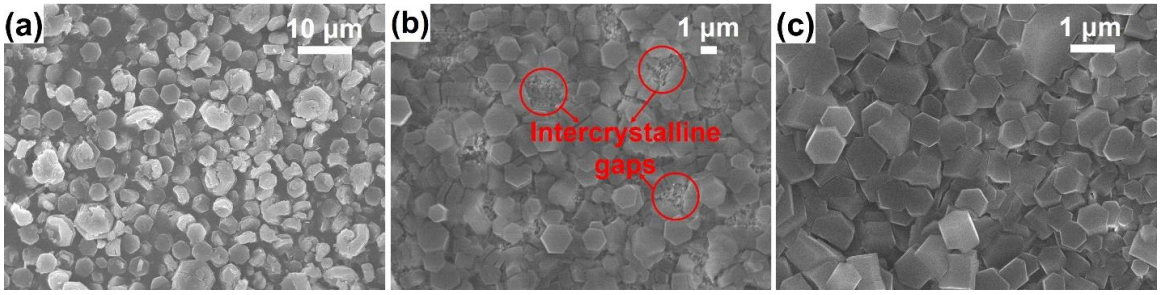

Figure 4-5. SEM images of Kgm-OEt crystals of (a) powder sample and seed layer on (b) bare and (c) APTEs-modified Al_2O_3 substrate.

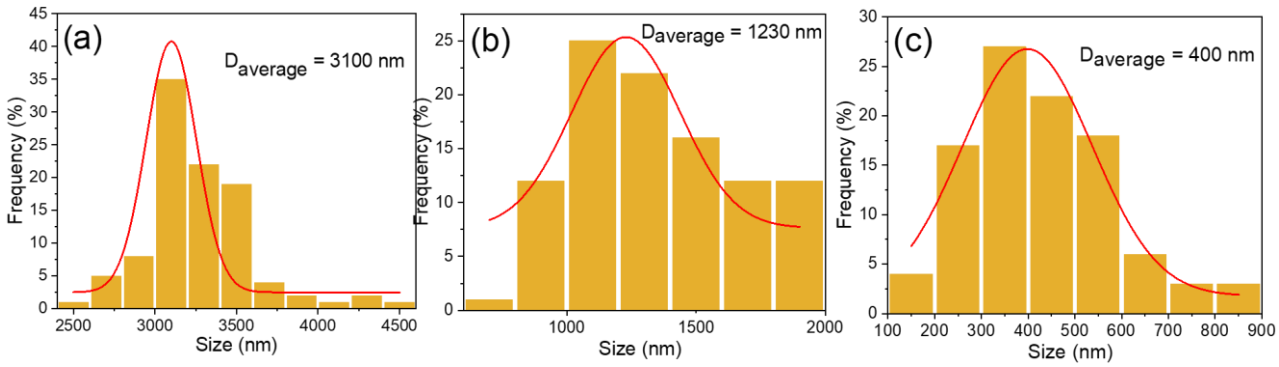

Figure 4-6. Particle size distribution of (a) powder sample, (b) seed in unmodified substrate and (c) seed in APTEs-modified substrate.

Preparation of Kgm-OEt membrane

Kgm-OEt membrane was grown from the seed layer by the secondary growth at room temperature. Top view SEM image of the membrane on the bare substrate shows that the crystals are loosely packed and poorly intergrown (**Figure 4-7** (a)). The SEM cross-sectional images indicate that the thickness of the membrane prepared on the bare substrate was about 10 μm. The continuity of the membrane was relatively poor, and small gaps between MOF particles were observed (**Figure 4-7** (b)). On the other hand, the surface was densely covered with hexagonal plate crystals merged tightly with each other forming the intergrowth structure on the APTEs-modified substrate and the thickness of the membrane on APTEs-modified substrate was about 3 μm (**Figure 4-7** (c)-(d)), which was about 3 times thinner than that by bare substrate, and the membrane was grown very compact without observable gaps between the intercrystalline boundary. It should be noted that the 2D sheet MOF crystals on the bare substrate tend to grow nearly vertical to the substrate surface after the secondary growth. On the other hand, most hexagonal particles were parallel to the APTEs-modified substrate, which can be suitable for gas transportation.

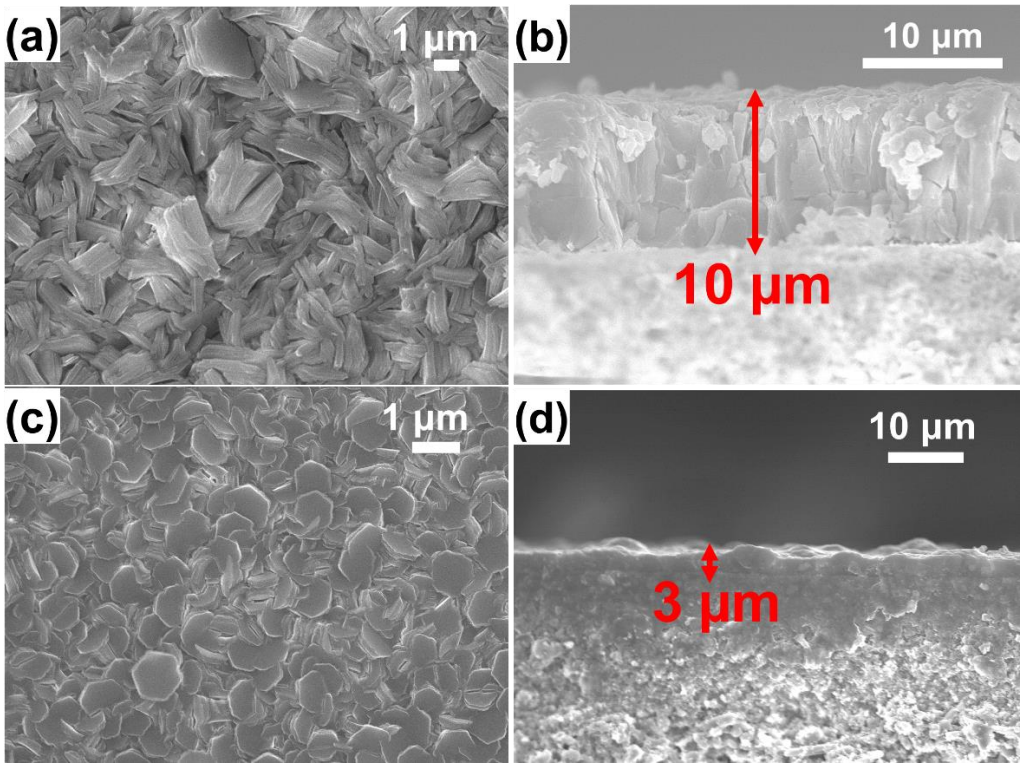

Figure 4-7. Top and cross-sectional view SEM images of Kgm-OEt membranes synthesized on the (a, b) bare and the (c, d) APTEs-modified substrate at different magnifications.

The difference in the growth direction of Kgm-OEt could be explained by the van der drift growth model.[30,31] The morphology of these Kgm-OEt crystals is a 2D hexagonal sheet structure with the order of crystal dimensions $L_b = L_a > L_c$, where L_i denotes the crystal length along the i axis (**Figure 4-8**). As the crystals grow larger, they collide with each other, and the orientation of the crystals change to get sufficient space for the crystal growth. On the bare substrate, the *a*- and *b*- axes growth of the crystal is faster than that of the *c*-axis, so the *a*- and *b*- axes are oriented to be perpendicular to the substrate. On the APTEs-modified Al_2O_3 substrate, as the particle sizes of the membrane were smaller, the collision of the crystals and the change of the crystal growth direction were greatly suppressed.

Figure 4-9 (a) shows the XRD patterns of the simulation of Kgm-OEt, powder, seed layer, membranes on bare and APTEs-modified substrate. All of the peak positions of membrane samples well match with the simulation, indicating the no impure phase. To analyze the orientation of the membranes, we compared the XRD of the membranes on APTEs-modified and unmodified substrate (**Figure 4-10**). **Figure 4-9** (b) shows the crystal plane of Kgm-OEt. The (001) plane is parallel to the hexagonal crystal. The 001 peak of membrane on unmodified substrate is almost absent, indicating the crystal orientation vertical to the hexagonal plane. For the membrane on APTEs-modified substrate, the 001 peak is clearly visible, indicating that the vertical growth is suppressed. EDX mapping analysis further revealed the boundary between the Kgm-OEt membrane and the APTEs-modified Al_2O_3 substrate (**Figure 4-11** (a), (b)). Optical images of the APTEs-modified Al_2O_3 substrate, seed layer and membrane also showed in **Figure 4-11** (c). In short, we tuned microstructure by deposition of amino groups on Al_2O_3 substrate and successfully prepared high-density and continuous Kgm-OEt membrane.

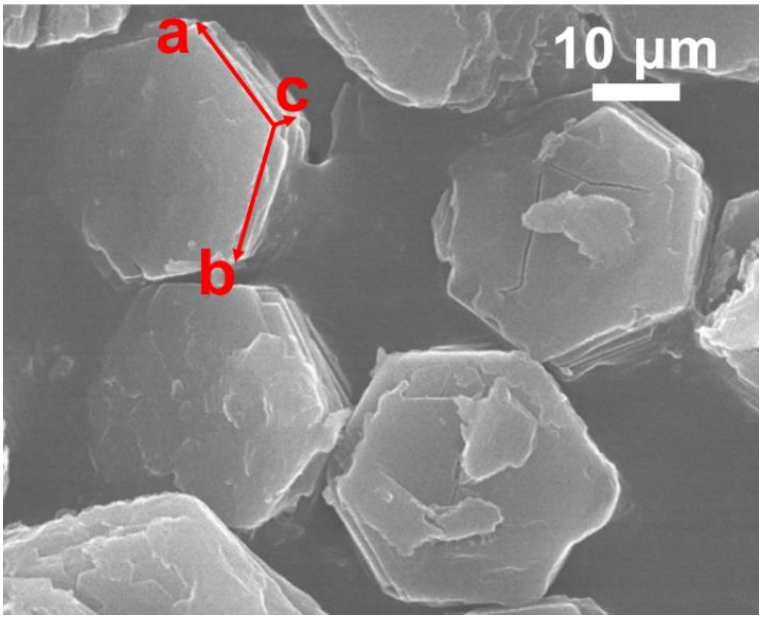

Figure 4-8. SEM image of Kgm-OEt crystals.

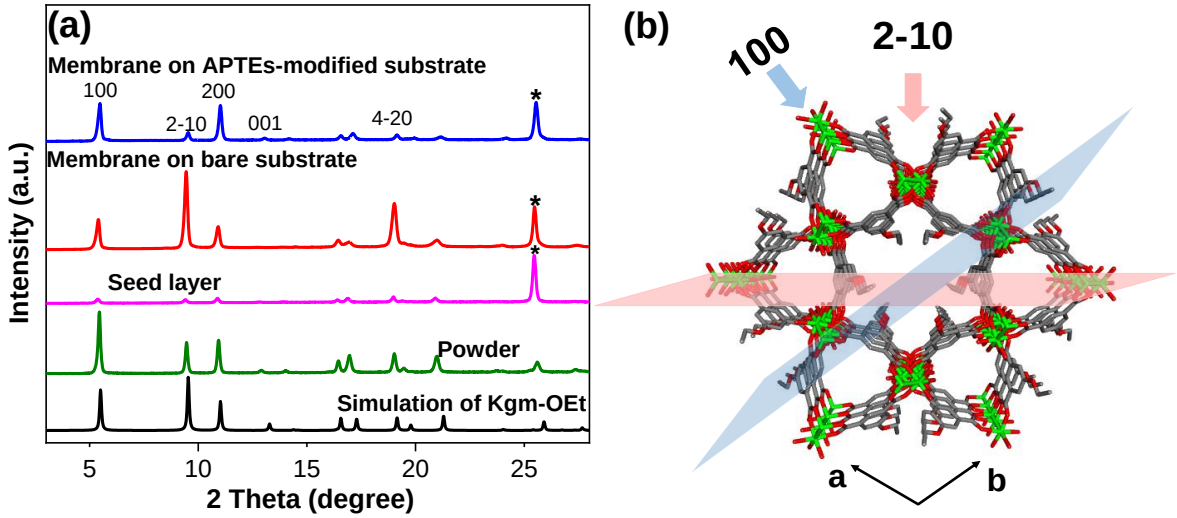

Figure 4-9. (a) XRD patterns of the simulation of Kgm-OEt, powder, seed layer and membranes. *: Al_2O_3 substrate. (b) Crystal plane of Kgm-OEt.

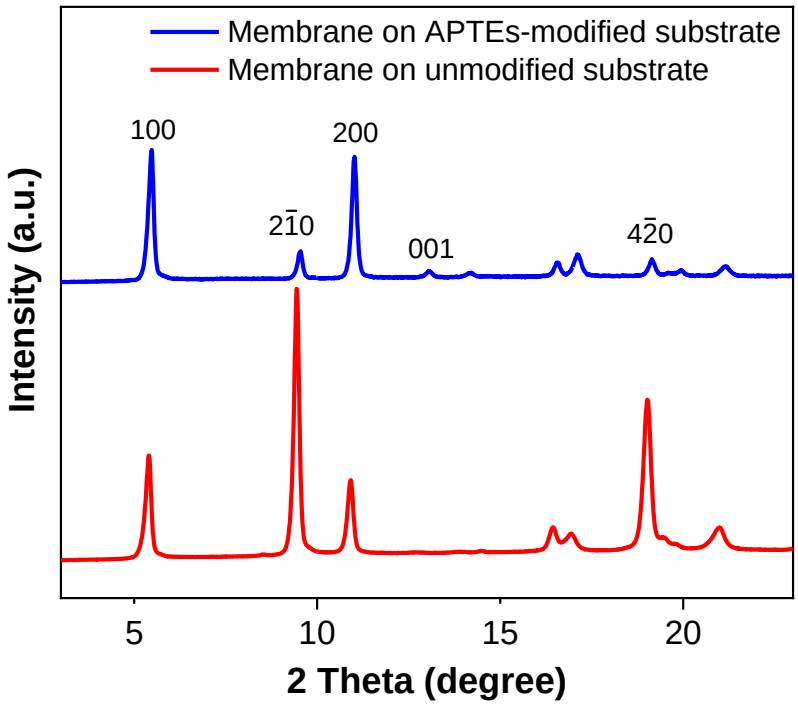

Figure 4-11. XRD patterns of membranes on APTEs-modified and unmodified substrate.

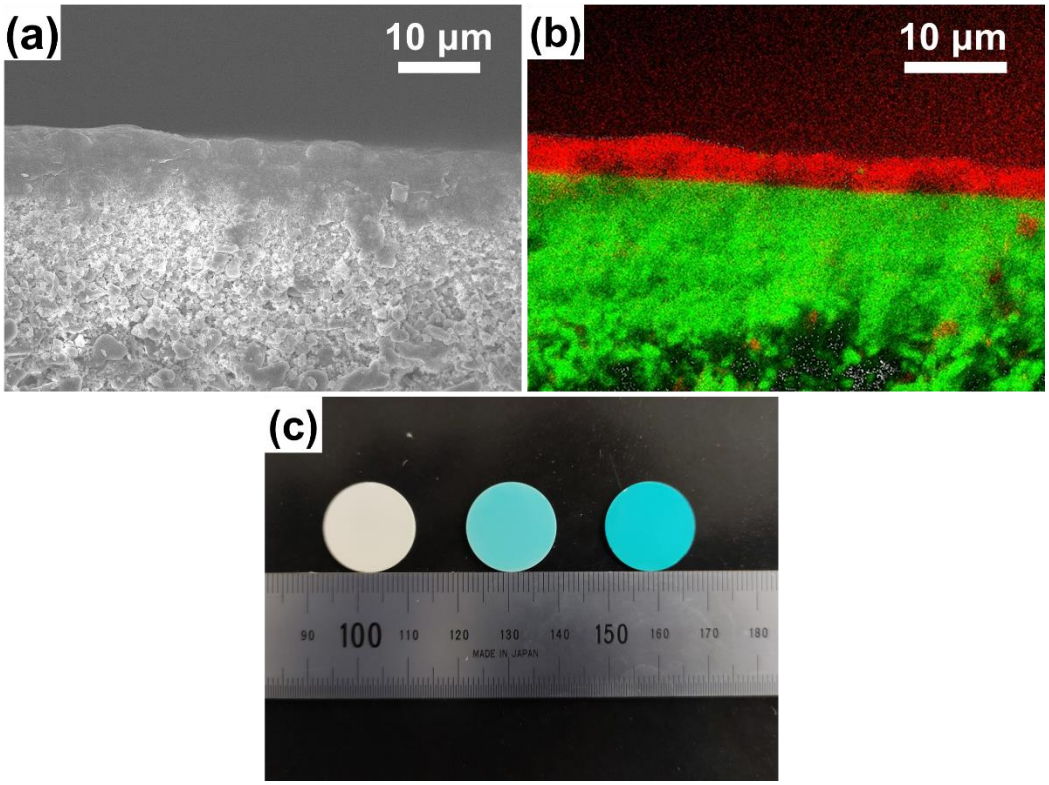

Figure 4-11. (a) SEM, (b) EDX mapping (Green: Al, red: Cu) of membrane on the APTEs-modified substrate. (c) Photograph of the APTEs-modified Al_2O_3 substrate: left, Kgm-OEt seed layer: middle and Kgm-OEt membrane: right.

Permeation measurements

The single gas permeances of the Kgm-OEt membrane were measured at 10 kPa differential pressure and 25 ℃ using a Wicke-Kallenbach setup. As-prepared Kgm-OEt membranes were activated by N_2 sweeping at 100 ℃ prior to gas permeation experiments. The activation temperature was determined by TGA curve (**Figure 4-12**). The results are shown with the kinetic diameter of the gas molecules (**Figure 4-13** (a)). The membrane exhibits the highest permeance for H_2 (2.73×10^{-8} mol m^{-2} s^{-1} Pa^{-1}), and the permeances decrease with an order of $H_2 > CO_2 > N_2 > CH_4 > C_2H_4$, which corresponds to their kinetic diameters except for CO_2. The calculated ideal selectivities for H_2/CO_2, H_2/N_2, H_2/CH_4 and H_2/C_2H_4 are 5.2, 4.4 ,4.6 and 6.5, respectively. The experimental separation factors for H_2 over CO_2, CH_4, N_2 and C_2H_4 obtained by 1:1 binary-gas permeation tests are 5.0,

4.1, 4.4, and 6.2. All of the separation factors surpass Knudsen constant and C_2H_4 molecules have the lowest permeability, indicative of the sieving effect of the membrane. The stronger CO_2 adsorption of Kgm-OEt (**Figure 4-14**) can reduce the CO_2 mobility so that the membrane shows lower permeance of CO_2 than N_2 and CH_4.[32,33] H_2/CO_2 selectivity is also higher than those of polymer membranes based on Robeson (2008) and Robeson (1991) (**Figure 4-13** (b)).[34] It is also noted that the long-term stability test showed that the gas permeance and the H_2/CO_2, H_2/N_2, H_2/CH_4 and H_2/C_2H_4 selectivity of the Kgm-OEt membrane were stable for 10 h at 25 ℃, indicating the high durability of the membrane (**Figure 4-15**).

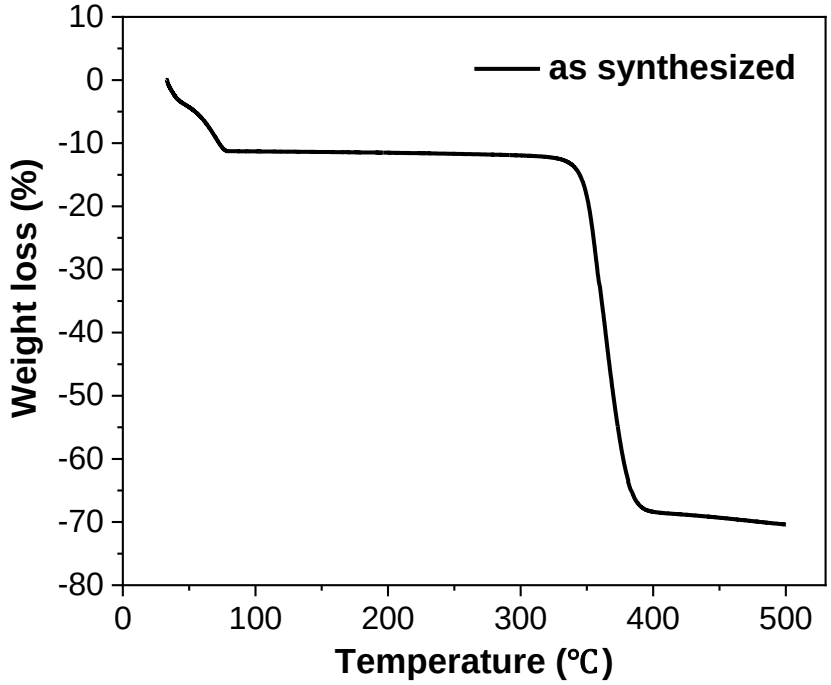

Figure 4-12. Thermogravimetric analysis (TGA) curve of Kgm-OEt powder samples.

As a comparison, we tested the binary-gas permeation of Kgm-OEt membrane prepared on the bare Al_2O_3 substrate (**Table 4-1**). The separation factor for H_2 and other gases were lower than 2. This value is much lower than Knudsen constant, the reason can be attributed to the existence of pinholes or poor intergrowth of particles. The results

clearly illustrate that APTEs promotes the growth of Kgm-OEt on the Al_2O_3 substrate to form a defect-free membrane.

Table 4-1. mixture gas permeances (mol m^{-2} s^{-1} pa^{-1}) and separation factors for the Kgm-OEt membrane in unmodified Al_2O_3 support at 25 °C and a pressure drop of 10 kpa

Gas	Separation factor	Knudsen constant
H_2/CO_2	1.76	4.7
H_2/N_2	1.54	3.7
H_2/CH_4	1.28	2.8
H_2/C_2H_4	1.56	3.7

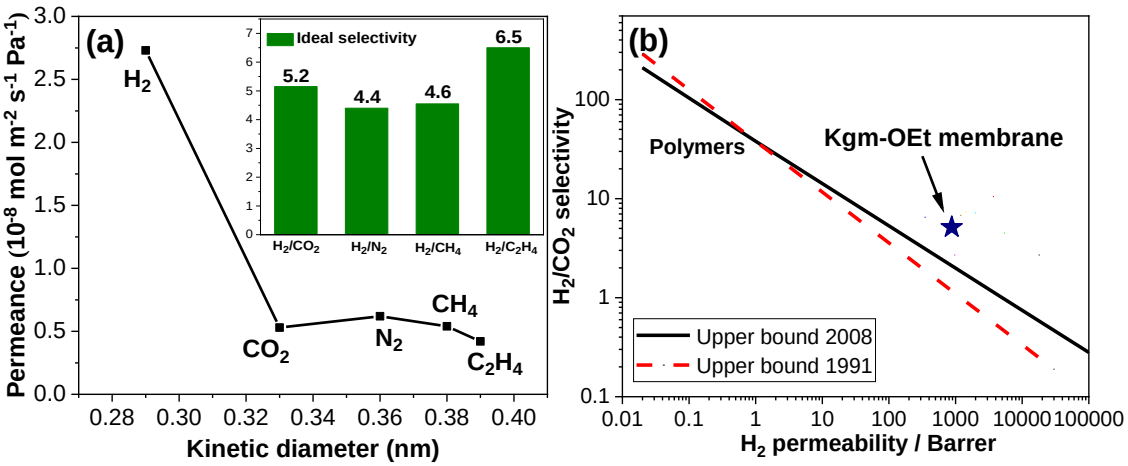

Figure 4-13. (a) Single gas permeances on the Kgm-OEt membranes at 25 °C and 10 kPa with the kinetic diameters. (b) H_2/CO_2 selectivity versus H_2 permeability for Kgm-OEt membrane at 25 °C and 10 kPa, compared with the upper bound lines for polymeric membranes are based on Robeson (2008) and Robeson (1991).

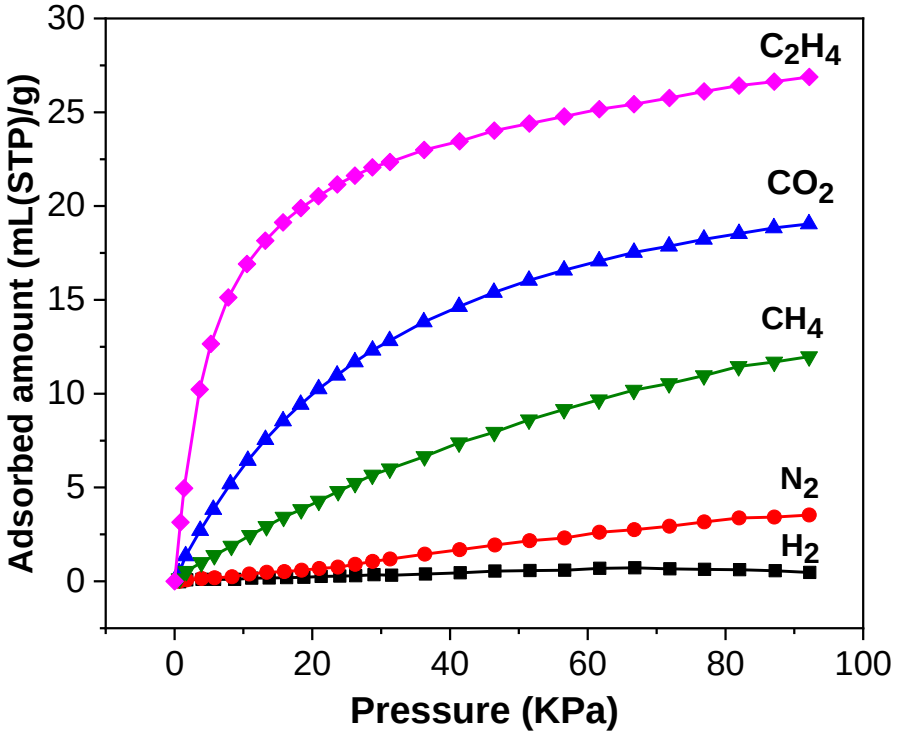

Figure 4-14. Adsorption isotherms of H_2, CO_2, N_2, CH_4, C_2H_4 for the Kgm-OEt powder sample at 25 °C

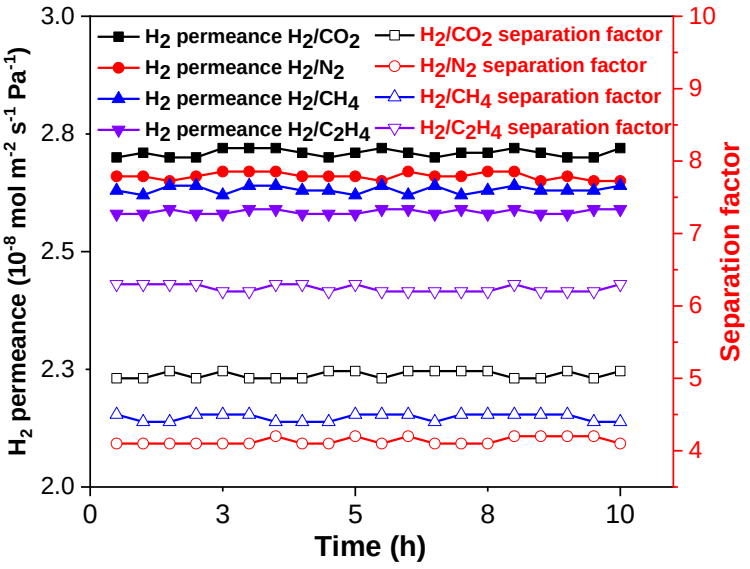

Figure 4-15. H_2 permeances and separation factors by binary gas mixtures of H_2/CO_2, H_2/N_2, H_2/CH_4 and H_2/C_2H_4 systems of Kgm-OEt membrane as a function of time at 25 ℃ with a pressure drop of 10 kpa.

4-4. Conclusions

In summary, a continuous and defect-free MOF Kgm-OEt membrane has been successfully synthesized by the secondary growth approach on the APTEs-modified porous Al_2O_3 substrate surface. We applied an LBL method to construct the seed layer for this kagomé-type of MOF. It is shown that APTEs-modified Al_2O_3 substrate can form a fully covered seed layer. The particle size of the seed is smaller on the APTEs-modified substrate than the bare substrate. The microstructure of the membrane grew in the APTEs-modified substrate is greatly improved compared with the bare substrate. Our work would give a convenient method for the preparation of various types of MOF membranes, especially those based on metal carboxylates, which cause defects by the ordinary methods.

4-5. References

1 H. Furukawa, M. A. Miller, O. M. Yaghi, *J. Mater. Chem.*, 2007, **17**, 3197-3204.

2 S. Kusaka, A. Kiyose, H. Sato, Y. Hijikata, A. Hori, Y. Ma, R. Matsuda, *J. Am. Chem. Soc.*, 2019, **141**, 15742-15746.

3 L. Li, R. Lin, R. Krishna, H. Li, S. Xiang, H. Wu, J. Li, W. Zhou, B. Chen, *Science*, 2018, **362**, 443-446.

4 H. Sato, W. Kosaka, R. Matsuda, A. Hori, Y. Hijikata, R. V. Belosludov, S. Sakaki, M. Takata, S. Kitagawa, *Science*, 2014, **343**, 167-170.

5 J. S. Seo, D. Whang, H. Lee, S.I. Jun, J. Oh, Y. J. Jeon, K. Kim, *Nature*, 2000, **404**, 982-986.

6 P. Horcajada, C. Serre, M. Vallet-Reg í, M. Sebban, F. Taulelle, G. F érey, *Angew. Chem. Int. Ed.*, 2006, **45**, 5974-5978.

7 Y. Ma, R. Matsuda, H. Sato, Y. Hijikata, L. Li, S. Kusaka, M. Foo, F. Xue, G. Akiyama, R. Yuan, S. Kitagawa, *J. Am. Chem. Soc.*, 2015, **50**, 15825-15832.

8 G. E. Cmarik, M. Kim, S. M. Cohen, K. S. Walton, *Langmuir*. **2012**, *28*, 15606-15613.

9 Y. Tan, Y. He, J. Zhang, *Inorg. Chem.*, 2012, **51**, 9649-9654.

10 S. R. Venna, M. A. Carreon, *J. Am. Chem.* Soc., 2010, **132**, 76-78.

11 W. Wang, X. Dong, J. Nan, W. Jin, Z. Hu, Y. Chen, J. Jiang, *Chem. Commun.*, 2012, **48**, 7022–7024.

12 S. Jiang, X. Shi, F. Sun, G. Zhu, *Chem. Asian J.*, 2020, **15**, 2371-2378.

13 Y. Liu, Z. Ng, E. A. Khan, H.-K. Jeong, C.-b. Ching, Z. Lai, *Microporous Mesoporous Mater.*, 2009, **118**, 296-301.

14 A. Huang, W. Dou, J. Caro, *J. Am. Chem. Soc.*, 2010, **132**, 15562-15564.

15 S. Tanaka, K. Okubo, K. Kida, M. Sugita, T. Takewaki, *J. Membr. Sci.*, 2017, **544**, 306-311.

16 H. Yin, J.Wang, Z.Xie, J.Yang, J.Bai, J.Lu, Y. Zhang, D. Yin, J. Lin, *Chem. Commun.*, 2014, **50**, 3699-3701.

17 S. Zhou, X. Zou, F. Sun, F. Zhang, S. H. Zhao, T. Schiestel, G. Zhu, *J. Mater. Chem.*, 2012, **22**, 10322-10328.

18 Y. Sun, Y. Liu, J. Caro, X. Guo, C. Song, Y. Liu, *Angew. Chem. Int. Ed.*, 2018, **130**, 16320-16325.

19 F. Zhang, X. Zou, X. Gao, S. Fan, F. Sun, H. Ren, G. Zhu, *Adv. Funct. Mater.*, 2012, **22**, 3583-3590.

20 B. Ghalei, K. Wakimoto, C. Y. Wu, A. P. Isfahani, T. Yamamoto, K. Sakurai,M. Higuchi, B. K. Chang, S. Kitagawa, E. Sivaniah, *Angew. Chem. Int. Ed.*, 2019, **58**, 19034–19040.

21 L. Wan, C. Zhou, K. Xu, B. Feng, A. Huang, *Microporous Mesoporous Mater.*, 2017, **252**, 207–213.

22 B. Liu, O. Shekhah, HK. Arslan, J. Liu, C. Wöll, R. A. Fischer, *Angew. Chem. Int. Ed.*, 2012, **51**, 807-810.

23 A. S. Münch, J. Seidel, A. Obst, E. Weber, F. O. R. L. Mertens, *Chem. Eur. J.*, 2011, **17**, 10958–10964.

24 O. Shekhah, L. Fu, R. Sougrat, Y. Belmabkhout, A. J. Cairns, E. P.Giannelis, M. Eddaoudi, *Chem. Commun.*, 2012, **48**, 11434–11436.

25 B. Ghalei, K. Wakimoto, CY. Wu, AP. Isfahani, T. Yamamoto, K. Sakurai, M. Higuchi, BK.Chang, S. Kitagawa, E. Sivaniah, *Angew. Chem. Int. Ed.*, 2019, **58**, 19034-19040.

26 O. Barreda, G. Bannwart, G. P. A. Yap, E. D. Bloch, *ACS Appl. Mater.Interfaces*, 2018, **10**, 11420–11424.

27 F. L. N. McHugh, M. J. McPherson, L. J. McCormick, S. A. Morris, P. S.Wheatley, S. J. Teat, D. McKay, D. M. Dawson, C. E. F. Sansome, S. E.Ashbrook, C. A. Stone, M. W. Smith, R. E. Morris, *Nat. Chem.*, 2018, **10**,1096–1102.

28 S. H. Jhung, T. Jin, Y. K. Hwang, J. S. Chang, *Chem. Eur. J.*, 2007, **13**, 4410–4417

29 X. Wu, Z. Bao, B. Yuan, J. Wang, Y. Sun, H. Luo, S. Deng, *Microporous Mesoporous Mater.*, 2013, **180**, 114–122.

30 Z. Zhong, J. Yao, R. Chen, Z. Low, M. He, J. Z. Liu, H. Wang, *J. Mater.Chem. A*, 2015, **3**, 15715–15722.

31 A. J. Bons, P. D. Bons, *Microporous Mesoporous Mater.*, 2003, **62**, 9–16.

32 N. Wang, A. Mundstock, Y. Liu, A. Huang, J. Caro, *Chem. Eng. Sci.*, 2015,**124**, 27–36.

33 C. Liu, Y. Jiang, C. Zhou, J. Caro, A. Huang, *J. Mater. Chem. A*, 2018, **6**, 24949–24955.

34 L. M. Robeson, *J. Membr. Sci.*, 2008, **320**, 390–400

Chapter 5

Heterobilayer membranes from isostructural MOFs for efficient CO_2 separation

5-1. Introduction

The content of carbon dioxide (CO_2) in the atmosphere is sharply rising year by year over the past few centuries, which brings serious challenges to the survival and development of human society since CO_2 is the key greenhouse gas that drives global climate change. [1-2] Therefore, it is very important to capture, purify, and utilize CO_2. [3-5] Presently, primary carbon capture and sequestration methods are chemical absorptions in solvents such as amines or ionic liquids; [6-8] however, corrosion of the device, absorbent cost, and high energy for CO_2 recovery are frequent disadvantages. [9-11] Membrane separation has been rapidly developed in recent decades because of its lower energy consumption, environmental-friendliness, and easy operation. [12-14] Polymeric membranes have dominated the membrane market so far. However, polymeric membranes can suffer from low thermal stability, a short lifetime, and a permeability/selectivity tradeoff. [15-17] Therefore, for future CO_2 separation, membranes based on materials with permanent porosity, robust frameworks, and rational pore aperture are more promising.

Metal-organic frameworks (MOFs) are a new class of materials constructed by bridging metal ions or clusters with organic linkers to form highly regular porous networks. [18-20] They attract much attention because of their regular structures, high surface areas, tunable pore sizes at the atomic level, and so on. [21-23] MOF materials have offered tremendous applications toward high-performance membranes, including mixed matrix membranes (MMMs), composites membranes, and MOF membranes. [24-27] Some researches suggest that higher CO_2 adsorption capacity and selectivity of MOFs are beneficial for the CO_2 permselectivity. For example, CAU-1 and ZIF-69 membranes were reported to exhibit high CO_2 permselectivity over N_2 and CH_4 due to their strong interaction with CO_2. [28,29] In addition, Liu et al. [30] reported that a defect-engineered UiO-66 membrane having higher CO_2/N_2 adsorption selectivity showed the superior CO_2/N_2 separation performance.

Although many promising MOF candidates with preferential CO_2 adsorption for CO_2 separation membranes should have been developed, most studies focus on benchmark MOFs such as ZIFs, UiO, and MIL series. [31-34] One possible reason for the limited examples of MOFs used in CO_2 separation membranes might be due to the difficulty in membrane fabrication. When metal ions and ligands are changed to tune the adsorption property of MOFs, crystal growth processes of MOFs can also be affected, resulting in the formation of a poorly intergrown, low-quality crystalline film. [35, 36] The development of a new membrane fabrication technique will broaden the applicability of MOFs toward membranes.

In this study, we demonstrate how to make a dense MOF membrane using a heterobilayer membrane strategy in which a MOF seed layer was first immobilized on the substrate surface, then the epitaxial secondary growth of another isostructural MOF membrane layer was created. This heterobilayer membrane showed good homogeneity and effective CO_2 separation, even though defectless membranes could not be obtained when the membrane was made from one of each MOF. Our result would provide a new concept to design separation membranes by combining the advantages of different isostructural MOFs.

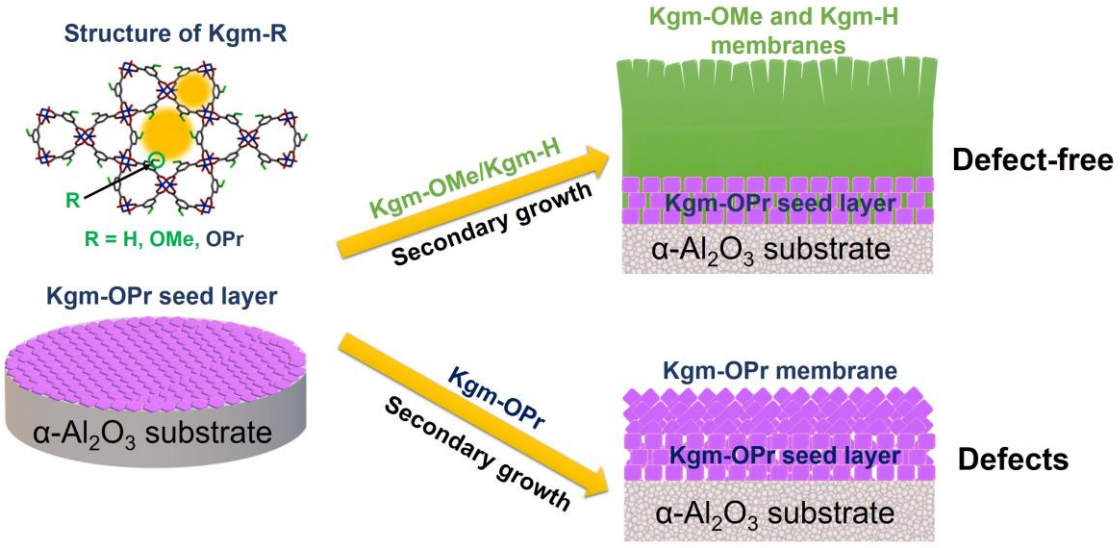

Grafic Abstract

5-2. Experimental

Chemicals

All commercially available chemicals were purchased and used as received: $Cu(NO_3)_2 \cdot 3H_2O$ (Wako,99%), methanol (Wako, 99.8%). isophthalic acid (TCI, 99%), dimethyl 5-hydroxyisophthalate (TCI, 98%), 5-methoxyisophthalic acid (TCI, 98%), propyl iodide (TCI, 99%), potassium carbonate (TCI, 99%), acetone (Nacalai, 99.5%), ethyl acetate (Nacalai, 99%), hexane (Nacalai, 95%), sodium hydroxide (TCI, 97%), hydrochloric acid (Nacalai, 36%~38%), (3-aminopropyl) triethoxysilane (Aldrich, 99%). 5-Propoxyisophthalic acid was synthesized by the eported method.[34] Porous α-Al_2O_3 disks substrates (18 mm in diameter, 1.0 mm in thickness, 70 nm particles in the top layer) were purchaced from Fraunhofer Institute IKTS, former HITK/Inocermic, Hermsdorf, Germany.

APTEs modification on the Al_2O_3 support surface

Porous Al_2O_3 substrates were first activated by immersing in hydrochloric acid (2 M) for 24 h. The Al_2O_3 substrates were then heated in a solution of 0.06 mL (3-aminopropyl)triethoxysilane (APTEs) in 20 mL toluene for 3 h at 120 ℃ under argon to deposit amino monolayer on the substrate surface. Following that, the substrate was washed with methanol and dried in a vacuum for 4 h.

Preparation of Kgm-OPr seed layer

The layer-by-layer (LBL) technique was used to create the Kgm-OPr seed layer. The Al_2O_3 modified substrates were first immersed in a 50.0 mM 5-propoxyisophthalic acid methanol solution for 20 min and then in a 50.0 mM $Cu(NO_3)_2 \cdot 3H_2O$ methanol solution for 20 min at room temperature. The substrates were washed with methanol at each step. The entire procedure was repeated four times to form a seed layer. After the seed layer formation, the substrates were dried in a vacuum at 80°C for 3 h.

Membrane preparation

The Kgm-OPr, Kgm-OMe, and Kgm-H membranes were prepared by a secondary growth method (**Scheme 5-1**). The synthesis solutions for Kgm-OPr, Kgm-OMe, or Kgm-H membranes were prepared by dissolving $Cu(NO_3)_2 \cdot 3H_2O$ (30 mg) and 5-propoxyisophthalic acid (28 mg), $Cu(NO_3)_2 \cdot 3H_2O$ (60 mg) and 5-methoxyisophthalic acid (49 mg) or $Cu(NO_3)_2 \cdot 3H_2O$ (60 mg) and isophthalic acid (42 mg), respectively, in a solution of pyridine (20 μL) and methanol (40 mL). The APTEs modified Al_2O_3 substrate was vertically placed into a beaker containing a synthesis solution. After several hours at room temperature, the substrate was removed and rinsed with methanol to remove the loose powder on the surface before being immersed in 50 mL methanol for 12 h, and stored in a vacuum for future use. The powder samples of each MOF were collected from the synthesis solutions to compare the crystal sizes of bulk powders with membranes.

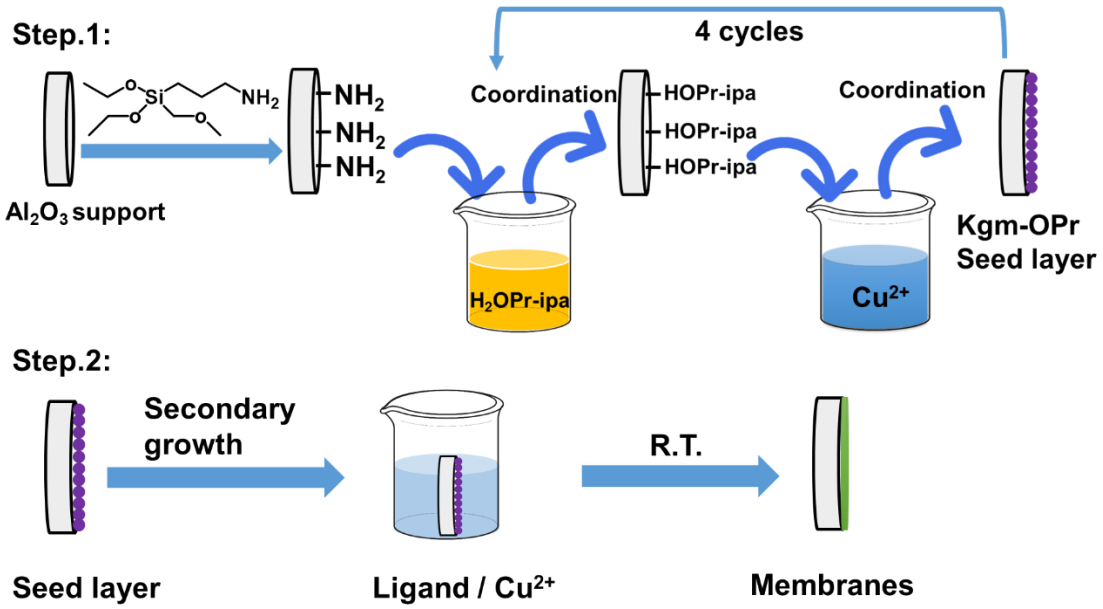

Scheme 5-1. Scheme of the preparation procedure of seed layer and membranes.

Characterization

X-ray diffraction (XRD) patterns of the MOF membranes and MOF powders were measured using a MiniFlex600 (Rigaku corp.) X-ray diffractometer with Cu *Kα* radiation. Field emission scanning electron microscope (FESEM) images were taken by a JED-

2300F (JEOL ltd.) with an acceleration voltage of 15 kV. Gas adsorption experiments were performed using a BELSorp-max (MicrotracBEL corp.) automated gas adsorption analyzer equipped with a cryostatic temperature controller. Samples were activated by heating at 120 °for 24 hours under dynamic vacuum before adsorption measurement.

Gas permeance measurement

The gas permeation measurements were performed on a Wicke–Kallenbach setup (**Scheme 5-2**). Before measurement, the membrane was activated at 100 ℃ for 5 h under a nitrogen gas stream. The volumetric flow rate was controlled by BELCAT II (MicrotracBEL corp.) equipped with mass flow controller and the pressure drop was controlled by pressure control valve. The feed flow rates for a single-gas measurement were set to 10 mL min^{-1}. The flow rates for the 1:1 mixed gas permeation measurement were set to 20 mL min^{-1} (10 mL min^{-1} each). The permeate side was swept with helium at 2 mL min^{-1}. The pressure difference was set at 10 kPa (the pressure for the feed side is 110 kPa and that for the sweep side is 100 kPa). An online gas chromatograph (Tracera BID-2010 Plus, Shimadzu corp.) with a molecular-sieve column was used to analyze the permeance. At room temperature, the H_2 permeance of the Al_2O_3 substrates was approximately 1.8×10^{-6} mol/m^2s Pa. The separation factor $\alpha_{i,j}$ of a binary mixture is defined as the ratio of the molar fractions X of component (i, j) in the permeate divided by the ratio of the molar fractions Y of (i, j) in the feed. The formula is shown below:

$$\boldsymbol{\alpha_{i,j} = \frac{X_i/X_j}{Y_i/Y_j}}$$

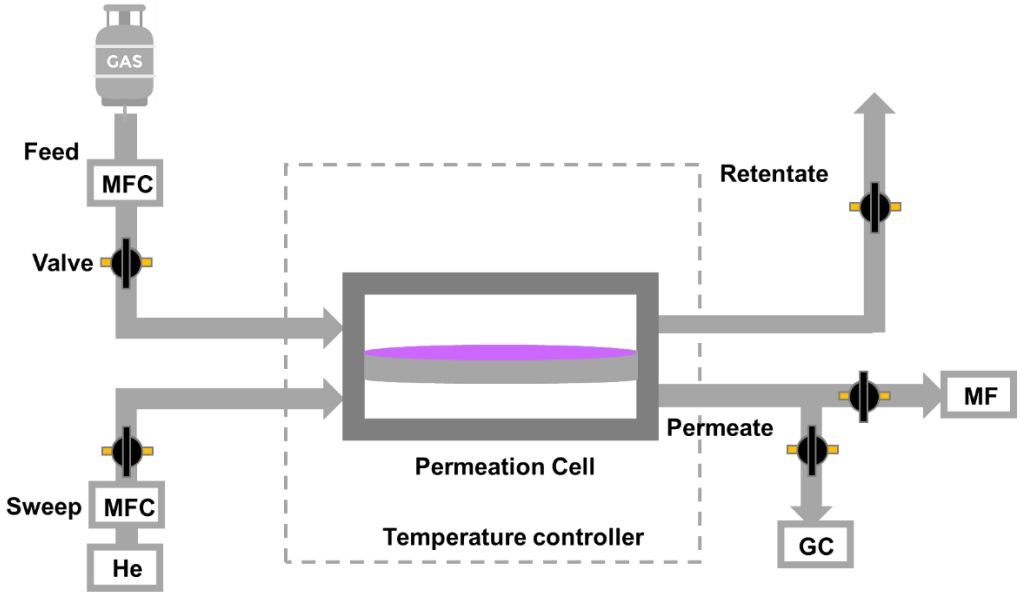

Scheme 5-2. Measurement equipment for gas permeation. MFC: mass flow controller. GC: gas chromatograph. MF: mass flow meter.

5-3. Results and discussion

Structure of Kgm-OPr, Kgm-OMe and Kgm-H and design strategy

Kgm-OPr ([Cu(OPr-ipa)], OPr-ipa = 5-Propoxyisophthalate), Kgm-OMe ([Cu(OMe-ipa)], OMe-ipa = 5-Methoxyisophthalate), and Kgm-H ([Cu(H-ipa)], H-ipa = Isophthalate) are a series of kagomé-type two-dimensional (2D) sheet structure MOFs. They are isostructural but have different pore aperture sizes. [37, 38] They have two types of one-dimensional (1D) pores. One is a triangular pore containing copper(II) paddle-wheel units coordinated by water molecules. Another pore has hexagonal geometry and all the alkoxy groups point toward the pore center, allowing the pore size to be adjusted by the functional groups on the 5-position of isophthalic acid (**Figure 5-1**). N_2 adsorption isotherms (**Figure 5-2**) at 77 K demonstrated the maximum adsorption amounts of 172, 77.7, and 28.9 mL(STP)/g for Kgm-H, Kgm-OMe, and Kgm-OPr at 80 kPa, respectively, indicating that the decrease in the pore volume depends on the substituent sizes. Table S1 summaries the surface areas and pore volumes of Kgm-H, Kgm-OMe, and Kgm-OPr, as

expected the surface area and pore volume follow the order of Kgm-H > Kgm-OMe > Kgm-OPr, which has been shown in the crystal structure. The simulated and observed powder XRD patterns (**Figure 5-3**) of the three MOFs showed characteristic peaks derived from 100, 2-10, and 200 reflections at the same 2theta values of 5.47º, 9.46º, and 10.97º, respectively, indicating that they have almost the same unit cells. The pore sizes of Kgm-OMe (4.8 Å) and Kgm-H (7.6 Å) after the removal of the coordinated water molecules [39] would show high CO_2 permselectivity based on the surface diffusion mechanism, as expected by the preferential CO_2 adsorption over N_2 and CH_4 (**Figure 5-4**(a) and (b)). On the other hand, Kgm-OPr, which has the small pore cross-section size (3.2 Å) and low adsorption capacities (**Figure 5-4**(c)) and is thought to be impermeable for gases larger than H_2, can well serve as the seed for the epitaxial membrane layer growth of Kgm-OMe and Kgm-H without affecting their permselectivity.

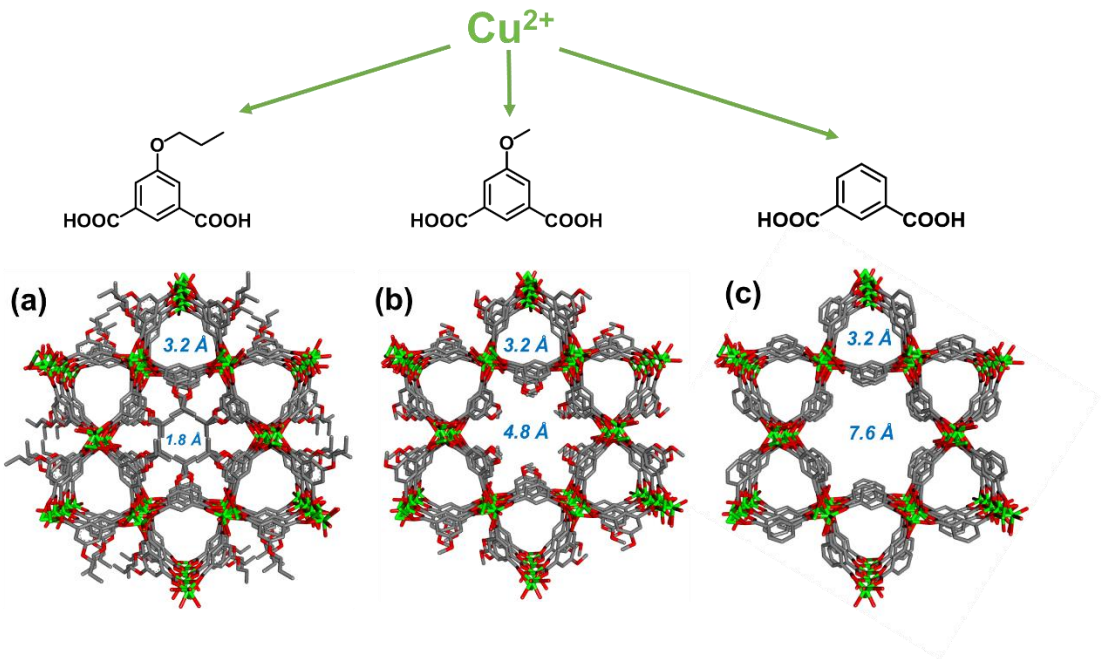

Figure 5-1. Structures of (a) Kgm-OPr, (b) Kgm-OMe and (c) Kgm-H. Atoms are colored as follows: Cu, green; O, red; C, gray; H is hidden.

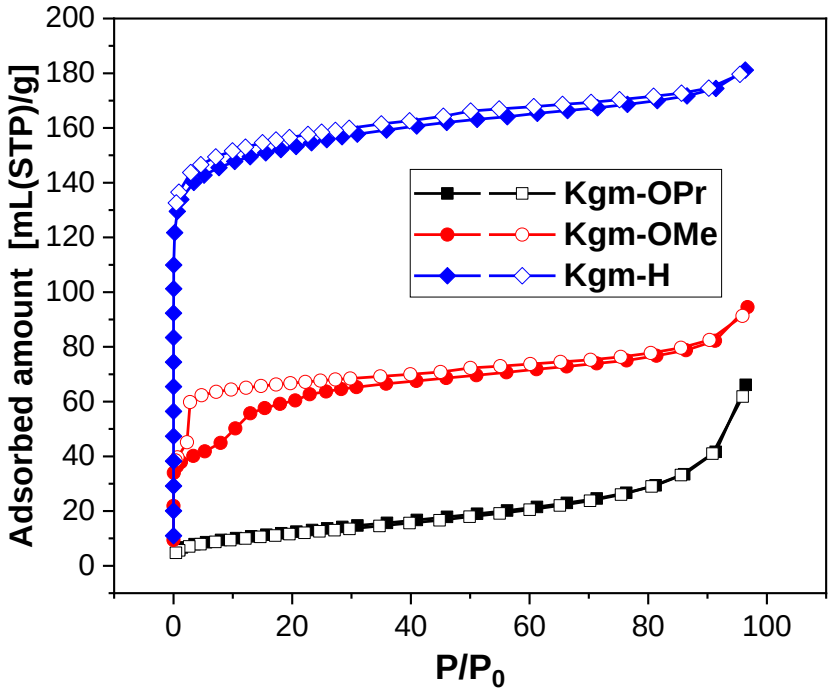

Figure 5-2. N_2 adsorption isotherms of Kgm-OPr, Kgm-OMe and Kgm-H at 77K.

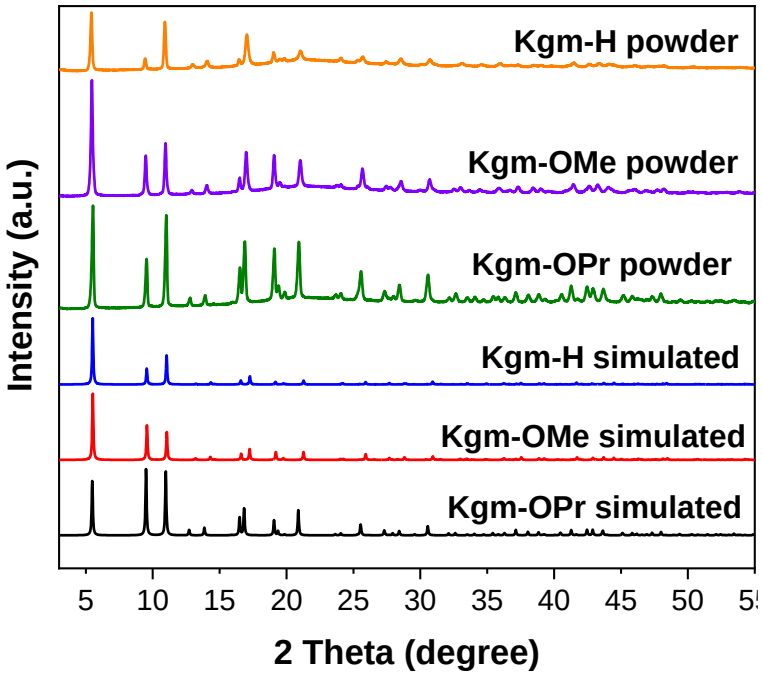

Figure 5-3. PXRD of Kgm-OPr, Kgm-OMe and Kgm-H simulated and powder samples.

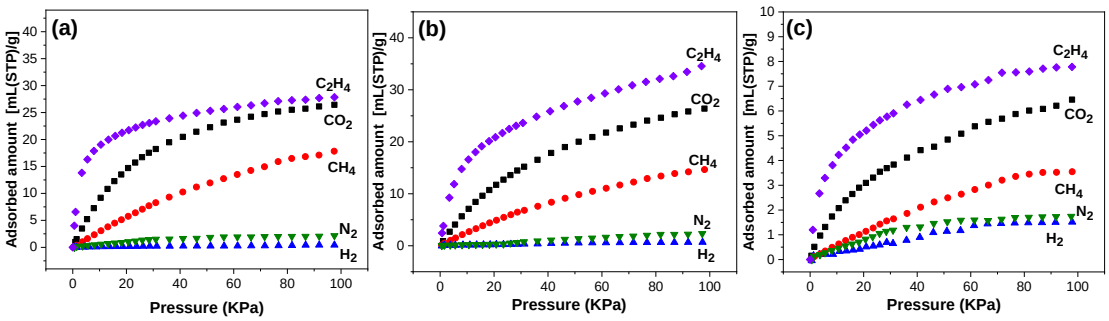

Figure 5-4. Gas adsorption isotherms of Kgm-OPr at 25 °C.

Preparation of Kgm-OPr seed layer

To create kagomé-MOF-based membranes, first, we modified Al_2O_3 substrates with APTEs as the covalent linker to improve the linkage between MOFs and substrates. Furthermore, the LBL method was used to prepare a seed layer of Kgm-OPr. A modified substrate was soaked in metal and ligand solutions alternately (**Scheme 5-1**). After LBL cycles, the substrate color became blue even after one cycle (**Figure 5-5**). After four cycles, SEM images showed that seed MOF crystals tightly stacked with each other and completely covered the substrate surface with the 500 nm thickness (**Figure 5-6**). The same LBL procedure was used for Kgm-OMe and Kgm-H. However, the seed layers for these MOFs cannot be obtained. After LBL cycles, the color of the Al_2O_3 substrate was still white. SEM images of the substrates showed that only a tiny amount of Kgm-OMe or Kgm-H particles were scattered on the surface and the Al_2O_3 surface was visible. (**Figure 5-7**)

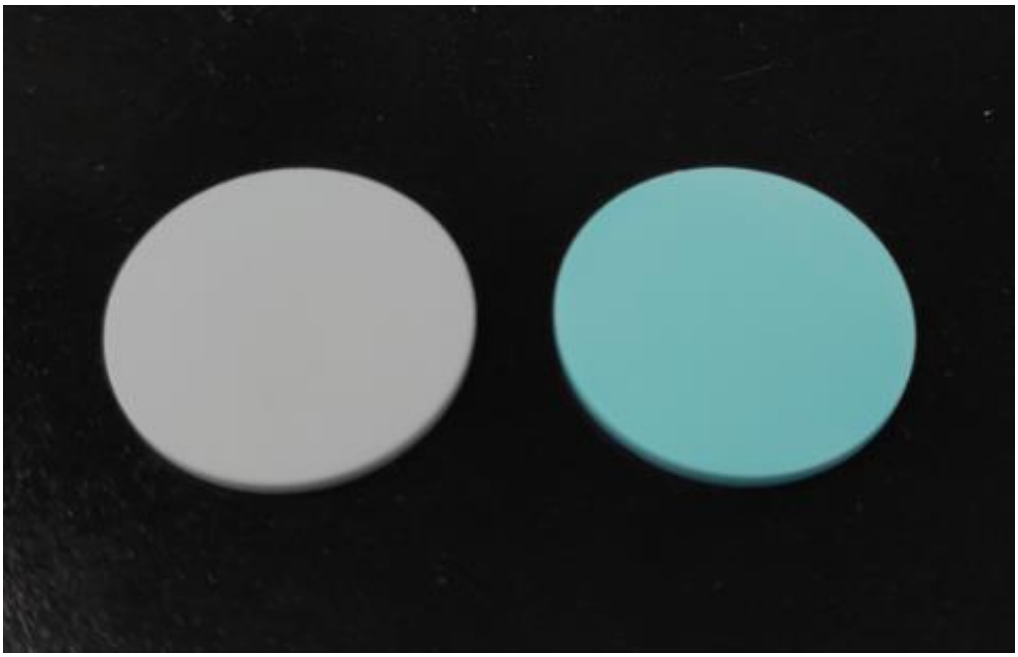

Figure 5-5. Optical images of the Al_2O_3 support (left), Kgm-OPr seed layer after one cycle (right).

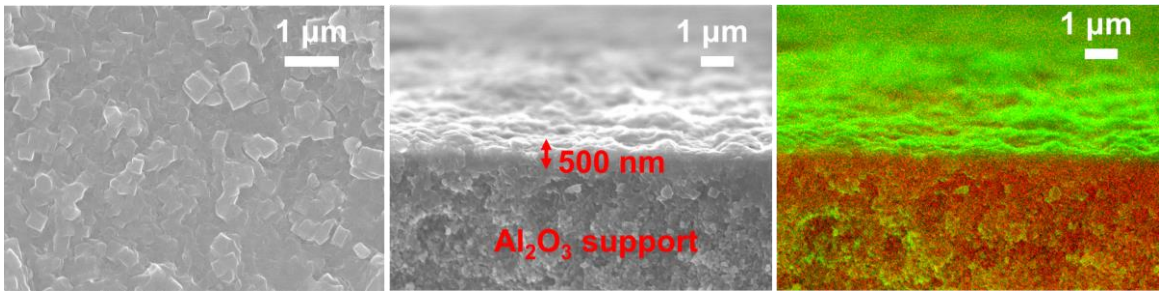

Figure 5-6. SEM images of Kgm-OPr seed layer. Left: Top view. Middle: Cross sectional view. Right: EDX mapping of Cross sectional view, red: Al, Green: background.

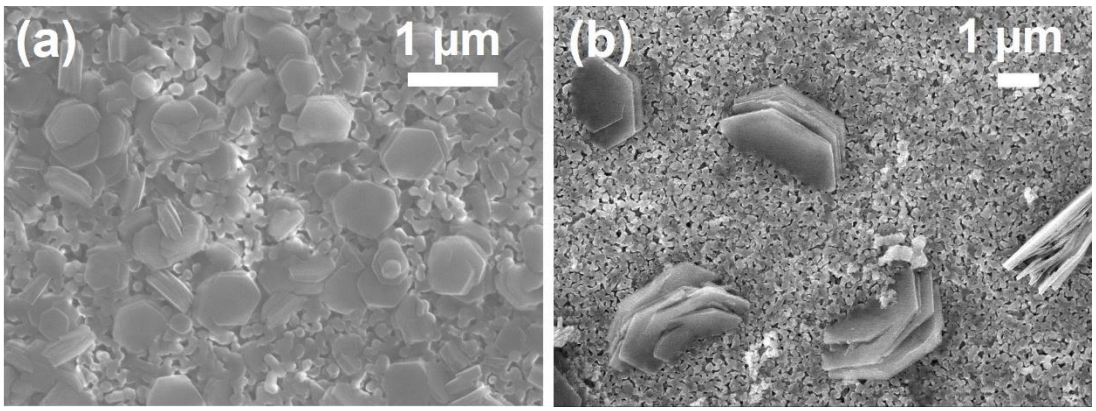

Figure 5-7. SEM images of (a): Kgm-OMe and (b): Kgm-H seed layer after 6 cycles.

The difference in the seed layer formation can be attributed to the difference in the nucleation rates of the crystals. Indeed, the particle sizes of the bulk powder samples of Kgm-OPr, Kgm-OMe, and Kgm-H prepared in the same condition were 0.5, 4.5, and 6 μm, respectively (**Figure 5-8**). The result indicates that Kgm-OPr nucleation is much faster than Kgm-OMe and Kgm-H, as the faster nucleation results in smaller particle size, [37, 38] resulting in the successful formation of the Kgm-OPr seed layer.

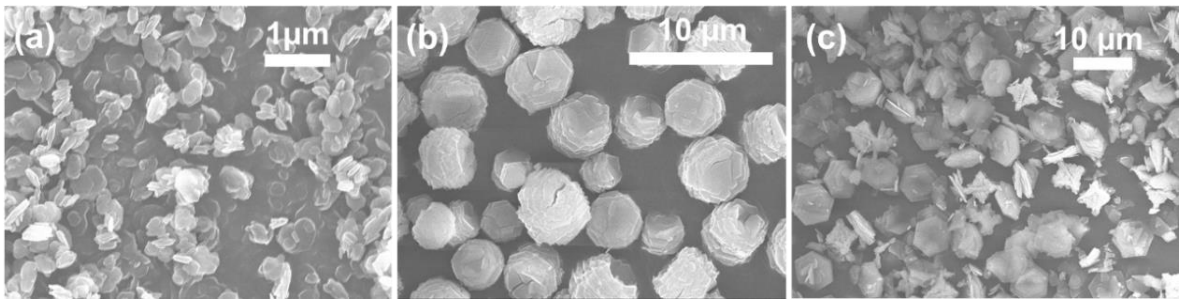

Figure 5-8. SEM images of the Kgm-OPr, Kgm-OMe and Kgm-H powder samples

Preparation of membranes

We attempted to fabricate membranes by secondary growth after successfully preparing the Kgm-OPr seed layer. As Kgm-OMe and Kgm-H are isostructural to Kgm-OPr, we anticipated that Kgm-OMe and Kgm-H crystals can be grown on the Kgm-OPr seed layer by the epitaxial growth. Therefore, the seeded substrate was immersed in the mixed solution of the ligand and metal salt for 6 h. Notably, no bulk powders of Kgm-H and Kgm-OMe were formed in the reaction solution, and Kgm-H and Kgm-OMe crystals grew only on the surface of the Kgm-OPr seed layer. Cross-sectional SEM images of the substrate indicate that Kgm-H and Kgm-OMe membranes formed with thicknesses of 6 and 4 μm, respectively (**Figure 5-9** (a)–(d)). The successful membrane formation was because of the slower crystal nucleation of Kgm-H and Kgm-OMe than the crystal growth. The continuity of the membranes is excellent, with no cracks observed between the

membrane and substrate. Note that extending the growth time to 12 h results in thicker membranes with 15 and 8 μm for Kgm-H and Kgm-OMe, respectively (**Figure 5-10**), despite the presence of macroscopic cracks penetrating from the top and to the bottom of the entire membrane. Therefore, the thick membrane has poor mechanical properties and easily causes cracks. Thus, we used the former membranes for gas separation tests.

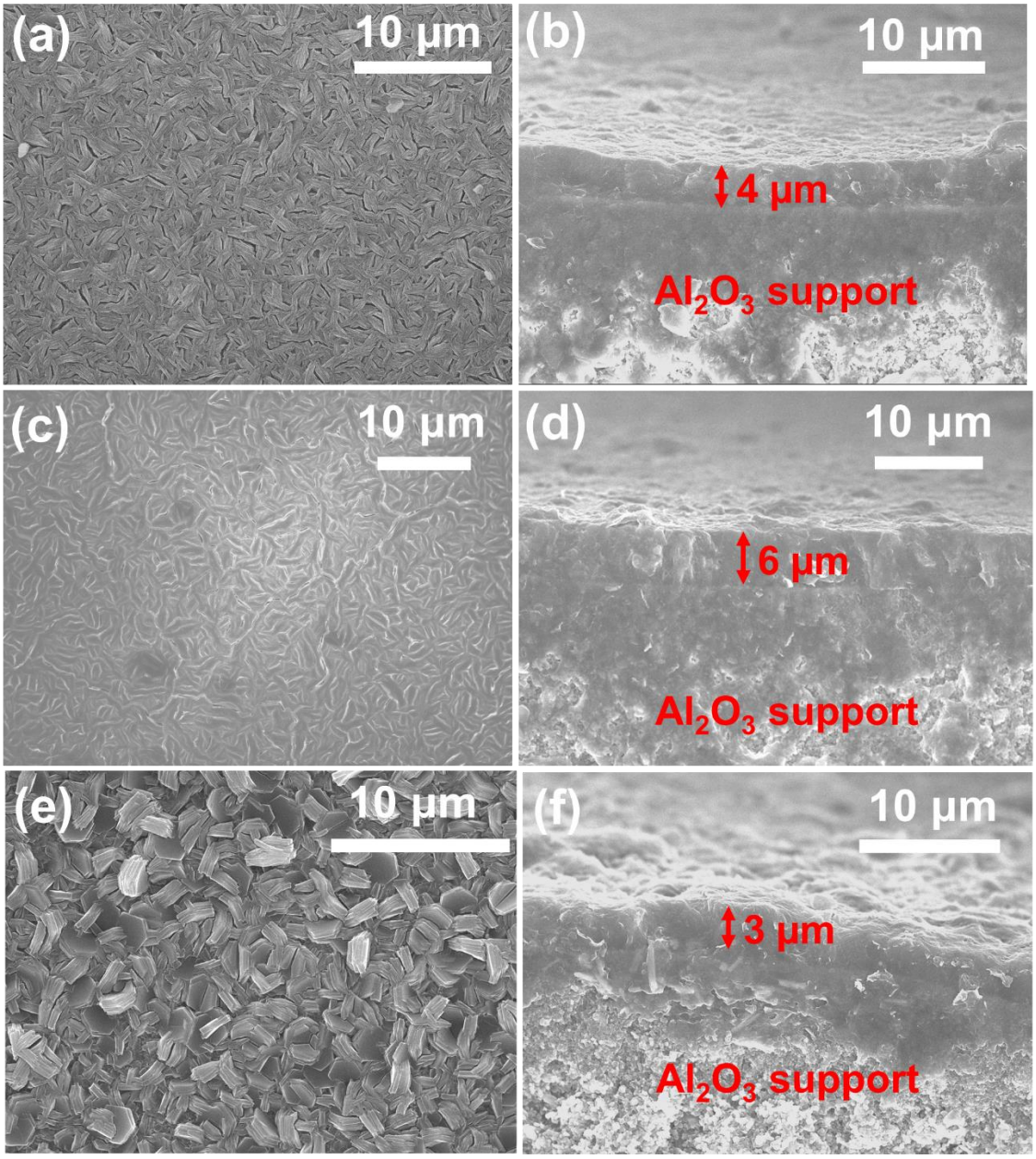

Figure 5-9. SEM images of top views and cross-sectional views, (a) and (b) Kgm-OMe membrane, (c) and (d) Kgm-H membrane, (e) and (f) Kgm-OPr membrane.

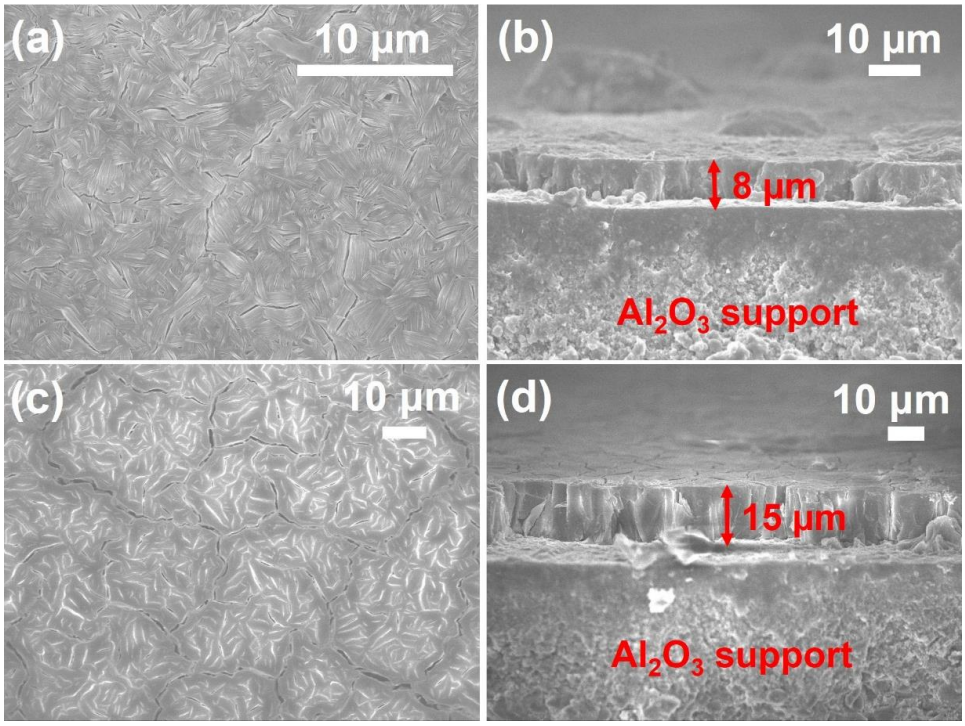

Figure 5-10. SEM images of top views and cross-sectional views under 12 h synthesis time. (a) and (b) Kgm-OMe membrane, (c) and (b) Kgm-H membrane.

We also prepared a Kgm-OPr membrane on a Kgm-OPr seed layer. However, when we used the same preparation conditions as Kgm-OMe and Kgm-H, the Kgm-OPr membrane did not form on the surface. Instead, bulk powders of Kgm-OPr were formed in the reaction solution because of the too fast crystal nucleation than crystal growth. When the concentration was reduced to slow down the reaction rate, the Kgm-OPr membrane grew from the seed layer, whereas Kgm-OPr can still be formed in the solution. The top view of SEM images shows that the membrane fully covered the Al_2O_3 substrate with a thickness of 3 μm (**Figures 5-9** (e) and (f)).

The XRD patterns of the Kgm-OPr seed layer and all three membranes are consistent with the simulated pattern of Kgm-OPr (**Figures 5-11** (a)). However, the relative peak intensities differ, indicating that the membranes have a preferential crystal orientation. The peak intensity for the Kgm-OPr membrane matched that of the powder sample, indicating that the crystals grew randomly (**Figures 5-11** (b)). In the case of Kgm-OMe

and Kgm-H membranes, 2-10 peak at 9.3° was much higher than that of the 100 peaks at 5.5°, although 100 peak is higher than the 2-10 peaks in the simulated pattern of Kgm-OPr (**Figures 5-11** (c) and (d)). Therefore, Kgm-OMe and Kgm-H crystals orient preferably in the [2-10] direction. SEM images of membranes also show the orientation, as the hexagonal MOF crystals are nearly perpendicular to the substrate and one side of the hexagon is parallel to the surface (**Figures 5-9** (a) and (c)). Note that 201 and 301 peaks are visible. Therefore, the gas transportation path (i.e., 1-dimensional channels of kagomé MOFs with [001] direction) is still available, although largely tilted from the gas permeation direction. **Figure 5-12** shows the optical images of Al_2O_3 support, Kgm-OPr seed layer and the three membranes.

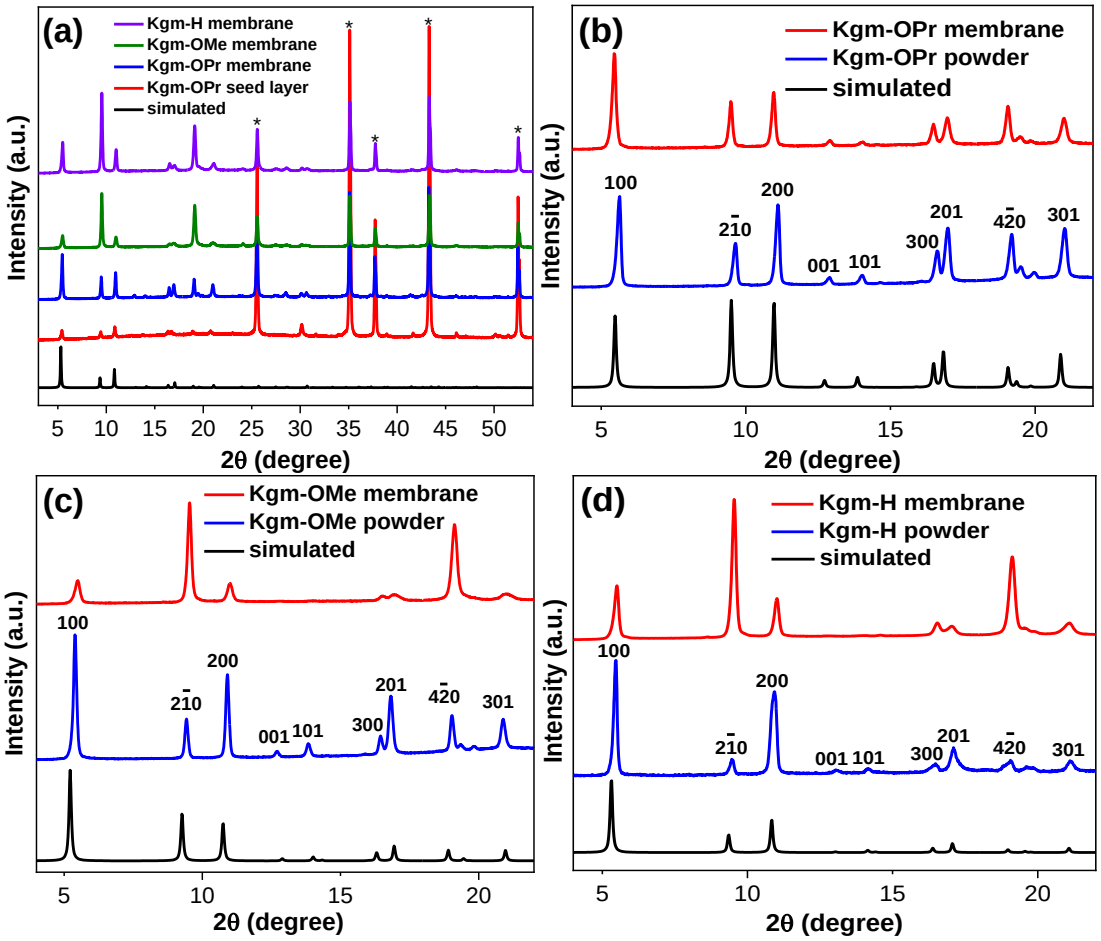

Figure 5-11. XRD patterns of simulated, Kgm-OPr seed layer, Kgm-OPr, Kgm-OMe and

Kgm-H membrane. *: Al_2O_3 support.

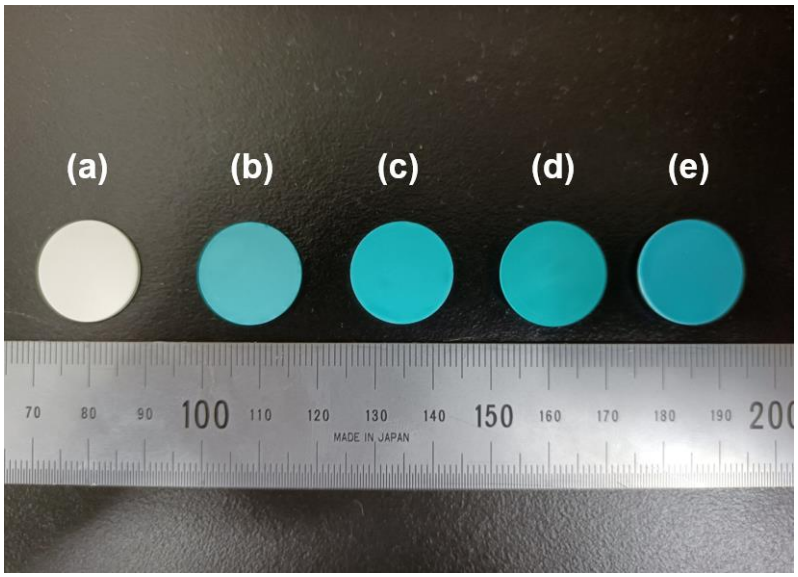

Figure 5-12. Optical images of the (a) Al_2O_3 support, (b) Kgm-OPr seed layer, (c) Kgm-OPr membrane, (d) Kgm-OMe membrane and (e) Kgm-H membrane.

Single gas permeation and mixture gas separation

Single and binary gas permeation measurements were conducted at 10 kPa differential pressure and 25°C for the Kgm-OPr, Kgm-OMe, and Kgm-H membranes (**Figure 5-13**, **Table 5-2 - 5-7**). The permeance of H_2 for Kgm-OPr membrane is much higher than CO_2, CH_4, and C_2H_4 (**Figure 5-13**(a)). The ideal selectivities of H_2 over N_2 and CH_4 gases can reach around 5-6, which surpass the Knudsen constant. However, the ideal CO_2/N_2 and CO_2/CH_4 equimolar selectivity determined from the single-gas permeances were 1.2 and 1.3, respectively (**Figure 5-13**(b)). This result indicates that only H_2 can permeate through the pores of Kgm-OPr and other gases permeate mainly through boundary voids between the polycrystals.

Different from the Kgm-OPr membrane, both the Kgm-OMe and Kgm-H herterobilayer membranes exhibit higher CO_2 permeance than those of N_2, CH_4, and C_2H_4. The ideal equimolar selectivities of CO_2/N_2 and CO_2/CH_4 are 5.9 and 6.8 for Kgm-OMe membrane, and 5.1 and 5.7 for the Kgm-H membrane, respectively (**Figure 5-13**(c)-(f)).

The high CO_2 permeance and selectivity than N_2 and CH_4 may be resulted from both preferential adsorption of CO_2 that promotes the surface diffusion and the smaller kinetic diameter resulting in a higher mobility of CO_2, as seen in the previously reported microporous membranes. [28, 30, 42] We note that lower C_2H_4 permeance than CO_2 is probably due to the larger molecular diameter of C_2H_4 leading to the higher diffusion resistance, which has larger influence than the adsorption affinity of C_2H_4.

The separation factors of the Kgm-OMe membrane determined from the permeation tests using CO_2/N_2 and CO_2/CH_4 equimolar mixed-gases are 6.5 and 7.8, respectively, and those of Kgm-H membrane are 5.5 and 6.1, respectively. The values are slightly higher than the ideal selectivities. This is due to competitive diffusion in the mixtures, in which the diffusion of CH_4 and N_2 through the Kgm-OMe and Kgm-H membranes is hindered by CO_2 molecules adsorbed on the pore. Conversely, the CO_2/C_2H_4 separation factor is lower than the ideal selectivity, which is due to the lower permeance of CO_2 in CO_2/C_2H_4 mixtures than that in single CO_2 gas because adsorbed C_2H_4 molecules impede the passage of CO_2. Note that separation factors of Kgm-OMe membrane are slightly higher than those of Kgm-H membrane, whereas the permeances of Kgm-OMe membrane are smaller than those of Kgm-H membrane. Kgm-OMe and Kgm-H crystals grow nearly vertically to the substrate, resulting in pores that lie horizontally to the gas permeation direction. Therefore, the gas diffusion pathway lengthens significantly than that of the crystals grown horizontally to the substrate. Considering that the adsorption capacities of Kgm-H and Kgm-OMe at 25°C are similar for CO_2, CH_4, N_2, and C_2H_4 (**Figure 5-4** (a) and (b)), the difference in the selectivities may be ascribed to the trade-off between permeability and selectivity caused by the difference in the pore sizes of Kgm-OMe and Kgm-H. Moreover, the CO_2/CH_4 separation factor of the Kgm-OMe membrane exceeds many of the pure polycrystalline MOF membranes reported so far (**Table 5-8**).

Table 5-2. Single gas permeances and ideal selectivities for the Kgm-OMe membrane at

25 ℃ and a pressure drop of 10 kpa

Gas	Knudsen constant	Permeance (mol m^{-2} s^{-1} pa^{-1})	Ideal selectivity
H_2	-	4.23×10^{-10}	-
CO_2	-	3.39×10^{-10}	-
N_2	$CO_2/N_2 = 0.8$	0.57×10^{-10}	$CO_2/N_2 = 5.9$
CH_4	$CO_2/CH_4 = 0.6$	0.5×10^{-10}	$CO_2/CH_4 = 6.8$
C_2H_4	$CO_2/C_2H_4 = 0.8$	0.35×10^{-10}	$CO_2/C_2H_4 = 9.7$

Table 5-3. Single gas permeances and ideal selectivities for the Kgm-H membrane at 25 ℃ and a pressure drop of 10 kpa

Gas	Knudsen constant	Permeance (mol m^{-2} s^{-1} pa^{-1})	Ideal selectivity
H_2	-	13.08×10^{-10}	-
CO_2	-	10.9×10^{-10}	-
N_2	$CO_2/N_2 = 0.8$	2.14×10^{-10}	$CO_2/N_2 = 5.1$
CH_4	$CO_2/CH_4 = 0.6$	1.91×10^{-10}	$CO_2/CH_4 = 5.7$
C_2H_4	$CO_2/C_2H_4 = 0.8$	1.79×10^{-10}	$CO_2/C_2H_4 = 7.3$

Table 5-4. Single gas permeances and selectivities for the Kgm-OPr membrane at 25 ℃ and a pressure drop of 10 kpa

Gas	Knudsen constant	Permeance (mol m^{-2} s^{-1} pa^{-1})	Ideal selectivity
H_2	-	1.54×10^{-8}	-
CO_2	-	0.35×10^{-8}	-
N_2	$CO_2/N_2 = 0.8$	0.29×10^{-8}	$CO_2/N_2 = 1.2$
CH_4	$CO_2/CH_4 = 0.6$	0.27×10^{-8}	$CO_2/CH_4 = 1.3$
C_2H_4	$CO_2/C_2H_4 = 0.8$	0.22×10^{-8}	$CO_2/C_2H_4 = 1.6$

Table 5-5. Binary gas permeances and separation factors for the Kgm-OMe membrane at 25 ℃ and a pressure drop of 10 kpa

Gas	Knudsen constant	CO_2 permeance (mol m^{-2} s^{-1} pa^{-1})	The other component permeance (mol m^{-2} s^{-1} pa^{-1})	Separation factor
CO_2/N_2	0.8	3.69×10^{-10}	0.57×10^{-10}	6.5
CO_2/CH_4	0.6	3.58×10^{-10}	0.46×10^{-10}	7.8
CO_2/C_2H_4	0.8	1.45×10^{-10}	0.19×10^{-10}	7.5

Table 5-6. Binary gas permeances and separation factors for the Kgm-H membrane at

25 ℃ and a pressure drop of 10 kpa

Gas	Knudsen constant	CO_2 permeance (mol m^{-2} s^{-1} pa^{-1})	The other component permeance (mol m^{-2} s^{-1} pa^{-1})	Separation factor
CO_2/N_2	0.8	12.8×10^{-10}	2.33×10^{-10}	5.5
CO_2/CH_4	0.6	12.3×10^{-10}	2.02×10^{-10}	6.1
CO_2/C_2H_4	0.8	7.8×10^{-10}	1.44×10^{-10}	5.4

Table 5-7. Binary gas permeances and separation factors for the Kgm-OPr membrane at 25 ℃ and a pressure drop of 10 kpa

Gas	Knudsen constant	CO_2 permeance (mol m^{-2} s^{-1} pa^{-1})	The other component permeance (mol m^{-2} s^{-1} pa^{-1})	Separation factor
CO_2/N_2	0.8	0.39×10^{-8}	0.30×10^{-8}	1.3
CO_2/CH_4	0.6	0.36×10^{-8}	0.26×10^{-8}	1.4
CO_2/C_2H_4	0.8	0.25×10^{-8}	0.19×10^{-8}	1.3

Binary gas permeation (**Figure 5-14**) of Kgm-OMe and Kgm-H membranes retained the separation factors over 10 h, showing good stability within the investigated time. Furthermore, the temperature-dependent separation factors for equimolar CO_2/CH_4 and CO_2/N_2 mixtures on Kgm-OMe and Kgm-H membranes demonstrated thermal stability from 25°C–140°C (**Figure 5-15**).

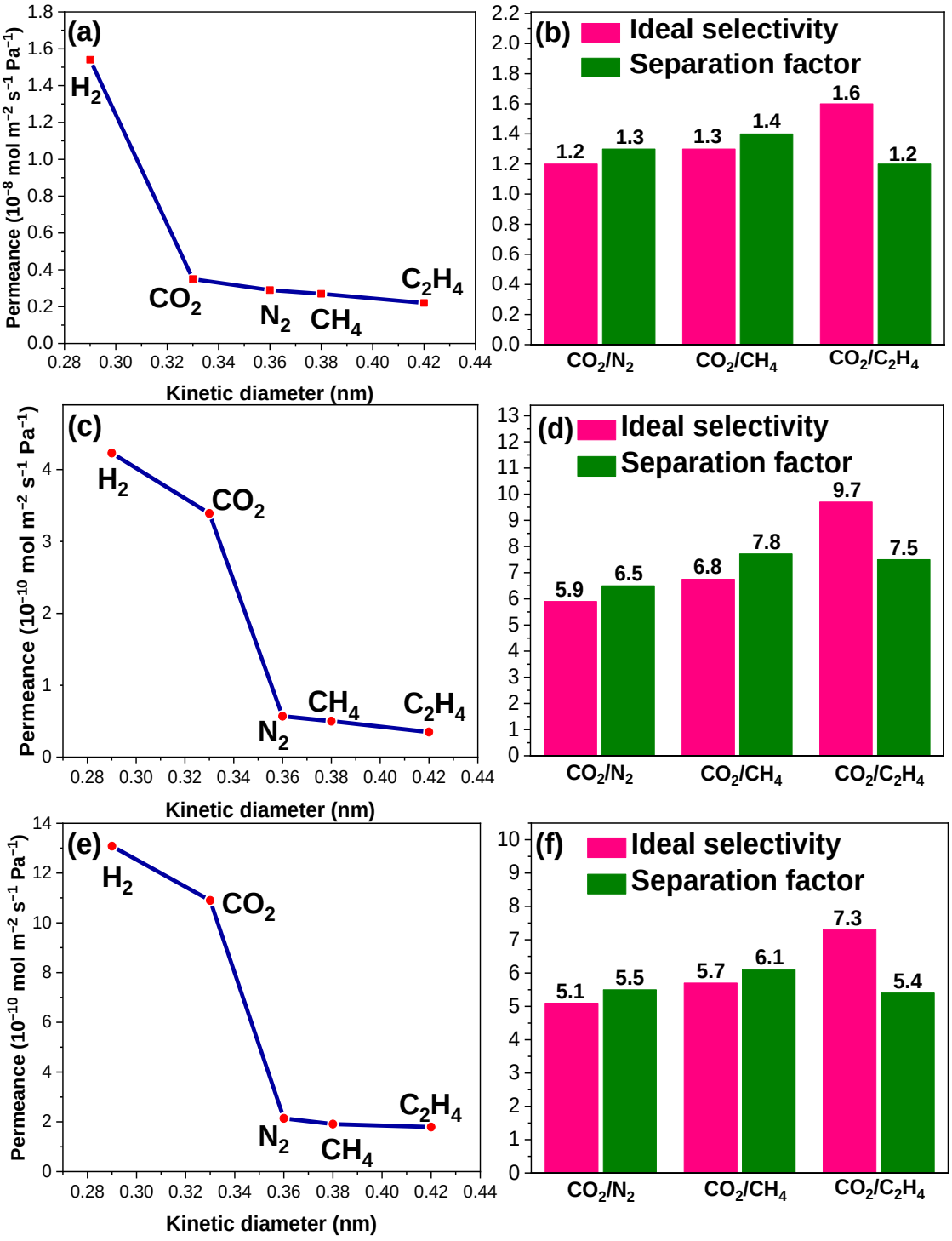

Figure 5-13. Single gas permeance, ideal selectivity and separation factors by mixture gas of (a) Kgm-OPr, (b) Kgm-OMe and (c) Kgm-H membranes.

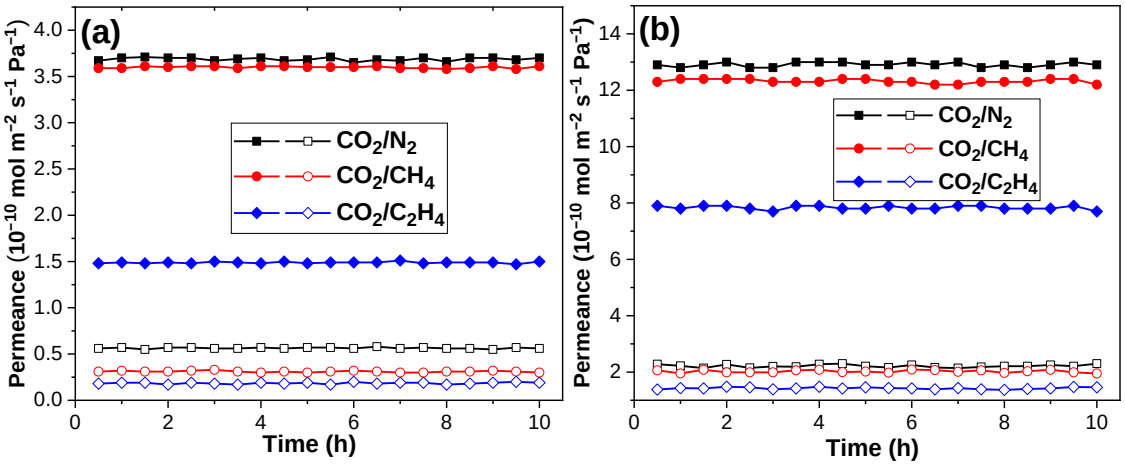

Figure 5-14. The permeances of CO_2/N_2, CO_2/CH_4 and CO_2/C_2H_4 from binary gas mixtures as a function of time at 25 °C with a pressure drop of 10 kPa at different times. (a) Kgm-OMe membranes, (b) Kgm-H membrane.

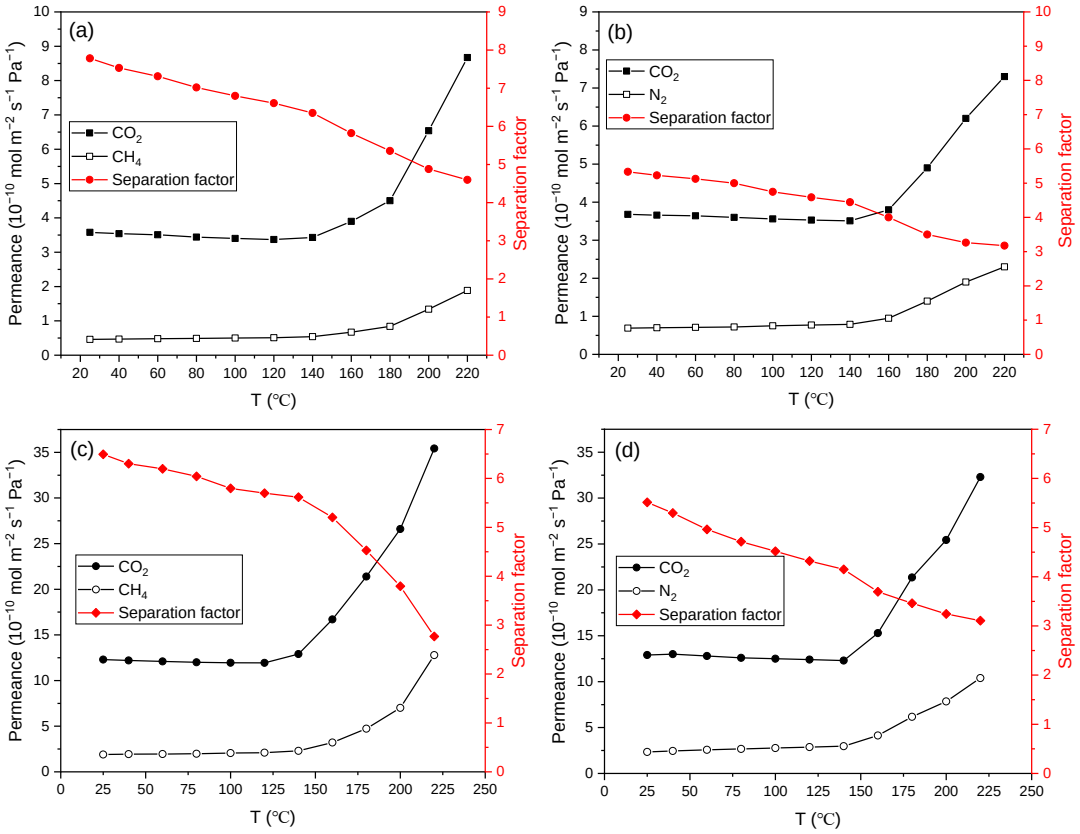

Figure 5-15. Mixture separation factors for CO_2/CH_4 and CO_2/N_2 on the Kgm-OMe membrane ((a)and (b)) and Kgm-H membrane ((c)and (d)) at 10 kpa as a function of

temperature.

Table S8. Comparison of the CO_2 separation performances of the heterobilayer membranes in this study with other MOF membranes from literatures.

MOF Membrane	Temperature	CO_2 Permeance (mol m^{-2} s^{-1} pa^{-1})	Selectivity	Reference
Bio-MOF-14	22℃	4.1×10^{-6}	CO_2/N_2 = N/A CO_2/CH_4 = 3.5	43
Bio-MOF-13	22℃	3.1×10^{-6}	CO_2/N_2 = N/A CO_2/CH_4 = 3.8	43
Bio-MOF-1	25℃	1.1×10^{-6}	CO_2/N_2 = N/A CO_2/CH_4 = 2.6	44
ZIF-8	35℃	1.22×10^{-7}	CO_2/N_2 = 2.7 CO_2/CH_4 = 2.9	45
$[Cu_2L_2P]_n$	25℃	1.5×10^{-8}	CO_2/N_2 = N/A CO_2/CH_4 = 6	46
UIO-66	25℃	1.7×10^{-9}	CO_2/N_2 = 1.13 CO_2/CH_4 = 1.06	47
SAM-1	25℃	8.0×10^{-8}	CO_2/N_2 = 4.5 CO_2/CH_4 = N/A	48
CAU-10-H	30℃	3×10^{-8}	CO_2/N_2 = 42 CO_2/CH_4= 95	49
CAU-1	RT	1.32×10^{-6}	CO_2/N_2 = 26.2 CO_2/CH_4 = 14.8	28
ZIF-69	RT	1×10^{-7}	CO_2/N_2 = 6.3 CO_2/CH_4 = 4.6	29
Kgm-H	25℃	10.9×10^{-10}	CO_2/N_2 = 5.5 CO_2/CH_4 = 6.1	This work
Kgm-OMe	25℃	3.39×10^{-10}	CO_2/N_2 = 6.5 CO_2/CH_4 = 7.8	This work

RT: Room temperature.

To summarize the influence of the crystal grow processes for the three MOFs on the membrane formation, firstly Kgm-OPr has a faster crystal nucleation rate and forms smaller crystals. This resulted in the formation of a homogeneous seed layer on the substrate, whereas the permeances of the Kgm-OPr membrane range ~10^{-8} mol m^{-2} s^{-1} Pa^{-1}, which are much higher than those of Kgm-OMe and Kgm-H membrane (10^{-10}~10^{-9}

mol m^{-2} s^{-1} Pa^{-1}), indicating that Kgm-OPr crystals were unable to grow sufficiently within the intercrystalline gaps in membrane layer. Secondly, because nucleation rates for Kgm-OMe and Kgm-H are relatively slow, which made them difficult to grow a full-coverage crystal seed layer, and the membrane cannot epitaxial crystal intergrowth from the seed crystals of Kgm-OPr preferably proceeded rather than the new crystal formation on the substrate, resulting in homogeneous crystal growth and dense membrane formation (**Figure 5-16**).

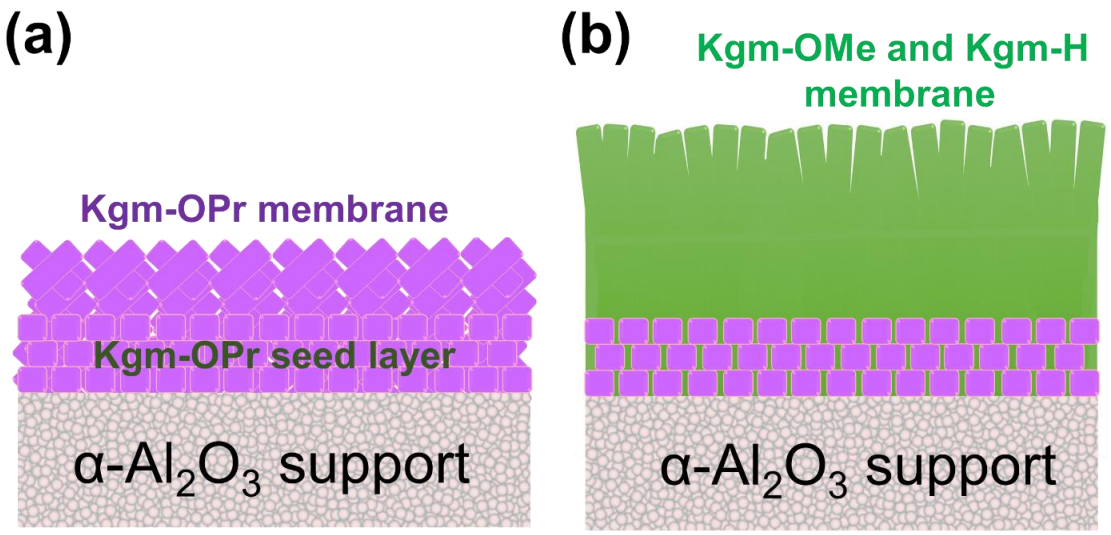

Figure 5-16. Crystal structures of degassed HKUST-1. (a) Local paddle wheel structure. (b) View of packing structure along the *a* axis. Atoms are colored as follows: Cu, green; O, red; C, gray; H, white.

5-4. Conclusions

In this work, we successfully fabricated two heterobilayer membranes for CO_2 separation from isostructural MOFs, Kgm-OMe, or Kgm-H membrane layers on the Kgm-OPr seed layer, employing the epitaxial secondary growth. Our results not only provide a new technique for fabricating membranes that cannot be directly prepared from the single MOF but also expand the MOF membrane families by combining the advantages of different types of MOFs.

5-5. References

1 D.Y.C. Leung, G. Caramanna, M.M. Maroto-Valer, *Renew. Sustain. Energy Rev.*, 2014, **39**, 426–443.

2 G.T. Rochelle, *Science*, 2009, **325**, 1652–1654.

3 Y. Zhang, J. Sunarso, S. Liu, R. Wang, Int. *J. Greenh. Gas Control.*, 2013, **12**, 84–107.

4 J. Liu, X. Hou, H.B. Park, H. Lin, *Chem. Eur. J.*, 2016, **22**, 15980–15990.

5 I. van Zandvoort, J.K. van der Waal, E.J. Ras, R. de Graaf, R. Krishna, *Sep. Purif. Technol.*, 2019, **227**, 115730.

6 Z. Li, L. Wang, C. Li, Y. Cui, S. Li, G. Yang, Y. Shen, *ACS Sustain. Chem. Eng.*, 2019, **7**, 10403–10414.

7 H. Hikita, S. Asai, Y. Katsu, S. Ikuno, *AIChE J.*, 1979, **25**, 793–800.

8 X. Wang, N.G. Akhmedov, D. Hopkinson, J. Hoffman, Y. Duan, A. Egbe, K. Resnik, B. Lia, *Appl. Energy.*, 2016, **161**, 41–47.

9 Q. Wang, J. Luo, Z. Zhong, A. Borgna, *Energy. Environ. Sci.*, 2010, **4**, 42–55.

10 E.D. Bates, R.D. Mayton, I. Ntai, J.H. Davis, *J. Am. Chem. Soc.*, 2002, **124**, 926–927.

11 X. Mu, Y. Chen, E. Lester, T. Wu, *Micropor. Mesopor. Mat.*, 2018, **270**, 249–257.

12 Y. Huang, R.W Baker, L.M Vane, *Ind. Eng. Chem. Res.*, 2010, **49**, 3760–3768.

13 S. Adhikari and S. Fernando, *Ind. Eng. Chem. Res.*, 2006, **45**, 875–881.

14 W. Raza, J. Wang, J. Yang, T. Tsuru, Sep. Purif. Technol. 2021, 262, 118338

15 C. Ma, J.J. Urban, *Chem.Sus.Chem.*, 2019, **12**, 4405–4411.

16 S. Yuan, X. Li, J. Zhu, G. Zhang, P. Van. Puyvelde, B.V.D. Bruggen, *Chem. Soc. Rev.*, 2019, **48**, 2665–2681.

17 Y. Liu, Y. Ban, W. Yang, *Adv. Mater.*, 2017, **29**, 1606949.

18 A. Schoedel, M. Li, D. Li, M. O'Keeffe, O.M. Yaghi, *Chem. Rev.*, 2016, **116**, 12466–12535.

19 M. Kondo, T. Okubo, A. Asami, S. Noro, T. Yoshitomi, S. Kitagawa, T. Ishii, H. Matsuzaka, K. Seki, *Angew. Chem. Int. Ed.*, 1999, **38**, 140–143.

20 J.H. Cavka, S. Jakobsen, U. Olsbye, N. Guillou, C. Lamberti, S. Bordiga, and K.P. Lillerud. *J. Am. Chem. Soc.*, 2008, **130**, 13850–13851.

21 R. Matsuda, R. Kitaura, S. Kitagawa, Y. Kubota, R.V. Belosludov, T.C. Kobayashi, H. Sakamoto, T. Chiba, M. Takata, Y. Kawazoe, Y. Mita, *Nature*, 2005, **436**, 238–241.

22 J.L.C. Rowsell, O.M. Yaghi, *J. Am. Chem. Soc.*, 2006, **128**, 1304–1315.

23 S. Krause, V. Bon, I. Senkovska, U. Stoeck, D. Wallacher, D.M. Többens, S. Zander, R.S. Pillai, G. Maurin, F.X. Coudert, S. Kaskel, *Nature*, 2016, **532**, 348–352.

24 J. Ma, X. Guo, Y. Ying, D. Liu, C. Zhong, Chem. Eng. J., 2017, 313, 890–898.

25 H. Yin, J. Wang, Z. Xie, J. Yang, J. Bai, J. Lu, J. Lu, Y. Zhang, D. Yin, J.Y.S. Lin, *Commun. Chem.*, 2014, **50**, 3699–3701.

26 M.W. Anjum, F. Vermoortele, A.L. Khan, B. Bueken, D.E.D. Vos, I.F.J. Vankelecom, *ACS Appl. Mater. Interfaces.*, 2015, **7**, 25193–25201.

27 N. Hara, M. Yoshimune, H. Negishi, K. Haraya, S. Hara, T. Yamaguchi, *J. Membr. Sci.*, 2014, **450**, 215–223.

28 H. Yin, J. Wang, Z. Xie, J. Yang, J. Bai, J. Lu, J. Lu, Y. Zhang, D. Yin, J.Y.S. Lin, *Commun. Chem.*, 2014, **50**, 3699–3701.

29 Y. Liu, G. Zeng, Y. Pan, Z. Lai, *J. Membr. Sci.*, 2011, **379**, 46–51.

30 J. Yan, Y. Sun, T. Ji, C. Zhang, L. Liu, Y. Liu, J. Membr. Sci., 2022, 120496.

31 Y. Pan, T. Li, G. Lestari, Z. Lai, *J. Membr. Sci.*, 2012, **390**, 93–98.

32 Y. Sun, Y. Liu, J. Caro, X. Guo, C. Song, Y. Liu, *Angew. Chem. Int. Ed.*, 2018, **130**, 16320–16325.

33 F. Zhang, X. Zou, X. Gao, S. Fan, F. Sun, H. Ren, G. Zhu, *Adv. Funct. Mater.*, 2012, **22**, 3583–3590.

34 B. Ghalei, K. Wakimoto, C.Y. Wu, A.P. Isfahani, T. Yamamoto, K. Sakurai, M. Higuchi, B.K. Chang, S. Kitagawa, E. Sivaniah, *Angew. Chem. Int. Ed.*, 2019, **58**, 19034–19040.

35 V. Chernikova, O. Shekhah, Y. Belmabkhout, M. Eddaoudi, *ACS Appl. Nano Mater.*, 2020, **3**, 6432–6439.

36 Y. Yoo, H.K. Jeong, *Cryst. Growth Des.*, 2020, **10**, 1283–1288.

37 B. Garai, A. Mallick, A. Das, R. Mukherjee, R. Banerjee, *Chem. Eur. J.*, 2017, **23**, 7361–7366.

38 O. Barreda, G. Bannwart, G.P. A.Yap, E.D. Bloch, *ACS. Appl. Mater. Interfaces.*, 2018, **10**, 11420–11424.

39 H. Sato, W. Kosaka, R. Matsuda, A. Hori, Y. Hijikata, R.V. Belosludov, S. Sakaki, M. Takata, S. Kitagawa. *Science*, 2014, **343**, 167–170.

40 S.H. Jhung, T. Jin, Y.K. Hwang, J.S. Chang, *Chem. Eur. J.*, 2007, **13**, 4410–4417.

41 X. Wu, Z. Bao, B. Yuan, J. Wang, Y. Sun, H. Luo, S. Deng, *Micropor. Mesopor. Mat.*, 2013, **180**, 114–122.

42 R. Krishna, J.M. van Baten, *J. Membr. Sci.*, 2022, **643**, 120049.

43 Z. Xie, T. Li, N. L. Rosi, M. A. Carreon, *J. Mater. Chem.* A. 2014, 2, 1239.

44 J.A. Bohrman, M.A. Carreon, *Chem. Commun.*, 2012, **48**, 5130–5132.

45 D. Liu, X. Ma, H. Xi, Y.S. Lin, *J. Membr. Sci.*, 2014, **451**, 85-93.

46 A. Bétard, H. Bux, S. Henke, D. Zacher, J. Caro, R.A. Fischer, *Micropor. Mesopor. Mat.*, 2012, **150**, 76–82.

47 B. Ghalei, K. Wakimoto, C.Y. Wu, A.P. Isfahani, T. Yamamoto, K. Sakurai, M. Higuchi, B.K. Chang, S. Kitagawa, E. Sivaniah. *Angew. Chem. Int. Ed.*, 2019, **58**, 19034–19040.

48 S. Aguado, C.-H. Nicolas, V. Moizan-Basle´, C. Nieto, H. Amrouche, N. Bats, N. Audebrand, D. Farrusseng, *New J. Chem.*, 2011, **35**, 41–44.

49 D.S. Chiou, H.J. Yu, T.H. Hung, Q. Lyu, C.K. Chang, J.S. Lee, L.C. Lin, D.Y. Kang, *Adv. Funct. Mater.*, 2021, **31**, 2006924.

Chapter 6

General Conclusions

This thesis describes the design and synthesis of porous and stable metal-organic frameworks (MOFs) containing interaction bonding sites for gas adsorption separation. We controlled the crystal space group for capturing oxygen from the air as well as controlled 3D porous structure for CO_2/N_2 and C_2H_2/C_2H_4 adsorption separation. This thesis also describes the design and adjustment of crystal growth of MOF membranes for H_2 purification and CO_2 separation, including the fabrication of MOF membranes with optimized microstructure and orientation for H_2 purification, controlled pore size and crystal growth rate for CO_2/N_2 and CO_2/CH_4 separation.

Chapter 2 describes the synthesis and controlled crystal growth of porous and stable SIFSIX pillared MOFs. We synthesized porous and stable MOFs ($Zn(dpa)_2(SiF_6)$) by adjustment of solvents and metals. $Zn(dpa)_2(SiF_6)$ exhibits the property of trapping oxygen in air under UV light with a conversion rate of 55% and releasing O_2 after heating at 140 °C. Moreover, $Zn(dpa)_2(SiF_6)$ exhibits high selectivity for O_2 and this chapter will provide a new method for separating oxygen from the air.

Chapter 3 describes the synthesis and crystal phase controlling of SIFSIX pillared MOFs through the reaction between different hexafluorosilicate metals (Ni, Co, Zn, Cd) and 4,4′-bipyridine (SIFSIX-1-M) or 1,2-bis(4-pyridyl)ethane (SIFSIX-7-M). The construction of SIFSIX MOFs based on these metals and ligands has always been a challenge and some researchers could only able prepare 2D non-porous MOFs. Our work successfully prepared 3D porous SIFSIX MOFs, in which SIFSIX-1-Ni, SIFSIX-1-Co, and SIFSIX-7-Ni can maintain 3D structures in a water-free environment. Gas adsorption experiments and IAST selectivity calculations show that those 3D and stable structures have excellent CO_2/N_2 and C_2H_2/C_2H_4 separation performance.

Chapter 4 describes the fabrication method of combining the surface modification of a substrate and the layer-by-layer (LBL) method, where the substrate was immersed in the metal-ion and ligand solutions repeatedly, to construct a continuous seed layer, from which dense and defect-free MOF (Kgm-OEt) membrane was fabricated by the secondary growth. The gas permeation results from the binary gas mixture demonstrated the absence

of defects. The controlled crystal growth enabled the crystal orientation such that 1D pores of Kgm-OEt were parallel to the gas permeation pathway through the membrane, which was suitable for gases transportation. This defect-free Kgm-OEt membrane can be applied for H_2 purification and shows higher H_2/CO_2 selectivity than polymer membrane.

Chapter 5 describes the fabrication of two heterobilayer membranes from isostructural MOFs, that is, Kgm-OMe and Kgm-H membranes based Kgm-OPr seed layer through secondary growth. Due to the lower reaction rates and larger particle size of Kgm-OMe and Kgm-H, they can eliminate the defects of Kgm-OPr seed layer through intergrow with Kgm-OPr seed. The gas molecules can transport through the 1D channels of MOF sheets then sieved by Kgm-OPr layer. Kgm-OMe and Kgm-H membranes showed excellent separation performance for CO_2/CH_4 and CO_2/N_2 binary mixtures. The separation factor for CO_2/CH_4 and CO_2/N_2 can reach up to 7.8 and 6.5 on Kgm-OMe membrane, 5.7 and 5.5 on Kgm-H membrane. The two membranes extended the MOF membrane families that can be used to separate CO_2 with N_2 or CH_4. Not only that, but the method also demonstrated in this research will provide a new concept to design molecule separation membranes by combining the advantages of different isostructural MOFs.

Compared with the traditional gas separation methods such as distillation, the advantages of adsorption separation and membrane separation are low-energy consumption and easy operation. For some gas mixtures that are difficult to achieve by membrane separation, adsorption separation can be a better choice. For example, the close molecular size of oxygen, argon, and nitrogen makes membrane separation difficult to achieve effective separation. Membrane separation is also ineffective in separating trace amounts of acetylene (1%) from ethylene. At this point, adsorption separation is a better option. MOFs with high-surface areas and tunable structures have attracted considerable interest in gas selective adsorption and separation. However, the structure of MOFs is variable with metals and ligands and is easy to change with the change in post-treatment environment. The synthesis of MOFs with interaction bonding sites and stable structures

is always a challenge. In chapter 2 and chapter 3, we focus on synthesis of SIFSIX pillared MOFs with controlled crystal structure through conditioning the metals, ligands, and solvents. We synthesized MOFs ($Zn(dpa)_2(SiF_6)$) with the property of selectively trapping oxygen in air under UV light and releasing O_2 after heating. $Zn(dpa)_2(SiF_6)$ contains the coordination site for singlet oxygen, so the selectivity of O_2/N_2 and O_2/Ar can reach 100%. In addition, three porous and stable SIFSIX pillared MOFs (SIFSIX-1-Ni, Co, and SIFSIX-7-Ni) were also synthesized. They not only show excellent adsorption selectivity for trace amounts of C_2H_2 in C_2H_4 due to the hydrogen bonding with C_2H_2 but also show high selectivity for CO_2 in CO_2/N_2 mixtures.

Membrane separation technology undoubtedly has a lower energy consumption and carbon emission compared to adsorption separation. For some mixed components such as H_2/N_2, H_2/CH_4, CO_2/CH_4, etc, microporous membranes can effectively separate them based on the difference in diffusion rate and interaction affinity with membrane of different molecules. MOF membranes are attracting much attention as a new class of microporous membranes due to the tunability of pore size and the affinity with gas molecules. However, there are still few studies on the crystal growth of MOFs into membranes and the methods for preparing MOF membranes are not well developed. Chapter 4 and chapter 5 focus on the design and growth of MOF membrane for H_2 purification, CO_2/N_2, and CO_2/CH_4 separation. In Chapter 4, we prepared a defect-free Kgm-OEt membrane by modifying the substrate with APTEs combined with layer-by-layer self-assembly and secondary growth. The microstructure of the membrane was optimized on the substrate with APTEs modification. Kgm-OEt membrane can effectively separate H_2 and CO_2. In Chapter 5, we apply this technique to construct heterbilayer MOF membranes for CO_2/N_2, CO_2/CH_4, and CO_2/C_2H_4 separation. Firstly, a MOF Kgm-OPr with fast nucleation rate was fabricated as a seed layer on an Al_2O_3 substrate, the Kgm-OPr has the small pore cross-section size (3.2 Å) and low adsorption capacities and is thought to be impermeable for CO_2, N_2, CH_4, and C_2H_4. Then the layer

of Kgm-OMe or Kgm-H, which is isostructural to Kgm-OPr, was prepared on the Kgm-OPr seed layer through secondary growth. The Kgm-OMe (4.8 Å) and Kgm-H (7.6 Å) has preferential CO_2 adsorption over N_2 and CH_4, and they exhibit CO_2 permselectivity based on the surface diffusion mechanism. It was widely accepted that the gas separation selectivity of membranes could be favorably represented as the interaction of adsorption selectivity and diffusion selectivity. As C_2H_4 has a larger kinetic diameter (4.2 Å) and a lower mobility and diffusivity, so both two heterobilayer membranes show excellent CO_2/N_2, CO_2/CH_4, and CO_2/C_2H_4 separation performance.

Based on these findings described above, it is expected that our finding of the synthesis of SIFSIX pillared MOF crystals and the adjustment of crystal structure for gas selective adsorption can provide guidelines for the synthesis of such MOFs in the future. Our approach to controlling crystal growth for the preparation of MOF membranes will also provide future researchers with experience in the fabrication of MOF membranes.

List of achievements

Publications related to this thesis

[1] Fabrication of a Kagomé-type MOF Membrane by Seeded Growth on Amino-functionalized Porous Al_2O_3 Substrate.

X. Wang, S. Kusaka, A. Hori, R. Matsuda,

Chemistry - An Asian Journal, **2021**, 16, 2018-2021.

[2] Heterobilayer membranes from isostructural metal-organic frameworks for efficient CO_2 separation.

X. Wang, S. Kusaka, A. Hori, S. Sen, R. Matsuda,

Microporous Mesoporous Mater, **2022**, 338, 111950.

Acknowledgements

I would like to dedicate my paper to all those who have offered me tremendous assistance during the study in Nagoya University.

First and foremost, First of all, my heartiest thanks flow to my supervisor, Professor Ryotaro Matsuda, for his helpful guidance, valuable suggestions, and constant encouragement in my study. His profound insight and accurateness about my paper taught me so much that they are engraved on my heart. Secondly, I want to express my heartfelt thanks to Dr. Shinpei Kusaka who provided me with beneficial help and offered me precious comments during the whole process of my writing, without which the paper would not be what it is now.

Also, I wish to express my gratitude to Professor Dr. Kazuki Nakanishi, Professor Dr. Ayae Sugawara Narutaki, and Professor Dr. Yoshiaki Kawajiri for the fruitful discussion and valuable suggestions.

Besides, I am deeply grateful to all the staff and members in the Matsuda laboratory. I would like to express my appreciation to Dr. Yunsheng Ma, Dr. Akihiro Hori, and Dr. Akio Mishima for helpful advice and thoughtful discussion. Also, I would like to thank all of my colleagues in the Matsuda laboratory. When I first came lab, because of the unfamiliar language and equipment, I often need the help of the membranes in Matsuda. lab, which brings them a lot of trouble. Especially, I would like to express my sincere gratitude to Mr. Katsuya Ono, Yuki Harada, Yonezu Akira, and Nakajo Toshinobu for their help to the use of equipment. Meanwhile, I would like to extend my deep gratefulness to all the members in Matsuda lab for their help in my life and study.

Last but not least, I would like to express my thanks to my beloved family for their unfailing love and support. For so many years, they have always been supporting me and respecting me. Their love and care are the greatest fortune of my life.

This thesis is dedicated to all those people who have supported my work.

May 2022

Wang Xiaoguang